UNIVERSITÁ DEGLI STUDI DI PADOVA

PhD thesis

Development of optical instruments for a tomographic analysis of dust and fluids in space environment

Author:
Dr.Alessandro Brunelli
Department of Astronomy of Padua

Supervisor:
Dr. Roberto Ragazzoni
INAF - Observatory of Padua

Professor. Giampaolo Piotto
Department of Astronomy of Padua

Co-Supervisor:
Professor. Simone Esposito
INAF - Observatory of Arcetri

1. Reviewer:

2. Reviewer:

Day of the defense:

To my family

Contents

List of Tables

List of Figures

Abstract

In the following pages are described the projects developed during the PhD. The basic idea followed since from the beginning of the doctorate is the development of several skills in order to increase the personal knowledge in optics and instrumentation for scientific research and for Astronomy. This thesis is focused on specialized arguments and the obtained results. Any theoretical or general introduction is reduced as much as possible.

The interest of Adaptive Optics and the Multi-Conjugate and Layer Oriented techniques leads to the specialization in the team of Adaptive Optics in the Observatory of Padova.

The first collaboration is for the characterization of a sensor for a spatial mission on Mars, designed for the analysis of dust and fluids and take place in the Spacelight company and in the laboratory of the Observatory of Padua. The collaboration took longer for the characterization of a pyramid sensor in the INAF laboratories and the characterisation and the acceptance tests of the optical derotator project for the Large Binocular Telescope (LBT) in Arizona.

A collaboration developed with EIE Group performed in 2011 has represented the right opportunity to learn the basis of the optical design used for a specific ray tracing simulation on the radio telescope of ALMA in Cile. The collaboration with the Adaptive Optics team in Padova and the Max Plank Institute for Astronomy in Heidelberg is not related and connected with the only optical derotator but also take place for the very first optical design of a telescope simulator for the whole alignment of the LINC-NIRVANA wavefront sensor of LBT.

Introduzione In queste pagine é descritta l'attivitá condotta durante il dottorato di ricerca in Astronomia e svoltasi presso il gruppo di Ottica Adattiva dell'Osservatorio di Padova (INAF) e il Dipartimento di Astronomia.

I progetti sono stati sviluppati nell'ambito dell'Ottica Adattiva applicata all'Astronomia e riguardano, in generale, sensori di fronte d'onda a piramide e metodologie di ricostruzione tomografica con tecniche multi-coniugate e Layer Oriented.

La necessitá di sviluppare abilitá scientifiche e tecnologiche mirate alla specializzazione ottica hanno portato alla collaborazione con aziende del settore, quali Spacelight s.r.l., EIE Group ed il Max Planck Institute for Astronomy (MPIA) di Heidelberg. Tali collaborazioni hanno prodotto risultati tecnologici di rilievo quali la realizzazione di un sensore di polveri per ambiente marziano e di un sensore di fronte d'onda per l'analisi tridimensionale di polveri e fluidi a densitá variabile.

La collaborazione congiunta tra Spacelight, INAF e MPIA ha permesso la realizzazione, la caratterizzazione e l'allineamento di due derotatori ottici per il Large Binocular Telescope in Arizona ed il primo disegno ottico del telescope simulator per l'allineamento di LINC-NIRVANA. Una collaborazione specifica con la ditta EIE Group ha permesso inoltre di acquisire e approfondire ulteriori abilitá nell'ambito nel disegno ottico finalizzato a simulazioni di ray tracing per il progetto del radio telescopio ALMA in Cile.

Chapter 1

Introduction

The construction of the LBT began in 1996 in Emerald Peak on Mount Graham in southeastern Arizona at 3000m altude in the Pinaleno mountains . In 1997 the foundations were completed and the ring was built to support the rotating dome. LBT is a telescope with an altazimuth mount and double pupil in a Gregorian configuration and provide the two primary active mirrors, two adaptive secondaries. Two tertiary mirrors for tip-tilt wavefront correction fold the beam into the gregorian focus in the direction of the LINC-NIRVANA wave front sensor implemented on a huge carbon fiber bench.

NIRVANA means Near-IR/Visible Adaptive iNterferometer for Astronomy and provide four wave front sensors, two for each side of the telescope arm [13]. The Ground Layer Wave Front Sensor (GWS) analyze the turbulence generated in the first 100m of atmosphere and send the signal for the correction to the adaptive secondary mirror. The sensor uses up to 12 natural guide star selected in a 6x6arminute field of view. The Mid High Wave Front Sensor (MHWS) analyze the turbulence of the high layers of the atmosphere (8km) and uses up to 6 natural guide star from a 2x2arminute field of view.

The pyramid sensor is the main concept of the wave front sensors and is designed to work on LBT in a multi-Conjugate an Layer Oriented Adaptive Optics configuration. The sensor can correct the atmospheric turbulence while the LINC camera can combine the two wave fronts collected by the two big arms of LBT into the Fizeau interferometer to reach a resolution which is comparable with a 22m telescope [6]. Such caracteristic place LBT in the vert first era of the giant telescope as a representative opportunity for a technological and scientific test bed for any future Astronomical research [12], [10].

The two primary monolithic and parabolic mirrors F/1.14 have a diameter of 8.4m and are glass built and coated with a thin layer of aluminum. The distance between the extremes of the two primary mirrors is called baseline and measures approximately 22.8m. These mirrors are equipped with a system of active optics to correct the load deformation. The two adaptive secondary mirrors with a diameter of 911mm have a concave ellipsoidal design and transform the F ratio from F/1.14 to F/15.28. The secondary mirrors have also an undersized design

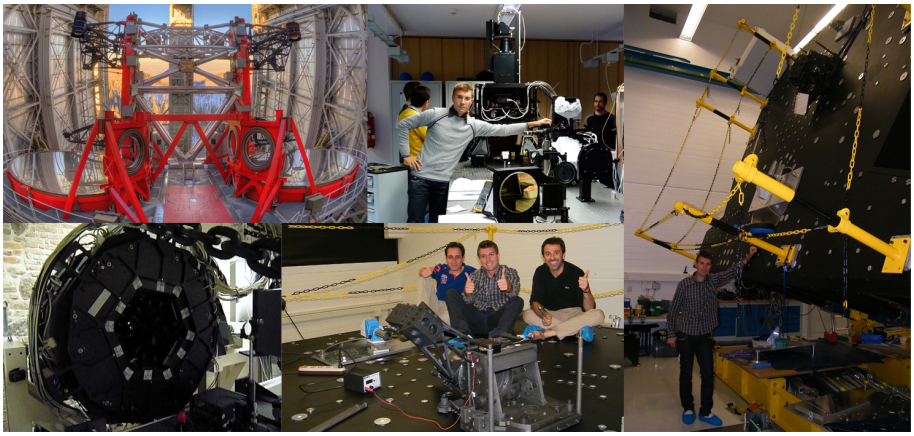

Figure 1.1: *picture collection with images of Large Binocular Telescope (LBT) in Arizona, the Mid High Layer Wave Front Sensor (MHWS), the LINC-NIRVANA bench tilted of 60deg, the Ground Layer Wave Front Sensor, the successful flexure test on the K-mirror unit for LBT.*

to avoid IR noise coming from the environmental thermal radiation.

1.1 The Pyramid Sensor

The pyramid sensor used on LBT, initially designed for optical microscopes, has been applied to astronomy by R. Ragazzoni [19]. The main optical element is a glass prism looking like a pyramid whose vertex lies on the focal plane of the telescope on a reference natural guide star. The four faces of the prism refract the light into four different directions. A collimator intercepts the beam and recreates four images of the pupil of the telescope on a CCD simulating a 4-quadrant sensor.

The position of the four pupils on the detector is a function of the pyramid vertex and the F number of the incident beam. The speckle, that usually characterize the PSF of a seing limited star, are selected by the four faces of the pyramid and the light is turned towards for different direction forming four images of the telescope pupil.

From the analysis of the light distribution on the four pupils is possible to retrive the derivate of the wavefront, than the shape and the aberration correction required. The Pyramid sensor provide several advantagen with respect other classical AO sensor as dempnstrated by MAD [15] and [3]:

- A great advantages of the pyramid sensor is with respect to the Shack-Hartmann (SH) because it allows the possibility to select the sampling of the pupil. Is it possible to map the pupil with a variable spatial and temporal resolution (CCD binning and Hz) in function of the seeing local parameter. The maximum sample is obtained when a sub-aperture correspond to single pixel o the CCD.

- Another great advantage is low Poisson signal to noise ratio S/N with respect to the Shack-Hartmann sensor. The pyramid allows to add optically photons on the CCD and the photon number N increase faster than the Poisson noise that increase as $\sqrt{N}$.

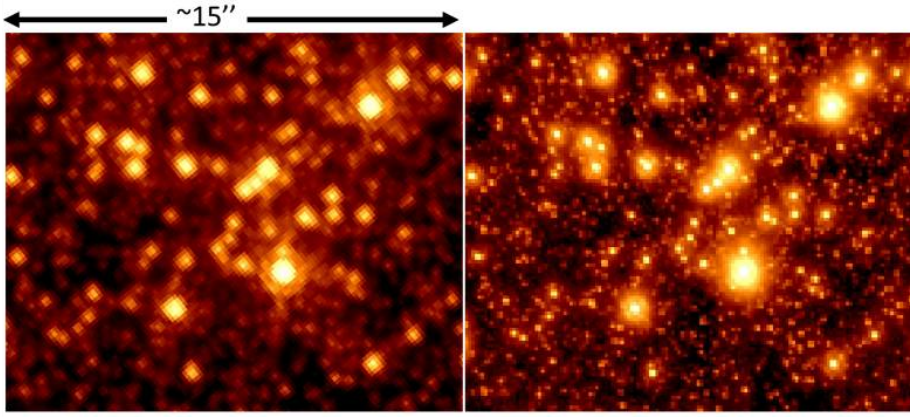

Figure 1.2: *WFPC3 in the H band for Hubble (left) and LBT (right) for a 20 minute and 8minute of exposure time respectively. The LBT and FLAO obtained the results with a seeing of 0.7" and a limit R_{mag}=11.5. The sampling of the pupill is 15x15 sub-apertures, the correction frequency is 0.5kHz with 153 corrected modes.*

- Is it also possible to adjust the sensitivity of the Pyramid sensor (not possible with SH) in relation to the degree of correction to the wavefront. This feature coupled with a closed loop, can improve performance. As the correction of wave fronts becomes more accurate, there is a decrease of the size of the star on top of pyramid and this increases the sensitivity of the sensor [7].

- A corrected star means a more dense PSF[1] increase the limit magnitude for the reference star of a factor two with respect to the SH.

However, a to high sensitivity of the pyramid could decrease the sensor performances. It could happen when the size of the star on top of the pyramid became as small as the diffraction limit a sudden atmospherical fluctuation can move the spot outside the sensor acquisition range causing a consequent failure of the correction of the wavefront.

The non corrected turbulence enlarge the PSF of the spot and the sensor can restart to implement the correction. To avoid too frequent oscillations is possible to decrease the sensitivity of some pyramids by using a diffuser to their culmination or applying a modulation (ie, an oscillating movement of the PSF around the vertex) with higher frequency wrt the reading velocity of the sensor.

On NIRVANA is used a similar concept based on the turbulence properties described by the kolmogorov theory [14]. The observed intensity turbulence depends on the wave observing wave length $\lambda^{-11/6}$. This means that a good correction in the IR is not good at visible wave length [22]. On this relation are designed the GWS and the MHWS. The sensors aquisition signal is in the visible band while the correction is done for the IR wave front. In such condition the IR-PSF is diffraction limit (or close to) while the VIS-PSF is partially uncorrected. The uncorrected PSF sostitute previously suggest pyramid modulation [16].

The adaptive optics Multi-conjugate (MCAO) is a technique introduced by Beckers [4] and based on the principle of using more than one reference star to

[1]Is it possible to reach a Strell ratio up to 80% which is close to the resolution theoretical limit

measure the turbulence in several directions. A classical adaptive optics limit is, in fact, due to small size of the corrected field of view [20].

It is necessary to have a reference source as close as possible to the scientific object almost into the isoplanatic angle (region where the turbulence can be defined as constant). Often also the brightness of the reference star is not sufficient to obtain a good correction even within this angle.

With respect to the Star Oriented SOAO technique (total correction of the turbulence on the line of sight) the MCAO represent an opposite concept. MCAO instead observing a single star, measure and observe a single layer. It is therefore possible to use more star to observe and correct more layers with appropriate Deformable mirrors (DM).

1.2 MCAO Technique

A MCAO adaptive optics system [4] uses a sensor that is conjugated with a DM. The sensor could be placed in the pupil plane of the telescope observing the conjugated layer at entrance pupil of the telescope. The corresponding DM should so placed in the same conjugated plane. Is necessary tu reproduce twice this region into the light optical path in order to place the the DM in the first plane and the sensor in the second one (closed loop[2] configuration [8]). In this configuration the sensor can measure the turbulence introduced near the pupil of the telescope, the so called Ground Layer Turbulence. A second sensor can measure independently the high altitude layer as happen in NIRVANA for the MHWS. Generally speaking has been observed that the most contribute comes by Ground layers. The height of conjugation of the DM does not coincide exactly with the layer of most turbulent, but coincides with the height which minimizes the residual correction. In other words, a sensor conjugated to a certain height can observe also low turbulence frequencies of the near layers[3]that appear blurred over the sensor. The reconstruction of the turbulence on the different layers can be obtained by two established techniques:

- Star Oriented (SO)
- Layer Oriented (LO)

In the first case the number of sensors is equal to the number of reference stars and reconstruction of the turbulence is done numerically by the sum of the signals received from each sensor. Since the sum is the RON, the S/N ratio does not change, and there are no improvements by increasing the number of stars. in a more realistic case the optically sum of the signals happen on a single sensor in order to increase the S/N proportionally with number of stars. The Star-oriented method is called "global reconstruction" and uses many sensors as many are the stars of the field you want to use to produce a map of the turbulence A computer program analyzes the data collected by each sensor and completely rebuild the structure of the atmosphere, calculates the necessary correction and sends it to the deformable mirrors conjugated atmospheric layers. This method has the the same magnitude limit adaptive optics. In addition the amount of data collected requires a big processing time and a greater capacity computer calculation. The layer oriented technique, however, uses many sensors as are the turbulent layers. Each detector is coupled to a layer where is placed

[2]In this configuration the sensor iterate the measurement on a wave front partially corrected. By the iterated measurement of residuals it is possible to reach high correction in few cycle

[3]The focal deep is bounded with the field of view of the sensor itself. A wide angle correction reduce the focus deep of the sensor and the correction is possible only for low orders.

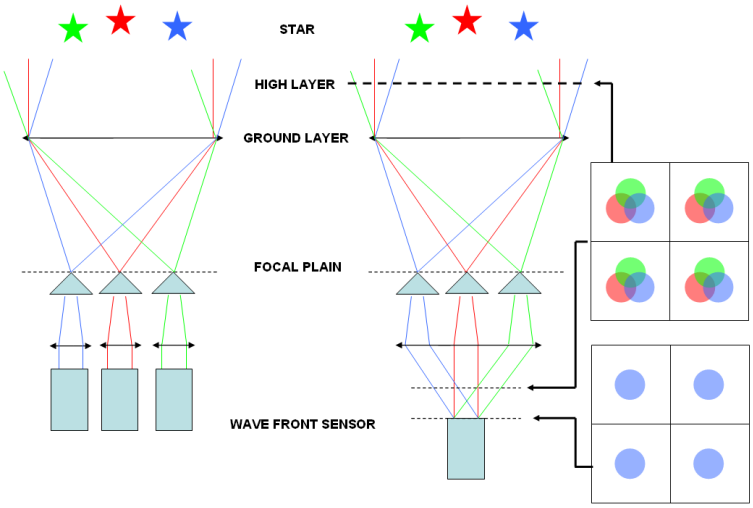

Figure 1.3: *In the left figure is shown the Star Oriented technique: the number of sensors is equal to the number of reference stars and reconstruction of the turbulence is done numerically by the sum of the signals received from each sensor. Is also summed the RON and the S/N ratio doesn't change for an improvements of the number of stars. In the right the Layer Oriented technique where the sum of the signals is done optically on a single sensor increasing S/N proportionally with number of stars.*

a deformable mirror(DM), and everyone collects at the same time the signal coming from all the reference stars. The co-add of the light is optical (but could be done via software) with the advantage to decrease the readout noise and to increase the limit magnitude. In this case the correction doesn't depend on magnitude of a single star, but on the sum of the magnitudes of the reference stars. Each star should reach a pyramid sensor.

The light coming from the same face of the used pyramids is optically superimposed on the CCD where are formed four pupils. To measure an high layer it is necessary to conjugate the sensor that height by a shift from the pupil plane.

The light footprint of the stars is not here completely superimposed for geometrical reasons. The so called metapupil is well corrected by the sensor in the common intersection where the optical co-add is efficient.

An advantage of the LO is the possibility to vary the height of conjugation, the pupil or metapupil sampling, and the temporal acquisition frequencies according to the spatial and temporal characteristics of turbulence.

Thanks to these characteristics is no longer necessary to make a correction on a column atmosphere (as it was for the classical adaptive optics), but it could be sufficient to correct several layers in different independent loops.

1.3 Multiple Field of View

As mentioned previously, the MCAO method [4] can be used to correct simultaneously in multiple layers of atmospheric turbulence. The concept of the Multiple Field of View (MFoV) is to divide the light from the reference stars in two fields of view that are observed separately by two wavefront sensors [18]. In NIRVANA the GWS and MHWS sensors are designed according to the

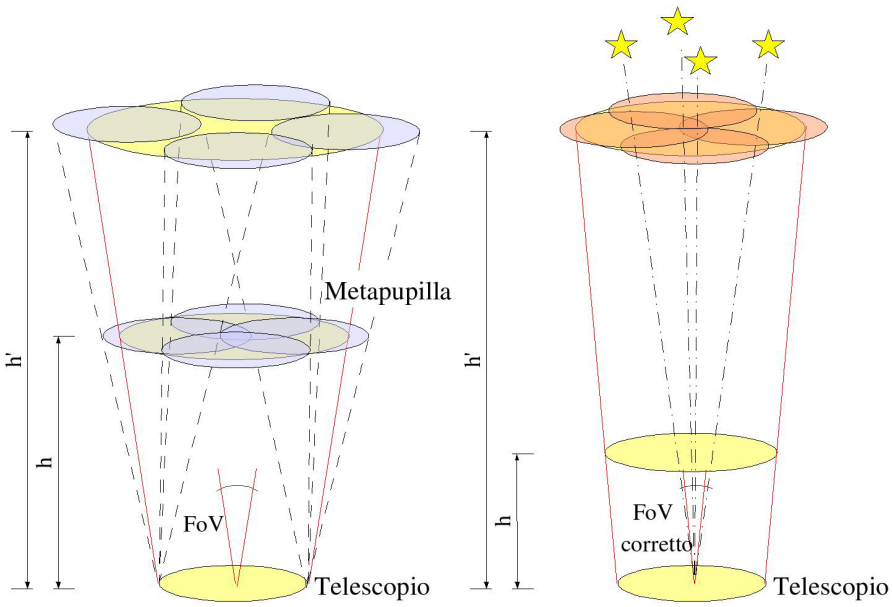

Figure 1.4: *on the right the field of view of 6x6arcminute of the GWS. The light from from stars overlaps allowing a good correction of the pupil, turbulence. On the left is represented the increasing pupils separation with the altitude. For angles beyond 2' in the MHWS the pupils do not overlap and optical co-add is not efficient anymore.*

scheme of the MFoV [11]:

- Ground-Layer Wave Front Sensor (GWS), which uses an annular area from 2' to 6' diameter, to correct the Ground layers.
- The Mid-High Wave Front Sensor (MHWS), which uses a field of 2'in diameter, for correct the layers at the higher elevation, between 4 and 20 km.

The distortion introduced on the wavefront from the Ground layers is the same for all stars because the pupils are perfectly superimposed. For this reason we can obtain information on the perturbation to the ground based on stars guides angularly away from the object of science.

For the high-altitude turbulence the reference star are selected in a small region close the scientific object in order to have a good metapupil coverage. Beyond a certain critical angle is loosed the superposition of the pupils and, in the central area the density of photons doesn't increase significantly [2]. The critical angle depends on the turbulent layer altitude and the diameter D of the telescope.

For the null altitude which is for the ground layer, there is no theoretical limits. The overlap of the pupils is perfect for the Ground Layer, while it decreases for layers at high altitude. The LBT design MFoV concept is to choose reference stars from a wide field of view of 6x6arcminute to correct the turbulence of the Ground Layer. The focal depth in the case of GWS is less than that in the case of MHWS, This means that for the GWS the turbulent layers are although very close and blurred. In the case of MHWS the situation is reversed because the field of view is smaller, and the focal depth is greater

and it is able to correct partially the closer turbulent layers [24].

Chapter 2

Two K-M unit for LBT

The optical derotator consists of three mirrors, M1, M2 and M3 mounted together in a stiff and stable and rotating stage that define the internal optical axis. The derotator is also called K-Mirror (KM) and its name arise from the k optical configuration of the mirrors in the instrumental design. The principal characteristic of a derotator is to rotate the incoming wavefront of and angle that is the double wrt the rotation angle of the three mirrors.

LBT provides an altazimutal mount that produces a rotation of the focal plane during the tracking. To fix the FoV on the detector to solution are allowed:

- Rotating the detector with the same angular velocity of the FoV.
- Using a K-mirror to introduce a contra-rotation of the FoV.

Both concept are used for the wave front sensor of LBT. Between the two big primary mirrors of the telescope is placed LINC-NIRVANA which is an interferometer and beam combiner with an MCAO-LO Adaptive Optics system. Nirvana is divided into two parts connected respectively with the two apertures of the telescope. The connection of the two signal will occur in the Fizeau interferometric configuration. Four wavefront sensors (two for one side of NIRVANA) measure the atmospheric turbulence using up to 12 reference natural guide stars. Two GWSs measure the Ground Layer turbulence and two MHWSs measure the Hig Layer Turbulence. The GWS sensor can rotate around its optical axis to follow the rotation of the focal plane of LBT while the MHWS are fixed to the carbon fiber bench. It's necessary to maintain fixed the FoV on the two MHWSs using an optical derotator for each sensor. To compensate for the rotation of the sky, one KM is placed and aligned with the optical axis defined by the MHWS and the FP/20 Camera. This unit lies between the first and second lens groups of the FP/20 Camera, closer to the second one. The KM provide several adjustment systems for the internal alignment and a different one for the alignment wtt the FP/20 Camera (named external alignment). The following sections will describe several phases of the construction of the two k-mirrors starting from the requirements of the instrument, the design, the mounting, the internal alignment and test done. Both instruments are now in the laboratory of the Max Planck Institute for Astronomy in Heidelberg (Germany) for the final acceptance tests.

2.1 Requirements

The KMs have to rotate during a scientific exposure to introduce a contro-rotation of the field of view of the MHWS wave front sensor. To have the correct

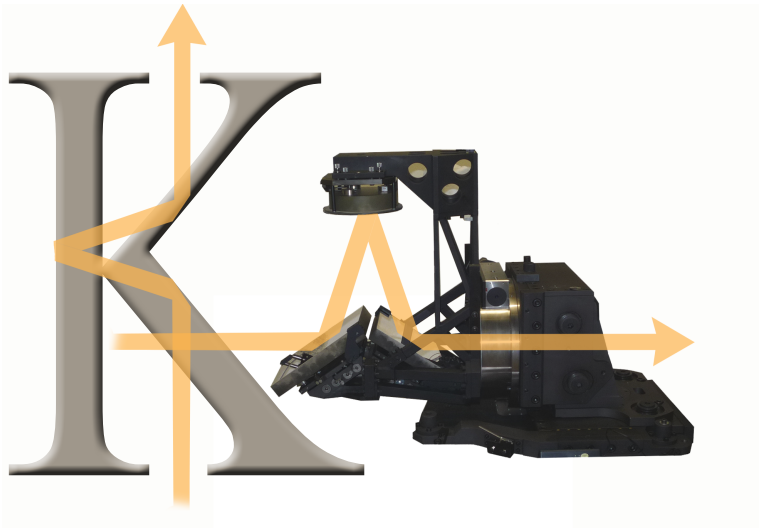

Figure 2.1: *The K-mirror picture with the explanation of the name origin due to the K configuration of the three mirrors.*

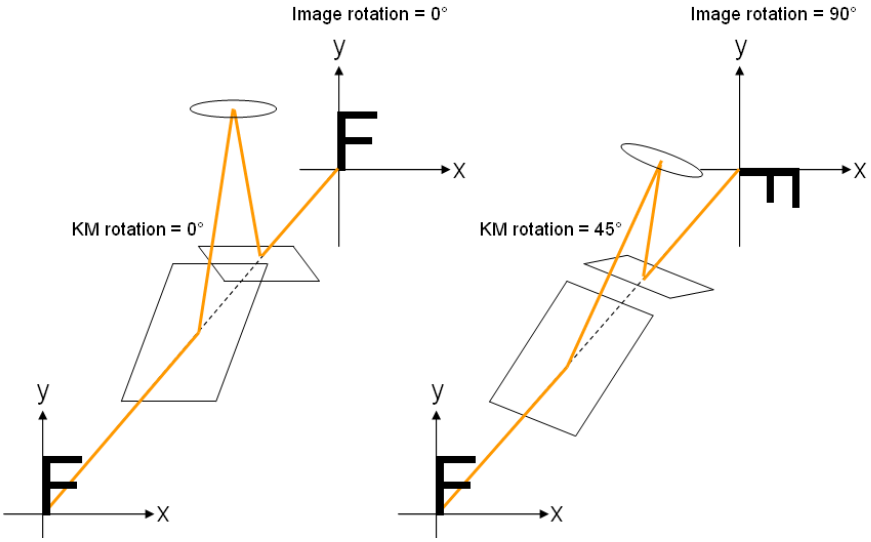

Figure 2.2: *A rotation of 45deg of the KM system around its optical axis produces a rotation of the image of the double angle of 90deg.*

Item	Specification
Reference wavelength	0.8 µm
Wavelength range	0.6 − 0.9 µm
Operating temperature	-15°C − +20°C
Storage temperature	-30°C − +50°C
Operating pressure	500 − 600 Torr
Storage pressure	500 − 760 Torr
Operating humidity	0% − 95% without condensation
Storage humidity	0% − 100%

Figure 2.3: *The environmental specifications and general definitions for the KM unit.*

response from the the sensor its necessary to fulfill the design requirements. The common concept to use a monolithic glass fused prism design in place of such KM was neglected because of dimension, weight, costs and technological limitation. A better solution as been identified in a tre separate mirrors configuration.

2.1.1 Decentering of the Chief Ray

The first important requirment for the KM is the decentering of the beam transmitted. The decentering o the beam produces a rigid shift of the stars on the MHWS focal plane, forcing the SEs of the MHWS to be re-centered continuously on the reference stars instead only at the beginning of each exposure (through the patrol camera input).

A rigid shift of the stars on the FP during a single exposure produces a tilt signal on the WFS, which is the same for all the reference stars and can be retrieved and used as a feedback to reposition the SEs with a pre-determined frequency during one exposure.

A reasonable stars rigid shift after which the SEs would not need to be repositioned is 1/10 of FoV for a single SE, that is to say 0.11 arcsec, corresponding to 88μm on the FP20 focal plane. Moreover, this acceptable decenter should be somehow divided between the KM and the FP20 optics error budgets.

Assuming the same contribution for the KM and the FP20, quadratically summed, the KM acceptable chief ray decentering would become 62μm. Considering that this requirement on the decentering should include bearing wobble, alignment results, thermal effects and flexures, a 62μm requirement seems to be too strict to be fulfilled [5].

A SE optional recentering during an exposure is, then, required to be implemented at a SW level. A realistically achievable decentering requirement could be, instead, 100μm (this value was the original specification). Since the KM is placed in between the FP20 optics, the decentering of the chief ray slightly affects also the pupil position, because the beam reaches the SE entrance focal plane with a little tilt, but this effect, for a beam decentering lower than 300μm, is negligible, resulting in a shift of less than 1/20 of subaperture in the 1x1 binning mode.

Decentering requirement: 62µm without SE re-centering during one exposure 100µm with SE re-centering during one exposure.

Conjugation height (c.h.)	Comment	Metapupil diameter
0 km	LINC mode c.h.	18 pixel
4 km	MHWS lower c.h.	24 pixel
7.1 km	DM actual c.h.	27 pixel
15 km	MHWS higher c.h.	38 pixel

Figure 2.4: *Metapupil diameter on the MHWS CCD at different conjugation heights. In the LINC mode the MHWS is conjugated at 0km, the MHWS possible conjugation range is between 4km to 15km (original conjugation range for the DM, when it was expected to be movable), while 7.1km is the actual conjugation range of the DM correcting the high layer perturbation.*

2.1.2 Telecentricity Angle

A deflection of the beam produce a deviation from the required telecentricity angle of the beam at the level of the MHWS entrance focal plane. This fact produce a rigid shift of the 4 pupils on the CCD, according to the following expression:

$$Tilt(rad) f_{PRI}/K_{SE} = pupil\ shift \tag{2.1.2.1}$$

where $fPRI$ is the equivalent focal length of the $MHWS$ Pupil Re-Imager, and k_{SE} is the Star Enlarger enlarging factor. Since, in the MHWS, fPRI = 99mm and kSE = 11.25, the resulting pupil shift for a given tilt is:

$$pupil\ shift(microns) = 8.8\text{x}10^3 Tilt(rad) \tag{2.1.2.2}$$

Considering a reasonably acceptable rigid pupil shift of a 1/10 of sub-aperture of the WFS, the corresponding tilt depends of course on the sub-aperture dimension on the CCD, which is varying accordingly to the binning mode required for each considered conjugation height.

Considering a conjugation height of 0km, as for the LINC mode, the 1x1 binning mode is required (by design the pupil image has a diameter of 18.3 pixels, with a required minimum metapupil sampling of 11x11 sub-apertures. In such a case, the sub-aperture diameter is the CCD39 pixelsize, corresponding to $24\mu m$, and resulting in a 56arcsec tilt to shift the pupils of about a tenth of sub-aperture.

Considering, instead, the 7.1km conjugation of the MHWS in linc-NIRVANA mode, the metapupil diameter becomes 27 pixels, and a 2x2 binning would still allow the minimum required pupil sampling. In a 2x2 binning mode the acceptable tilt introduced before the FP20 focal plane becomes $112 arcsec$.

The first equation (eq4.7.0.3) would apply perfectly if the KM was the last optical system before the MHWS entrance focal plane. In the real case in which the KM is placed in between the FP20 optics, the deflection of the chief ray affects the pupil position slightly less than what said before, and a non-negligible rigid shift of the stars on the focal plane occurs too e.g. a 50arcsec deflection of the beam at the level of KM, would cause a 150um shift of the stars on the SE entrance focal plane.

Quadratically combining this effect with the shift due to chief ray decentering, the overall shift to take into account is $\sqrt{100^2 + 150^2} = 180mm$, which corresponds to 1/5 of the SE FoV.

Binning mode	Total acceptable tilt @FP20 focal plane	KM component
1x1	<56”	<40”
2x2	<112”	<80”

Figure 2.5: *KM acceptable chief ray deflection, accordingly to different binning modes.*

A SE adjustment during an exposure may turn out to be necessary, and it is required to be implemented at a SW level.

Requirement: 40arcsec for LINC mode 80arcsec for LINC-NIRVANA mode

2.1.3 Strehl Ratio

The required Strehl Ratio (SR) is 90% for the KM + FP20 camera system. Because of that, the KM Strehl Ratio will be kept as high as possible, in order to match this combined requirement and leave a not so strict requirement in terms of SR to the FP20 camera. We decided to fix the minimum of KM Strehl Ratio to 95%, supposing an analogous value for the FP20 camera.

2.1.4 Mirrors Flatness

An inverse sensitivity analysis has been performed in order to evaluate the requirements on the flatness. The purpose is to define the maximum surface RMS (in waves) which is required to guarantee a SR better than 95%. Notice that the large angle of incidence on M1 and M2 (55deg) leads to a less stringent requirement on the surface flatness, compared to M2, whose angle of incidence is 20deg. The mirror flatness is estimated over the optically clear area, the Strehl is estimated at the wavelength of 1μm and using only the portion of the mirror surface interested by the footprint of a single beam. The used reference wavelength is 800 nm, and the results are the following:

- RMS M1: 25 nm (l/32)
- RMS M2: 14 nm (l/57)
- RMS M3: 24 nm (l/33)

2.1.5 Mirrors Reflectivity

The required reflectivity for each of the three KM mirror is 96%.

2.1.6 Bearing Motion Requirements

The main KM motion requirements were calculated and can be summarized as follows: the minimum step motion required at the level of the flange of the bearing can be calculated as:

- where r is the radius of the focal plane of the camera, Δ is the point spread function radius (at 0.6μm, assuming diffraction limited conditions). Using the values of the camera, δ turns out to be about 0.008°.

$$\delta = \frac{1}{2} \cdot \frac{360}{2\pi r} \cdot \Delta \tag{2.1.6.1}$$

Bearing minimum incremental motion: 0.008°

- The velocity and acceleration of the K-mirror can be evaluated by studying the field motion as a function of the object celestial coordinates (Right Ascension and Declination) and the UT time. If L is the observer latitude (32.7N), the star field is centered at a zenith distance z and azimuth A, then the field will rotate at a rate given by:

$$\frac{\delta\eta}{\delta t} = -0.262 \frac{cos(L)cos(A)}{cos(z)} [rad/hr] \tag{2.1.6.2}$$

As for any altazimutal mount, a cone of avoidance must be defined, i.e. the minimum angular distance between the pointing direction and the zenith: in such angle was assumed to be 6arcminute. The resulting maximum angular velocity (accordingly to (4.7.0.4), with $A = 90°$ and $z = 90° - 6arcminute = 89.9°$) is 2.0deg/s and the maximum acceleration obtained taking into account for the variation of A and z with time was $0.35 deg/s^2$.

Maximum derotation angular velocity: 2 deg/s

Maximum derotation angular acceleration: 0.35 deg/s^2

- Motor power consumption: motor power consumption is required to be low to avoid the heat dissipated by the motor to generate turbulence just before the MHWS, leading to a loss of performances of the adaptive optics system. A power consumption larger than 2W would require a cooler.

Power consumption: $\leq 2W$

2.1.7 Internal Optical Path

The distance between the three mirrors of the KM, namely its internal optical path (nominally, 640mm), is strictly correlated to the nominal distance between the vertexes of M1 and M3 (by design, 218.89mm), because the real optical path added between the FP20 optics by the KM itself is the difference between those 2 values: 640 - 218.89 = 421.11±1mm (additional optical path). This value is important since, even if it has no optical power, the KM will be inserted in a position inside the FP20 camera in which the beam is focussing, so a non-conformance with the expected additional optical path would translate in a de-focus on the MHWS. The tolerance in the additional optical path comes from

the MHWS position adjustment range, which is 2mm. All these considerations lead to the following requirement:

Additional optical path: 421.11±1mm

2.1.8 Adjustment Travels

Adjustment travel ranges have been selected to be reasonably wide to properly position the KM on LINC-NIRVANA optical bench and to align it with respect to the FP20 camera (external alignment).

- **Lateral and Vertical Adjustment Travel:** $5mm$
- **Tip-Tilt Adjustment Travel:** $0.5°$

2.1.9 Adjustment Resolutions

Adjustment minimum incremental steps have to be reasonably smaller than the precision required in positioning and aligning the system with respect to LINC-NIRVANA optical bench. Both tip-tilt and shift adjustment resolutions directly derive from the chief ray deflection and decentering requirements, reduced of a factor 10.

- **Lateral and Vertical Adjustment Travel: 10μm**
- **Tip-tilt Adjustment Resolution: goal 5".**

A relaxed 10arcsec resolution is still accepted, due to KM adjustment system manufacturable)

Requirement	
Deflection of the chief ray	40 arcsec
Decentering of the chief ray	100 µm
M1 Flatness	λ/35 nm RMS @ 800 nm
M2 Flatness	λ/60 nm RMS @ 800 nm
M3 Flatness	λ/35 nm RMS @ 800 nm
Mirrors Reflectivity	> 96%
Maximum derotation angular velocity	2.0 deg/s
Maximum derotation angular acceleration	0.35 deg/s^2
Bearing motor power consumption	< 2W
Bearing minimum incremental motion	0.008 deg
Strehl Ratio	SR > 95% @ 1µm wavelength
Additional optical path	421 ± 1 mm
Lateral and Vertical Adjustment Travel	±5mm
Lateral and Vertical Adjustment Resolution	10 µm
Tip-tilt Adjustment Travel	±0.5deg
Tip-tilt Adjustment Resolution	10" (goal 5")

Figure 2.6: *Tabelle with the requirements for the two K-mirrors unit. Deflection and decentering are to be intended as the maximum (Peak to Valley)end through a contiguous span of* $\pm 30^\circ$ *in the pupil plane, corresponding to* $\pm 15^\circ$ *of rotation of the physical frame of the K-mirror.*

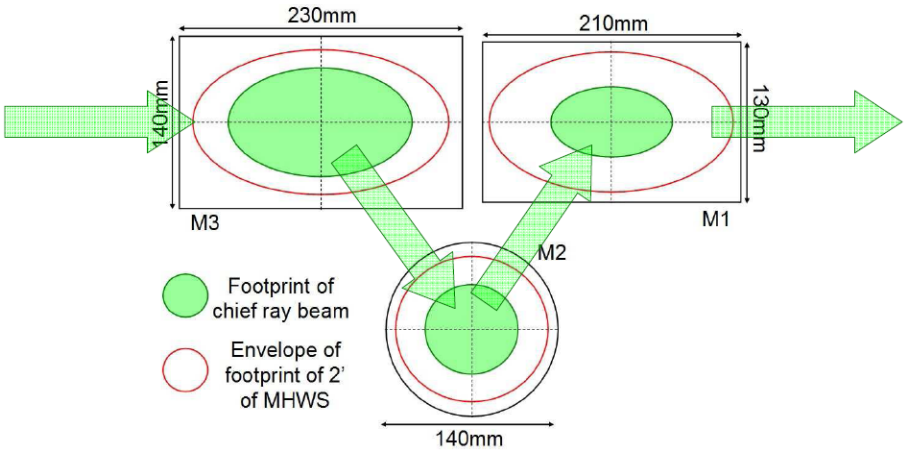

Figure 2.7: *Required dimensions of the mirrors. Green and red ellipses represent, respectively, the footprints of the chief ray beam and their envelopes considering MHWS 2 FoV. Green arrows show the light path direction.*

2.2 Design

The mirrors of figure 2.7 are numbered from the closest one to the KM rotating bearing (M1) to the farthest one (M3)while the position angle is defined between a line perpendicular to M2 and LN optical bench. The position angle value is 0° when M2 is perpendicular to the optical bench. Then, rotating it clockwise, looking at the entrance pupil of the FP20 camera through the KM, it is 90° when M2 is parallel to the optical bench, and 180° when perpendicular again to the optical bench.

The values expressed in figure 2.8 give the torque of M standard screws according to DIN ISO 261 for metric threading, DIN EN ISO 4762, DIN EN ISO 4032, DIN EN ISO 4014 and DIN 931-2,6912,7984 and 7990 for the screws head pull. They will be considered to tight all screws in KM, except the screws used for the adjustment of tip tilt, and decenter, in particular, the ones used for the alignment of M1, M2 and M3 and the ones on the base-plate that will be used to align the KM to the FP20. Moreover also the grubs screwed in the base plate under the bearing and on the side of the base plate need to be less tight, because they are used just to make more rigid the mechanical guide of the decenter adjustment.

The KM is shipped within a plastic box. The KM is fixed to a stainless steel plate placed inside the box with four M12 nuts. The plate is fixed to supports with six bolts and the supports are linked to the box. It is recommended to use a fork lift having arms whose distance can be adjusted, to lift the box evenly from its shorter side. Alternatively the box can be fixed to a pallet (for instance by using straps placed in such a way to prevent relative displacement of the box with respect to the pallet) and then a fork lift can be used to move the whole assembly.

A detailed description of the packing / unpacking procedure is given, focusing on:

- list of tools to pack the system
- sequence of operations to properly pack the system

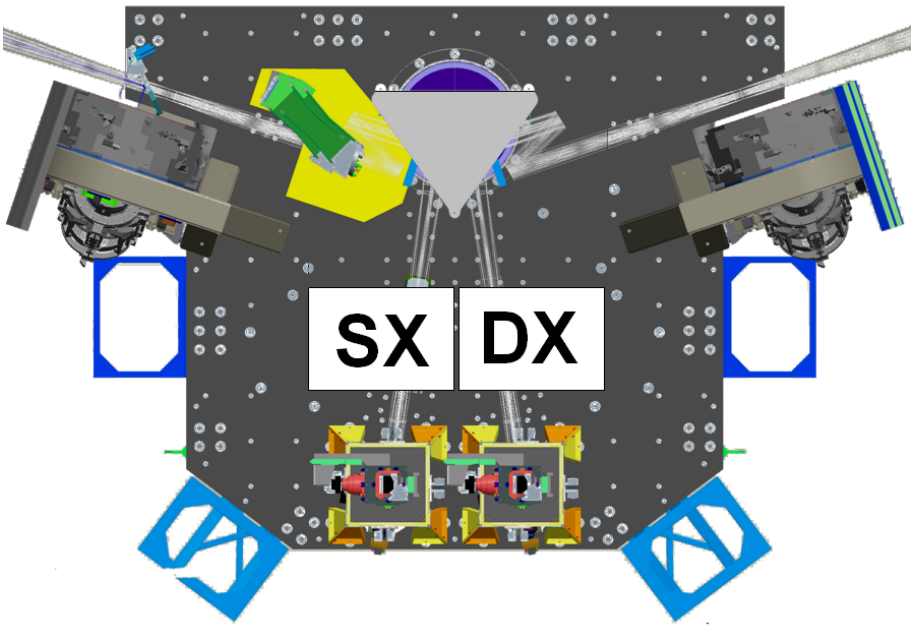

Figure 2.8: *The optical bench of LINCK-NIRVANA with the derotator position signed for both units..*

- sequence of operations to properly unpack the system

2.2.1 Packing

It is assumed that the starting point is with the KM placed over an optical bench. It is necessary to have the following tools:

1. Mirror covers
2. 4 lift bars 4 M12 screws and washers
3. Lift plate
4. M12 eyebolt
5. Small crane or overhead traveling crane
6. Fork lift, pallet
7. Belts
8. start rotating the KM bearing until M2 reflective surface is orthogonal to the direction of gravity
9. Protect the mirrors with optical paper and covers
10. Remove the box cover
11. Mount the threaded bars on the KM (completely assembled)
12. Mount the lifting plate on the threaded bars and fix them with 4 M12 screws + washers

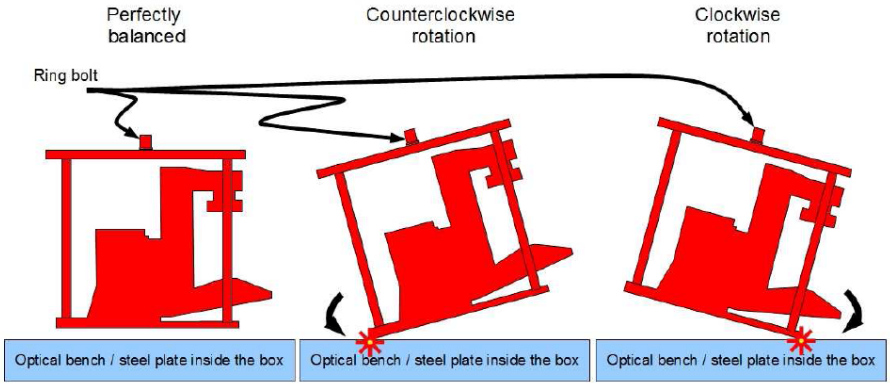

Figure 2.9: *rotation of the KM with counterweight not properly mounted. Repositioning of the eyebolt is needed.*

13. Insert the eyebolt on one threaded hole of the lifting plate (central one is suggested)
14. Attach a belt or a steel cable to the eyebolt and to the crane hook
15. Unscrew the bolts fixing the KM to the optical bench
16. Tighten the cable/belt using the crane
17. Slightly raise the KM
18. Verify whether any rotation of the KM occurs
19. If a rotation occurs, slowly bring down the KM onto the bench
20. Adjust the position of the eyebolt on the lifting plate and repeat from 9 to 10. Repeat until the KM is in equilibrium
21. Lift up the KM and move it towards the box
22. Place the KM inside the box

2.2.2 Unpacking

It is assumed that the starting point is with the KM placed inside the box and the box is fixed to a pallet with belts. It is necessary to have a small crane or overhead traveling crane, a fork lift, pallet, a steel cable and a belt. N.B. Usually small cranes like do not allow to put the KM box between the two legs. Two situations typically occur, depending on the type of available crane.

If it is not possible to extend the arm of the crane to place the KM inside the box, with the box placed outside the legs of the crane, since the maximum load of the crane is too low or the distance between crane's legs is smaller than the shortest side of the box. Then:

1. Remove the belts
2. Remove the box cover
3. Place the pallet box assembly over crane's legs with the fork lift.

4. Attach the eyebolt to the lifting plate
5. Attach the steel cable to the eyebolt and to the crane.
6. Tighten the cables.
7. Loosen the bolts which fix the KM to the steel plate inside the box.
8. If no other modification occurred after packing (like removal or components/subsystems from the KM) it is not necessary to change the position of the eyebolt.
9. Slightly remove the bolts which fix the KM to the steel plate
10. Lift the KM (completely assembled) with the small crane
11. Remove the box from the legs of the crane
12. Place the KM over the optical bench, following the same procedure used to put it inside the box.
13. The crane maximum load with the arm fully extended is high enough to place the KM inside the box, with the box outside the legs of the crane.
14. In this case it is not necessary to place the pallet over the legs of the crane.
15. Then, the previous procedure shall be used, with the pallet placed outside the legs of the crane.

If the crane maximum load with the arm fully extended is high enough, place the KM inside the box, with the box outside the legs of the crane.

- In this case it is not necessary to place the pallet over the legs of the crane.
- Then, the previous procedure shall be used, with the pallet placed outside the legs of the crane.

2.2.3 Handling Procedures

The plate to lift the km up is fixed to the KM through four bars, threaded at one end and with a threaded hole on the other side. The threaded part of the bar is screwed to the KM base-plate, while the threaded hole on the other side is used to fix the lift plate. This plate is provided with several threaded holes: one eyebolt placed in one hole is sufficient to lift the KM. The selection of the hole depends on centre of mass of the KM.

The centre of mass position might change in case of KM maintenance (for instance removal of one or more mirrors). For that reason several holes have been made on the plate. A practical procedure is used to verify what is the best position to place the eyebolt:

- the bars, plate and ring bolt are mounted
- the KM assembly is lifted
- a possible rotation of the KM is observed
- if any rotation occurs, the KM is taken down and the position of the eyebolt is changed
- the operation is repeated until an acceptable balance of the assembly is reached

As during the handling operation of the KM the base-plate can hardly hit the supporting surface (optical bench), it is recommended to place the KM over a surface with comparable hardness or suitable protected with a thick layer of shock-absorbing material.

2.2.4 Assembling and Installing

The KM instrument is subdivided into seven sub-systems:

- base-plate
- bearing
- motor assembly
- frame
- M1 unit
- M2 unit
- M3 unit

2.2.5 KM Mounting and Dismounting Procedure

First, a mounting procedure KM sub-systems is described; then the mounting procedure of each subsystem which is supposed to need maintenance during its life is described. Such procedures indicated throughout this document should be followed during any repairing or replacing of one of the KM components. Unless otherwise specified dismounting procedures are the same as mounting procedures but in reverse order.

1. *Base-plate mounting*

Fix the base-plate to a bench (LN optical bench, standard optical bench, box steel plate) The base-plate is fixed to the interface columns (see AD2) on bench, or to the threaded supports in the box, using the attachment points, and fastening with a washer and and an M12 nut.

2. *Bearing mounting*

The bearing is mounted on three points over the base-plate. Use 3 bolts M6x25 to fix the rotation stage. The rotation stage must be mounted oriented with the motor in the upper position.

3. *Mounting of the motor on the rotation stage*

The motor is fixed to the bearing shaft through a flexible coupler. The flexible coupler is tightened to the bearing shaft and to the motor shaft with two grub screws, while the motor mount is fixed to the bearing body with four M4 bolts. It is sufficient to loosen the screws of the coupler on the side of the bearing and to remove the four bolts to dismount the subsystem from the bearing. The opposite for mounting. There is a hole to fix the upper screw (screw1) as first. The position of the motor shaft shall be adjusted by powering the motor to make the screw and the hole position coincident. To mount the subsystem to the bearing:

1. power the motor and rotate it until the position of the hole on the motor mount is coincident with the screw1 on the coupler.
2. Loosen the screw without removing it.
3. Insert the coupler on the bearing shaft
4. Slightly squeeze the screw of the coupler
5. Insert the four bolts C and tighten them a bit
6. Tighten the grub screw 1
7. Tighten the four bolts.

4. *Mounting of the KM frame*

It is recommended the operation to be done by two people and not to lift the frame taking it with a belt or a cable from its upper part. The frame is mounted on the bearing using the three holes. The bolts must be fixed at the lower position of the holes. The safer procedure to mount the frame is the following:

1. One person takes the frame from the lower part, which is more solid
2. A second person inserts one bolt (preferably the uppermost one)
3. The position of the frame over the bearing is adjusted until the three bolts entered and are fixed

5. *Mounting of M1 unit*

M1 unit is the smallest one among the two rectangular mirror sub-units. To properly mount M1 unit the following tools are necessary:

- Six special M10 bolts
- Proper allen key

Insert the unit on its proper position of the frame, close to the bearing. Take care to avoid hits of the mirror onto the frame. The holes on the frame structure have been threaded to simplify the mounting procedure. Just place the mirror mount in position and screw the M10 screws into the holes.

6. *Mounting of M2 unit*

M2 unit is mounted on the frame using seven micrometric screws, in a push-pull configuration. Three of the screws are pushing M2 mount, while the other four screws pull it to fix it to the main structure.

7. *Mounting of M3 unit*

To properly mount M3 unit the following tools are necessary:

- Eight special M10 screws

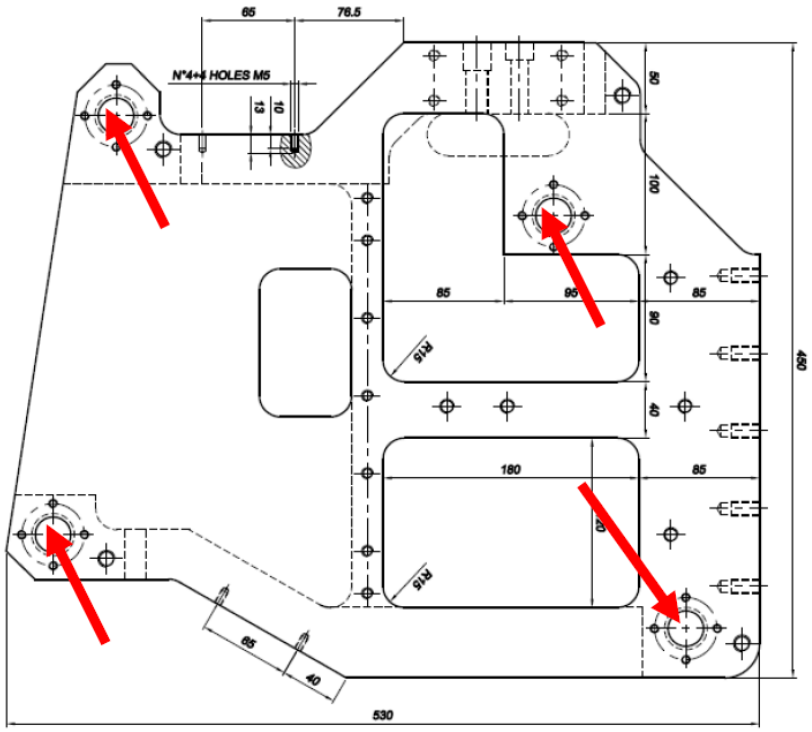

Figure 2.10: *KM Base-plate: the arrows show the attachment points of the base-plate to LN optical bench.*

- Proper allen key

Insert the unit on its proper position of the frame, far from the bearing and screw the M10 screws into the holes. Take care to avoid hits of the mirror onto the frame.

2.2.6 M1 unit assembly/disassembly

Always take care to properly cover and protect the mirror. The unit is assembled in such a way to have the coated surface of mirror, protected with optical paper, laying on a surface. To assemble the sub-system the following procedure shall be followed:

1. The mirror is provided with three pads glued on its rear surface
2. The three shortest bars are vertically screwed on the pads, avoiding torques on the bars using pliers.
3. The three longest bars are laterally screwed on the pads, three nuts are inserted on the outer part of the horizontal bars.
4. The tilting plate is inserted from top and blocked in correspondence of the vertical bars with nuts and lock nuts.
5. The lateral and horizontal bar supports are inserted in correspondence of the horizontal bars and fixed to the tilting plate with proper M4 screws.

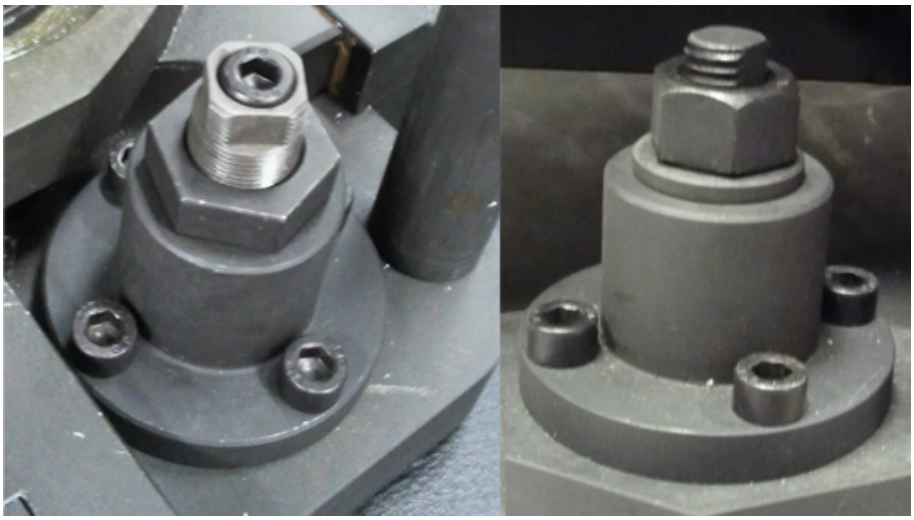

Figure 2.11: *mechanical interface between the KMs baseplate and the optical bench of NIRVANA. Nut and washer used to fasten the base-plate to the optical bench through one of its attachment points. The adjustable bells (two for each unit showed in the left) allows to positioning the instrument on a flat configuration using the four interface columns.*

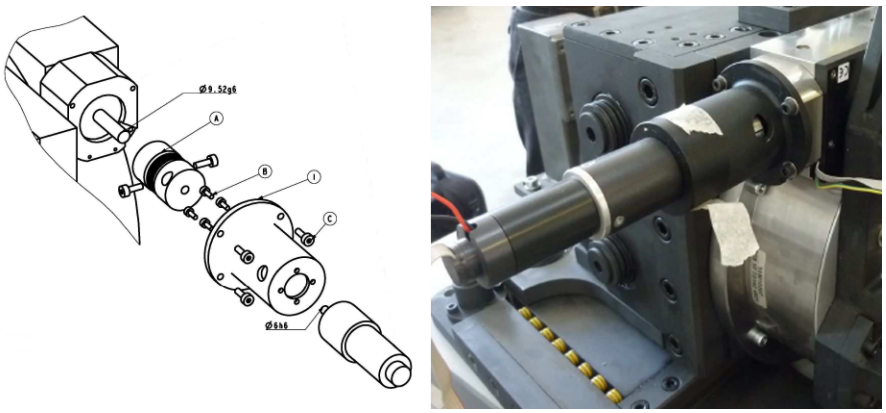

Figure 2.12: *motor subsystem design and mechanical part attached to the bearing.*

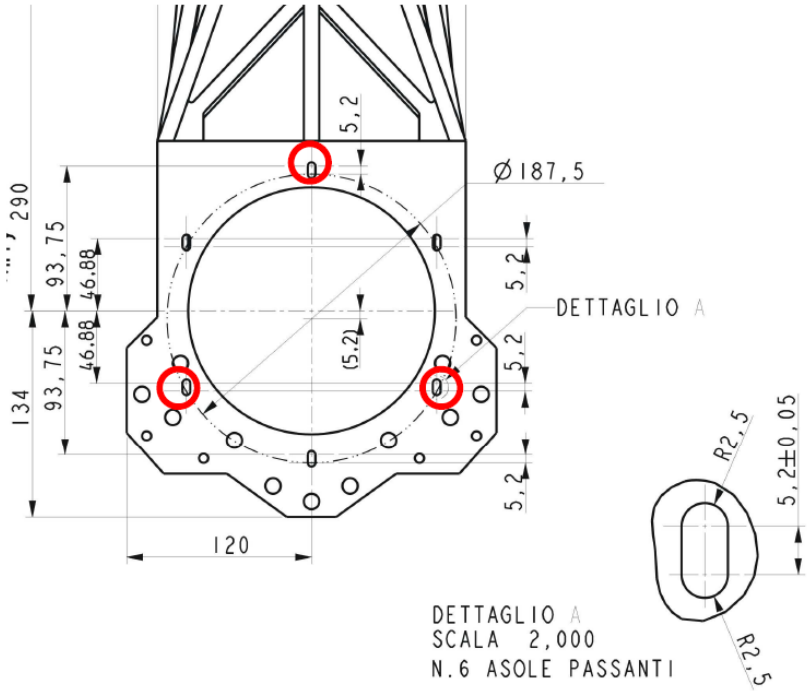

Figure 2.13: *Frame. The mounting holes are the elongated ones, but only the three ones in the red circles have been used to optimize the performances. To have the frame fixed only on 3 points (defining a plane),a washer has been placed between the frame itself and the bearing, in correspondence of each screw. An enlarged image of the hole is shown on the right. The frame shall be mounted at the bottom of the hole.*

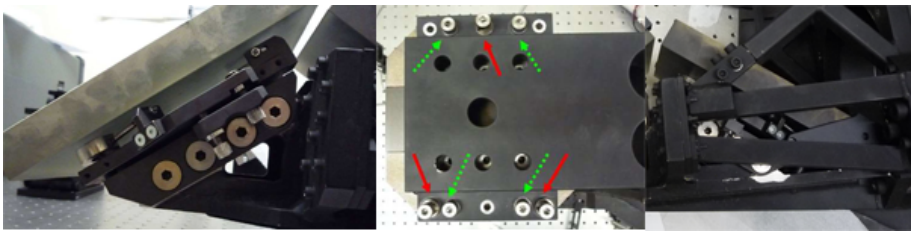

Figure 2.14: *Left: M1 unit mounting concept i, 2 screws are used for each side for tip-tilt regulation. Center: top view of the frame in correspondence with the M2 unit. The red arrows show the pushing micrometric screws, while the green dotted arrows show the pulling screws. Right: M3 unit.*

Figure 2.15: *Some phases of mirrors gluing.*

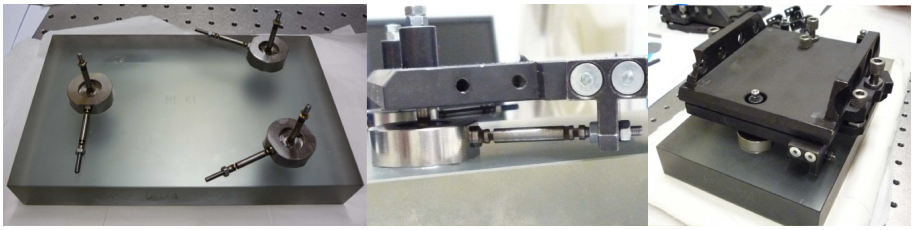

Figure 2.16: *M1 lateral pins (with a nut inserted on the outer end) screwed on the side of the pads. With the tilting plate fixed to the vertical bars with nuts and lock nuts. Connecting the fixing plate to M1 mount: the fixing plate is then used to connect the mount to the frame.*

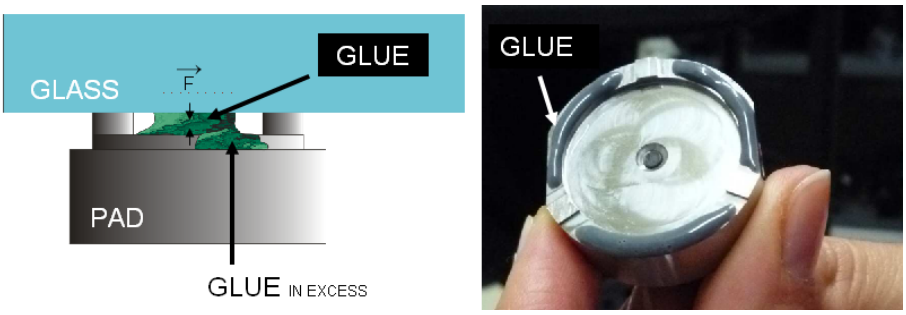

Figure 2.17: *The gluing concept is to keep in touch the upper edge of the invar pad and the backside of the mirror. The glue is placed on the lower edge of the pad but thanks to the surface tension it can reach the glass surface and start curing. The contraction of the glue produce a sort of preload ($\vec{F}$). The pre-load on a small area maintain in contact the pad and the mirror without introducing mechanical stress.*

6. Another plate is assembled: this plate will be fixed to the KM frame, while the rest of the mirror mount is regulated in tip-tilt using three couples of micrometric screws.

7. Safety arms are mounted on two opposite corners of the mirror mount with M4 screws. Reverse the previous operation to disassemble the unit.

2.2.7 M2 unit assembly/disassembly

Always take care to properly cover and protect the mirror. The unit is assembled in such a way to have the coated surface of mirror, protected with optical paper, laying on a surface. To assemble the sub-system the following procedure shall be followed:

1. The mirror is provided with three pads glued on its rear surface

2. The three shortest bars are vertically screwed on the pads, avoiding torques on the bars using pliers

3. The three longest bars are laterally screwed on the pads, three nuts are inserted on the outer end of horizontal bars

Figure 2.18: *M2 unit mounting: the 6 bars are screwed on the pads. M2 with the tilting plate fixed to the horizontal bars with nuts and lock nuts, through bar supports.*

4. The tilting plate is inserted from top and blocked in correspondence of the vertical bars with nuts
5. The lateral and horizontal bar supports are inserted in correspondence of the horizontal bars and fixed to the tilting plate with proper M4 screws.
6. A safety plastic ring is mounted through 4 plastic columns just above M2 mirror (be careful to avoid contact between the mirror and the ring).

To disassemble the sub-system follows the previous steps in reverse order.

2.3 Internal Alignment Procedure

In this section is described the internal alignment procedure used to verify the performance of both K-Ms units. The all KM is mounted and screwed to the optical test bench in four points using special interface plates, which should be disposed on the optical bench as indicated in the following. Alignment Tools:

- Generic lab tools (screwdrivers, hex keys...)
- A laser source ($\lambda = 632.8nm$) equipped with x-y movements
- 1 beam expander (dia.=1inch)
- 1 variable diaphragm (0.5mm-2mm)
- 2 folding mirrors on tip-tilt mounts
- 1 flat mirror (diameter=1inch)
- 1 beam splitter (50:50)
- 1 lens (f =750mm, diameter=1inch) with tip-tilt-x-y movements
- CCD detector (pixelsize=5.2mm) with x-y movements
- Tip-tilt mount to hold a 1inch mirror integral with the rotating bearing
- 1 corner cube (diameter=1inch)
- Generic holders and bases

Figure 2.19: *Interface plates to fix KM to a standard optical bench. They can be fixed to the bench with a maximum of 8 M6 screws, then the interface column will be inserted into the M8 threaded hole.*

2.3.1 Alignment Bench Configuration

In the description below we assume the following coordinate system: z is coincident with the rotation axis of the KM, y is perpendicular to the optical bench, the origin is located at the aperture of the laser source used for the alignment. The configuration of the bench used to align the KM is set as follows (see figures below for more details).

The used setup is divided into two parts: before the K-mirror (accordingly to the light path direction), hereafter bench-side 1, and after the K-mirror, bench-side 2. The two optical setups are used for two main phases of the KM alignment:

- Materialization of the rotating axis
- Alignment of the KM mirrors

Materialization of the Rotating Axis

This setup is aligned on the bench-side 1. A laser beam is expanded using a beam expander. A variable diaphragm, integral with the laser head and the beam expander, selects the inner area of the beam. The whole source is mounted on a linear and vertical stage in order to regulate the translation of the beam. A folding mirror reflects the beam towards the KM; the mirror is equipped with tip-tilt capabilities to adjust the angle between the laser beam and the mechanical axis of rotation of the bearing. To materialize the mechanical rotation axis of the KM we need to adjust the laser beam:

- translation in the x-y plane (laser stage)
- rotation around x and y (tip-tilt mount of the mirror)

No neutral density filters are placed between the source and the rest of the opto-mechanics in order to avoid refraction. Anyway a filter can be used in front of

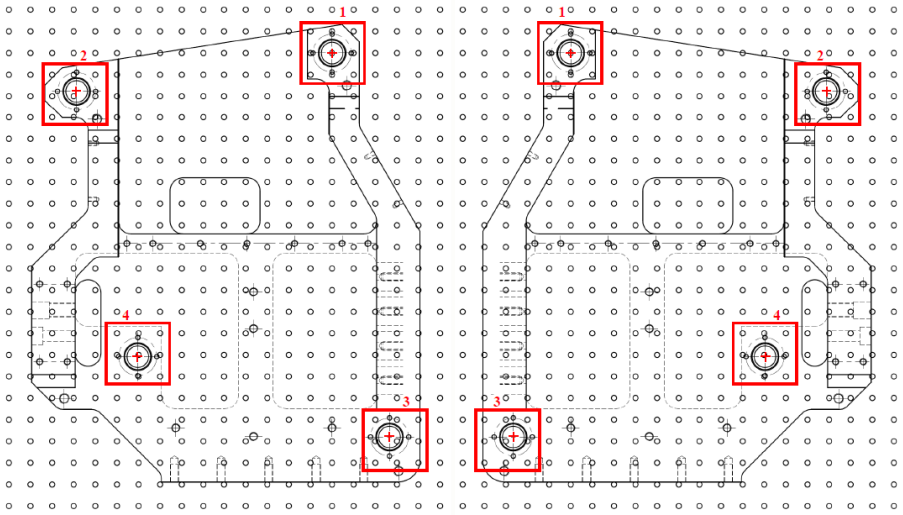

Figure 2.20: *Drawing of a standard optical bench, showing the places where interface plates should be put for KM SX on the left and for KM DX on the right.*

Figure 2.21: *An image of the KM.*

the detector. A reference flat mirror (dia=1inch), with tip-tilt capabilities, is fixed to the rotating bearing of the KM through a dedicated crescent flange and a magnetic repositionable plate. The same mount is used to hold the CCD camera in the following part of the procedure. The light reflected by the flat mirror comes back to the beam splitter and is reflected towards a 1inch plano-convex lens (focal length 750 mm) and a CCD (pixelsize=5.2μm), placed in the focal plane of the lens. The lens and the CCD are mounted on x/y stages.

Alignment of the Mirrors

The beam passing through the bearing is reflected by M1, M2, M3. All mirrors are equipped with tip-tilt mounts for the tip-tilt adjustment. M2 must use also its three screws to adjust his vertical position which is an important requirement for the optical path inside the KM. The setup prepared on the bench-side 2 is used to check the direction of the beam coming out from the KM. This bench-side can assume two possible configurations. In the first configuration the CCD camera is placed close to M3 and measures the decenter of the exit beam due to a tiptilt misalignment of M1. In the second configuration the lens and the CCD camera are used to measure the tip-tilt of the exit beam.

2.3.2 Alignment Procedure Concept

The goal of the alignment procedure is to properly orient mirrors M1 and M3 so that a laser beam materializing the axis of rotation is transmitted through the KM with decentering and tilt complying with the specifications. To achieve this it's necessary to align the laser to the axis of rotation and then align the KM to the laser beam. Furthermore, the alignment consists of correcting both tilt and decentering for either the laser and the KM. The optical properties of the KM can be used to distinguish between the off-set and tilt of the laser (with respect to the axis of rotation) and the misalignment of the KM itself. A lens placed after the KM can be used to separate the alignment on tilt from the alignment on decentering. When an off-set and/or tilted beam is transmitted through a perfectly aligned KM, a 180 degrees rotation of the KM generates a 360 degrees rotation of a transmitted beam. When a beam coincident with the axis of rotation is transmitted through a misaligned KM, a 180 degrees rotation of the KM generates a 180 degrees rotation of the transmitted beam. In practice, both errors will contemporary define the trajectory of a spot, reimaged on a CCD test camera, and an iterative procedure must be used to align the system. The resulting trajectory will be a spiral: the larger the distance between the starting point and the ending point of the spiral, the larger will be the KM misalignment. In the very beginning of the procedure, when the KM and the laser are severely affected by misalignments, it is better to project the laser spot on a screen placed few meters away from the KM. The same corrections based on the properties of the trajectory will then be then performed using a CCD camera for smaller misalignments.

Materialization of the rotating axis of the bearing

To materialize the mechanical rotation axis of the K-mirror a flat mirror is implemented as a reference inside the k-mirror with tip-tilt regulations. The laser station is equipped with a micrometric regulation for decenter corrections along XY axis. A beam expander and a variable diaphragm allow, respectively, to adjust collimation and to select a small central portion of the beam to minimize aberrations. The tip-tilt of the laser beam entering the bearing and

reflected by the reference mirror is regulated by the first folding mirror of the setup. The beam splitter reflects the beam coming from the reference inside the bearing into the lens direction. The lens focuses the beam, which is then reflected by another folding mirror into the CCD camera, to measure the beam angle and to adjust the reference mirror axis in order to make it parallel to the mechanical axis of rotation of the bearing. To perform the reference mirror tip-tilt regulation, the bearing is rotated of 180 degrees and the movement of the reflected spot on a screen is recorded. The inclination of the reference is adjusted in order to make the spot not move during an entire rotation of the bearing. At the very beginning of the procedure, the tip-tilt regulation is implemented by observing the spot movement on a screen placed between the reference and the beam splitter. A second regulation is done with the screen close to the camera position. Once the spot hits the camera, the tip-tilt of the reference mirror is adjusted looking at the spot position on the CCD, where the accuracy of the alignment is measured thanks to an IDL software showing the spot movement in real-time using the pixel scale units of the CCD.

Laser alignment

Next step is to reach a parallelism between the mechanical rotation axis of the bearing and the laser beam. A corner cube (retro-reflector) is positioned on the bench 1 setup, to compare the angle of the beam coming from the reference and the one directly coming from the laser (retro-reflected by the corner cube). The tip-tilt of the laser is regulated adjusting the first setup folding mirror tip-tilt. The position of the spot back-reflected by the corner cube is first recorded thanks to the CCD test camera and then compared with the position of the spot reflected by the reference. The tiptilt of the first flat setup mirror is adjusted looking at these two spots until their positions are coincident.

Center the laser beam on the mechanical axis

To adjust the decenter of the laser beam with respect to the mechanical rotation axis of the bearing the reference flat mirror is removed and replaced by a test camera. Two micrometric translating stages are used to adjust the laser beam, in a way it stay fixed on a position of the CCD camera for an entire 180° rotation of the bearing. At the beginning of the procedure the spot produces a half circle on the CCD, then the laser is shifted towards the mechanical axis of the bearing reaching an accuracy of about 10 microns.

2.3.3 Alignment of the K-mirror Mirrors

An iterative procedure is used to align M1 and M3. The first step is to align M1 observing the decenter of the beam, passed through the K-mirror, with respect to the beam entering the K-mirror itself. To do that, a CCD is placed on bench-side 2 very close to M3 and the bearing is rotated. If M1 is aligned, the beam reflected by M2 reaches the surface of M3 in the point defined by the intersection of the mirror surface and the rotation axis. A misalignment of M1 lead the spot above or below this point. The spot produces a spiral or a semi-circle on the CCD where the radius must be minimized using the tip-tilt correction of M1. The second step is to align M3 observing the tip-tilt of the beam outcoming from the K-mirror, positioning the CCD on the focal plane of a lens. In this phase, M3 tip-tilt is adjusted minimized again the radius of the spiral or the semi-circle drawn by the spot in a 180 degrees rotation of the

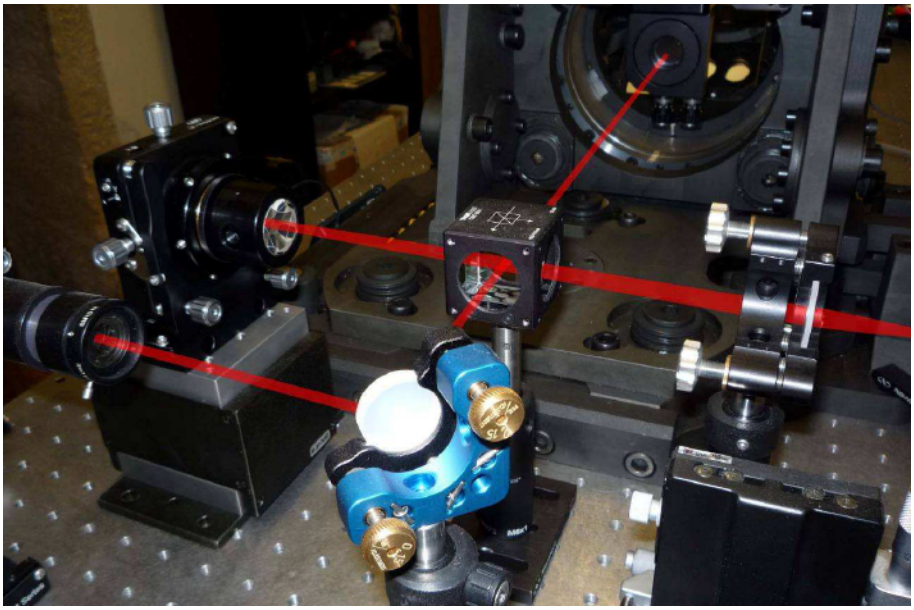

Figure 2.22: *the corner cube placed in the laser beam to reflect back the laser with the same direction. The position on the CCD is compared with the position given by the window. The middle point on the CCD represent the zero position angle of the beam in respect to the rotation axis. That test describe how to correct the tip-tilt of the folding mirror to make the laser parallel to the mechanical rotation axis..*

bearing on the CCD. If the spiral or the semi-circle become a circle instead of a point it probably means that will need a residual correction of the tip-tilt of the laser (using the first setup folding mirror on bench-side 1).

M1 and M3 are moved iteratively, accordingly with the already described observable. When, after a complete 180° rotation, the path drawn by the transmitted beam on the setup CCD (in both configurations) becomes a circle, the mirrors are aligned, because the KM is de-rotating the incoming beam. At this point, the incoming laser beam can be tilted or shifted laterally, of an amount lower than the indetermination in materializing the bearing rotation axis. When the circles diameters on the CCDs are minimized, the incoming laser is placed on the real rotation axis of the system.

2.3.4 Alignment of M2 (Additional Optical Path Analysis)

The optical path inside the K-mirror, between the mirror M1 and M3 has to be 640 1mm. A distantiometer (accuracy of 1mm) is placed on bench-side 2 in the optical beam and adjusted in decenter and tip-tilt. Its beam has the opposite versus of propagation with respect to the laser beam used for the alignment. A reference screen is placed on bench-side 1. To roughly adjust the tip-tilt of the distantiometer, the beam is sent back inside the laser head. Tests on the distantiometer show that a statistic measure of the distance can give the required accuracy. The distantiometer is moved integrally with the reference screen, to measure their relative distance with and without the KM in between, in order to retrieve the additional optical path introduced by the KM itself. The

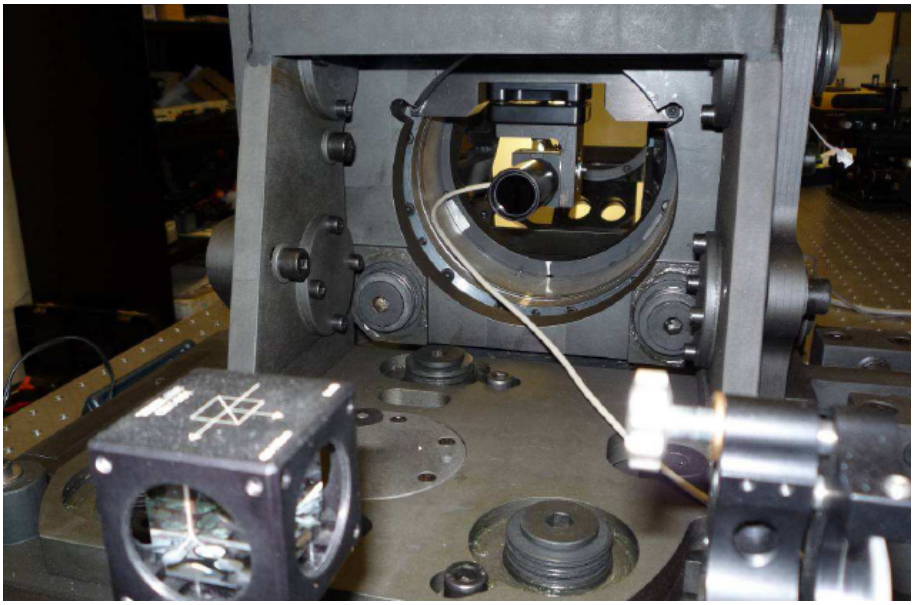

Figure 2.23: *the CCD camera placed on the rotation axis. The rotation of the KM and of the CCD consequently produce a semi-circle on the camera. Adjust the x-y linear stages below the laser to correct the decenter. In this test the laser will overlap the rotation axis. During an entire rotation of the bearing the spot didn't move more than 2 pixels of the test camera, that is to say 10μm in both KMs.*

alignment of the laser pointer of the distantiometer to the mechanical axis can reach an accuracy of about 200arcsec which is enough for the target because any optical misalignment increases the optical path only of a few microns.The internal optical path distance is adjusted with a piston movement of M2 inside the K-mirror, which can be done adjusting its three tilting systems at the same time. Of course, the M1+M3 and the M2 alignments have to be repeated iteratively, to achieve the best configuration.

2.3.5 KM Alignment on the LN Optical Bench

Once the KM is internally aligned, it can be placed on the optical path of the camera FP20 and aligned with respect to the optical axis. In the description below we assume the following coordinate system: z is coincident with the rotation axis of the KM, y is perpendicular to the optical bench, the origin is located at the aperture of the laser source used for the alignment. In the following procedure the KM is aligned with respect to a given beam, materializing the optical axis. The concept to be used for the KM alignment to a given optical axis is the same used to materialize the bearing rotation axis during the KM internal alignment, but in this case the proper KM actuators for external alignment (implemented on the base plate) are used. In the figure is shown the setup used for the KM alignment on LN optical bench. First of all, a flat mirror is implemented as a reference inside the k-mirror with tip-tilt regulations. A beam splitter reflects the beam coming from the reference inside the bearing towards a lens. The lens focuses the beam, which is then reflected by a folding mirror into a CCD test camera, to measure the beam angle and to adjust the reference mirror in order to make it orthogonal to the mechanical axis of rotation

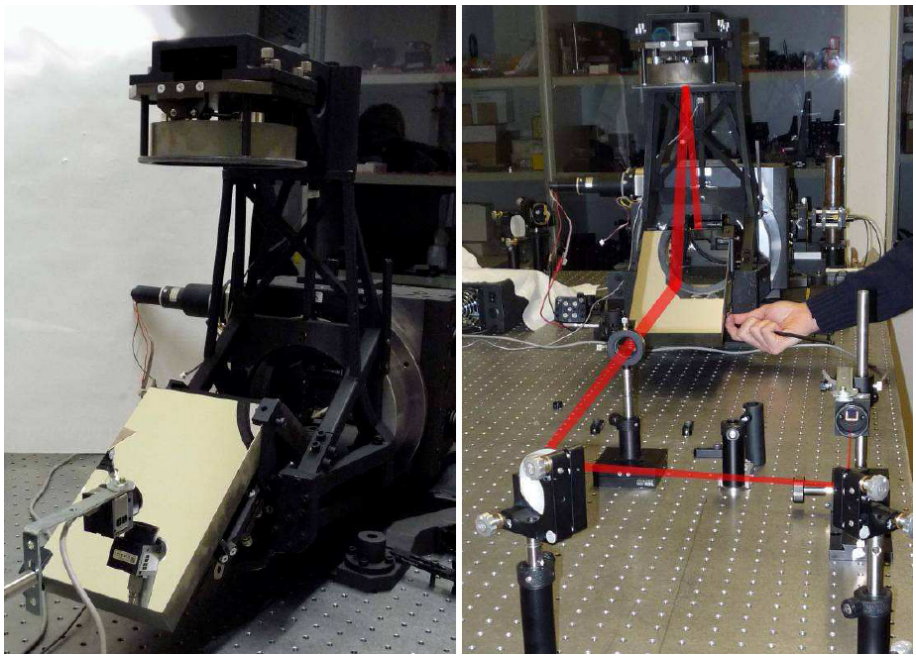

Figure 2.24: *decenter regulation is given by a tip-tilt regulation of M1. The exit beam must hit the intersection point between the surface of M3 and the rotation axis. If the CCD is placed very close to M3, its inclination become negligible. Alignment of M3 is done by using a lens and a CCD. The spot produces at first a semicircle, or a spiral and finally a "point" or a circle. The spot must be placed in the middle point computed between the first and the last position obtained on the CCD, corresponding to rotation of the KM of 0° and 180°.*

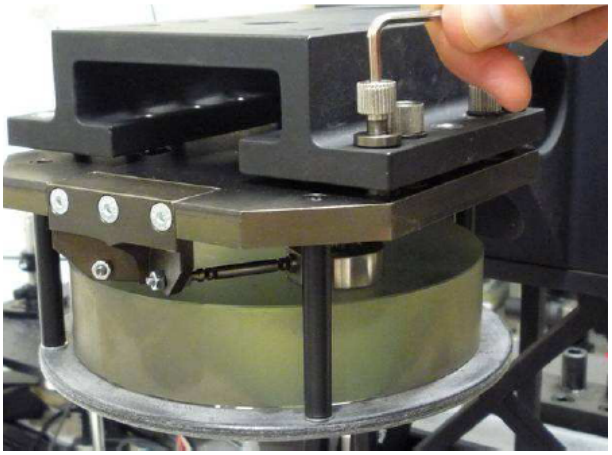

Figure 2.25: *measurement of the optical path inside the KM. The distantiometer is aligned with the optical axis of the KM using decenter and tip-tilt correction on the distantiometer holder. Is reached an accuracy of about 200" for tiptilt and 0.5mm for decenter. The vertical position of M2 can be adjusted using the 3 screws over the mirror mount of M2.*

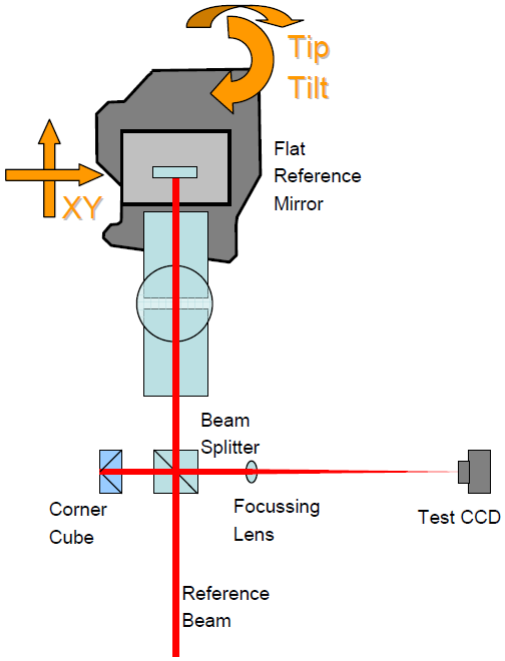

Figure 2.26: *Setup used to align the KM to a given optical axis, materialized with a reference beam.*

of the bearing. To perform the reference mirror tip-tilt regulation, the bearing is rotated of the maximum allowed amount (which is 180° for the first KM positioned on the LN bench, and 120° for the second one) and the movement of the reflected spot on a screen is recorded. The inclination of the reference is adjusted in order to make the spot not move during an entire rotation of the bearing.

At the very beginning of the procedure, the tip-tilt regulation is implemented by observing the spot movement on a screen placed between the reference and the beam splitter. A second regulation is done with the screen close to the camera position. Once the spot hits the camera, the tip-tilt of the reference mirror is adjusted looking at the spot position on the CCD, where the accuracy of the alignment can be measured thanks to a software showing the spot movement in real-time using the pixel scale units of the CCD. Next step is to reach a parallelism between the mechanical rotation axis of the bearing and the laser beam. A corner cube (retro-reflector) is positioned on the bench setup, to compare the angle of the beam coming from the reference mirror and the one materializing the optical axis (retro-reflected by the corner cube). The position of the spot back-reflected by the corner cube is compared with the position of the spot reflected by the reference mirror. The tiptilt of the KM base plate is adjusted looking at these two spots until their positions are coincident. To adjust the decenter of the KM with respect to the reference beam, the reference flat mirror is removed and replaced by a test camera. The KM base plate lateral and vertical adjustment screws are used to adjust the KM position, in a way the reference beam is fixed on a position of the CCD camera for the allowed rotation of the bearing.

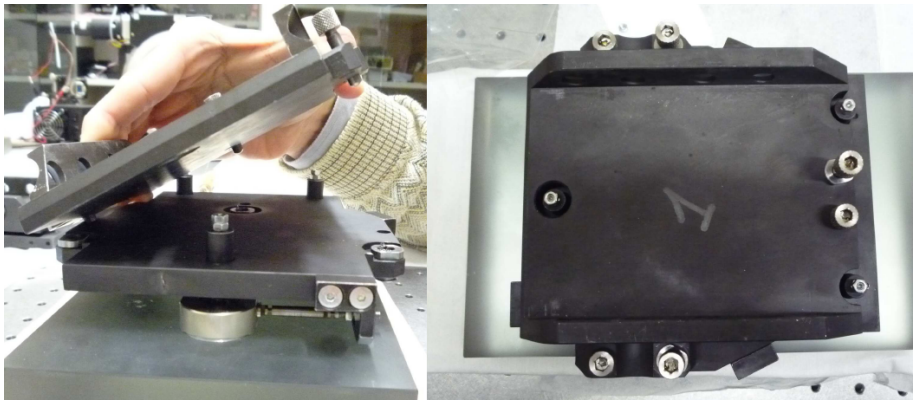

Figure 2.27: *Actuators below the mount of the mirrors M1 and M3..*

2.3.6 Actuators for Internal Alignments

The units M1 and M3 have actuators to adjust the mirror orientation. They are very similar, so the description for just one unit will be given. There are three couples of screws placed at 120° to rotate the mirror around one direction with a large angle use one screw and unlock the opposite screws; to reverse the motion do the opposite using two screws to push the mirror mount and unlocking the other screw. For fine adjustments lock every screw forcing the motion against their threading. The pushing screws enter into a threaded bushing fixed to the plate which is rigidly connected to the K-Mirror frame (bottom plate); the screw head arrives onto the plate which is connected to the mirror (mirror plate) and on this place a countersink hole is made allowing some play between the screw head and the housing. The pulling screws enter into passing holes made on the bottom plate and are screwed to another set of threaded bushing which are now fixed to the mirror plate. The play between every mechanical part ensures the possibility to adjust the mirror orientation, while the mirror mount deformation prevent damages and deformation of the mirror. It is recommended to make adjustments along one direction as far as practicable, as the unidirectional repeatability is very good. In case of reversal motion the hysteresis of the actuators and the elasticity of the mount could give the wrong sensation that the actuation has no effect on the base-plate position. Continue adjusting along the same direction until the hysteresis is recovered. M2 unit exploits the same concept of push-pull screws, which allows the translation of the mirror along the direction orthogonal to its reflecting surface and allows also angular adjustment in case is needed.

2.3.7 Actuators for Alignment to a Given Optical Axis

The actuators for the alignment to an external optical axis (the FP20 camera) are placed on the base-plate of the KM (see figure 2.28). Z is along the optical axis and doesn't need of adjustment system, Y is along the vertical direction. To perform the adjustment is useful to: unlock the screws a bit; make the necessary adjustments by unscrewing one of the two actuators and by screwing the opposite one; lock the screws; put the actuator which has been unscrewed in contact with the mounting base. The system regulation repeatability suffers of mechanical hysteresis and it is then suggested to perform unidirectional adjustments as far as possible to minimize this effect. The available degrees of

freedom of the baseplate are:

1. pitch - in figure 3 (red) and figure 4 (red) are shown the adjustment and the locking screws respectively.

   Travel range: ±1.35degree

   Resolution: 10”

2. roll - in figure 3 (blue) and figure 1 (black) are shown the adjustment and the locking screws respectively.

   Travel range: ±2.3degree

   Resolution: 10”

3. X linear displacement - in figure 2 (red) and figure 1 (white) are shown the adjustment and locking screws respectively.

   Travel range: ±5mm

   Resolution: 10μm

4. Y linear displacement - in figure 5 and figure 6 are shown the adjustment and locking screws respectively.

   Travel range: ±5mm

   Resolution: 10μm

Pitch and roll are a bit coupled and it is recommended not to fully unscrew the locking screws: keep them always tighten to obtain the best sensitivity and to decouple the actuators. Furthermore, the rotational degrees of freedom are disentangled from the translational ones. It is recommended to make adjustments along one direction as far as practicable, as the unidirectional repeatability is very good. In case of motion reversal the hysteresis of the actuators and the elasticity of the mount could give the wrong sensation that the actuation has no effect on the base-plate position. Continue adjusting along the same direction until the hysteresis is recovered.

2.3.8 Electrical Interface

Figure 2.29 show some pictures of the KM patch box. The colored flat cable connects the motor encoder with the electric board provided by MPIA, while the black cables connect the limit switches (the connectors have different number of pins, 4 and 5 respectively, to avoid any connection mistake) and the motor (3 pins).

2.4 Verification

In this document the results of the mechanical and optical tests done on the components of the derotator. Here are described the alignment procedure verification tests for both units KM1 and KM2. The assembly, integration and verification of both the K-Mirrors was finished in April 2011. The systems were integrated and aligned in the optical laboratory of the Astronomical Observatory of Padova. The K-mirror Unit 1 and Unit 2 have been assembled, aligned and tested in the optical laboratory of the Astronomical Observatory of Padova, and they will be integrated on the Linc-Nirvana optical bench, with the aim of de-rotating the 2’ field of view which can be used by the corresponding Mid-High Wavefront Sensor. Both units now are at the MPIA in Heidelberg. A technical

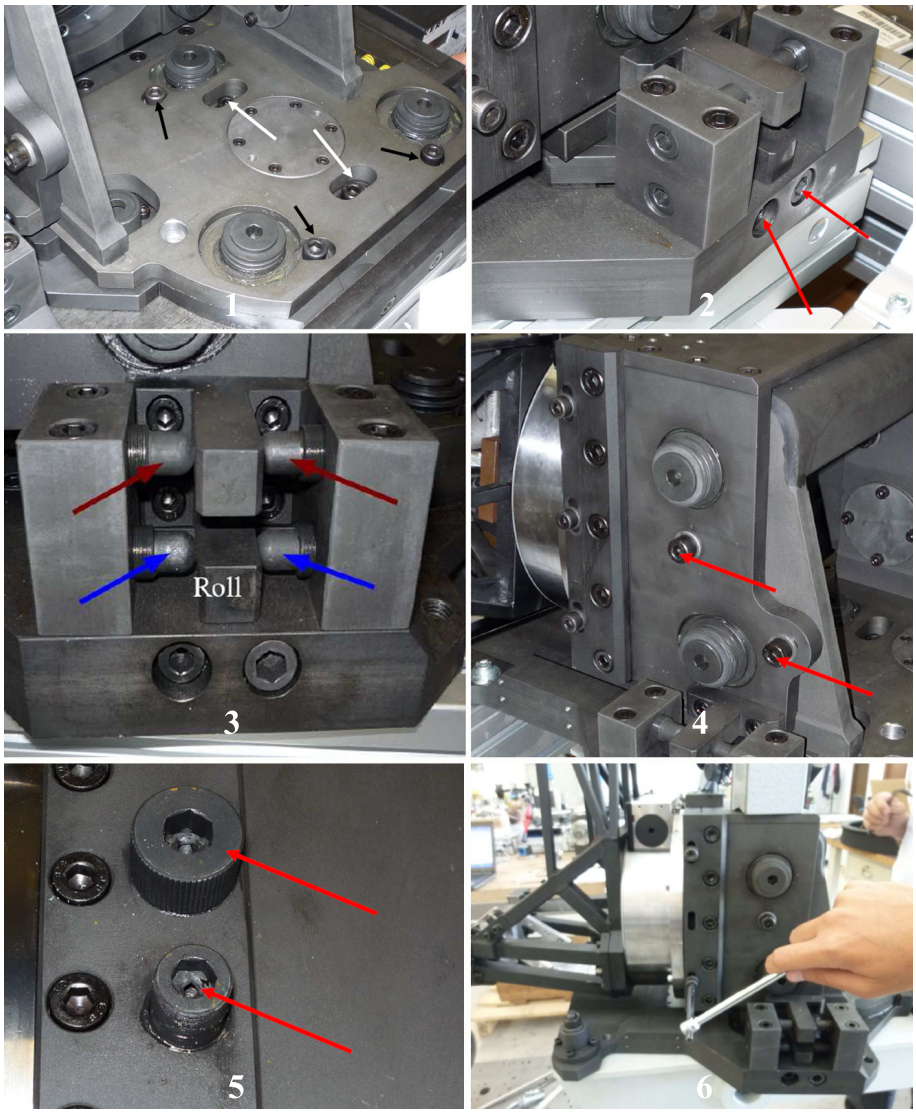

Figure 2.28: *The actuator of figure 2 are for the decentering in the X direction and the locking screws are shown in figure 1 in white. The actuators for pitch and yaw alignment are in figure 3 and the pitch and roll locking screws are in figure 1 and 4 in black and red respectively. Pitch adjustment is achieved by screwing one of the related actuators, depending on the adjustment direction. Figure 4 in red shows the locking screws of the pitch actuators while in figure 1 in black are shown the roll actuators. Figure 5 shows actuators for the vertical adjustment while figure 6 shows the locking screws.*

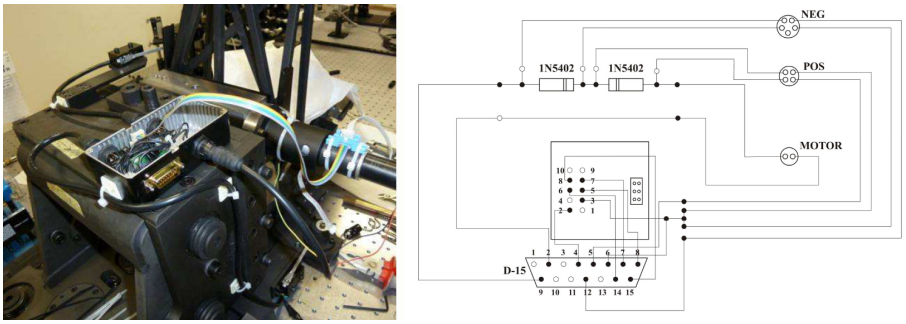

Figure 2.29: *The KM patch box connected to the motor of the rotating bearing and the limit switches.*

support from Padua as been given ton MPIA several time to perform flexure test and the cheque of the performance after the shipment. After the integration on the MPIA laboratory the thermal test will be done in the climatic chamber of the institute to verify the alignment maintenance in a temperature range from 20° to -20°C. Each system is composed by 3 flat mirrors, with tip-tilt capabilities, fixed on a common frame, which is able to perform a 180 degrees of rotation, thanks to a rotating stage, corresponding to a 360 degrees rotation on the sky. However, this rotation range has been reduced to 90 degrees to avoid collisions with the other K-mirror. Furthermore, during observing operations, the system will be asked to perform a rotation only on a ±15 degrees range, corresponding to a ±30 degrees rotation of the FoV. The verification test concerns this topics:

- SHIFT AND TIP-TILT ADJUSTMENT RESOLUTIONS TEST:
- BASE-PLATE FLEXURES TEST
- MIRRORS FLATNESS TEST
- INTERNAL ALIGNMENT TEST

Laboratory equipment for the performance verification test :

- generic lab tools (screwdrivers, hex keys...)
- needed a spirit level
- needed 2 dial gauges
- needed an interferometer
- A laser source (λ=632.8μm) equipped with x-y movements
- beam expander (dia.=1")
- variable diaphragm (0.5mm-2mm)
- folding mirrors on tip-tilt mounts
- flat mirror (dia=1")
- beam splitter (50:50)
- lens (f =750mm, dia=1") with tip-tilt-x-y movements
- CCD detector (pixelsize=5.2μm) with x-y movements

#	Requirement	
1	Deflection of the chief ray[2]	40 arcsec
2	Decentering of the chief ray[2]	100 µm
3	M1 Flatness[3]	λ/35 nm RMS @ 800nm
4	M2 Flatness[3]	λ/60 nm RMS @ 800nm
5	M3 Flatness[3]	λ/35 nm RMS @ 800nm
6	Mirrors Reflectivity	> 96%
7	Maximum derotation angular velocity	2.0 deg/s
8	Maximum derotation angular acceleration	0.35 deg/s2
9	Bearing motor power consumption[4]	< 2W
10	Bearing minimum incremental motion	0.008 deg
11	Strehl Ratio[3]	SR > 95% @ 1µm
12	Additional optical path	421±1 mm
13	Lateral and Vertical Adjustment Travel[5]	±5mm
14	Lateral and Vertical Adjustment Resolution[5]	10 µm
15	Tip-tilt Adjustment Travel[5]	±0.5deg
16	Tip-tilt Adjustment Resolution[5]	10" (goal 5")

Figure 2.30: [1] *Verification Method: D=review of design, T=test, A=analysis, I=inspection, S=by similarity.* [2] *These are to be intended as the maximum (Peak to Valley) deflection and decentering through a contiguous span of ±30deg in the pupil plane, corresponding to ±15 deg of rotation of the physical frame of the K-mirror.* [3] *While the mirror flatness is estimated from the measurement taken over the optically clear area, the Strehl is estimated at the wavelength of one micron and using only the portion of the mirror surface interested by the footprint of a single beam.* [4] *This number is due to the maximum heat dissipation accepted from the motor, to avoid the turbulence formation just before the MHWS.* [5] *Travel adjustments are given for the unit as a whole.*

- Tip-tilt mount to hold a 1" mirror integral with the rotating bearing
- 1 corner cube (dia=1")
- Generic holders and bases

2.4.1 Mirrors Reflectivity

Mirrors coating reflectivity is guaranteed by the mirrors manufacturer as above 98% in all the required range. A reflectivity curve of protected silver, provided by the company itself, is shown in figure 2.31. The requirement is fulfilled.

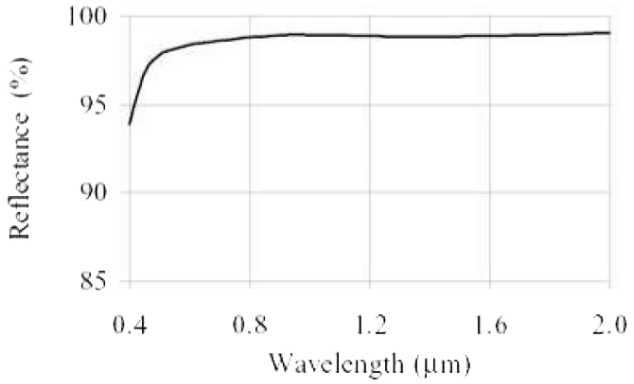

Figure 2.31: *Protected silver coating reflectivity.*

2.4.2 Bearing Motor Power Consumption

The selected motor dissipated power is 1.16W. The requirement is fulfilled. Further test can be performed only with the final KMs electronics.

2.4.3 Bearing Minimum Incremental Motion

The selected motor minimum measurable step motion is 0.0036°. The requirement is fulfilled. Further test can be performed only with the final KMs electronics.

2.4.4 Shift and Tip-Tilt Adjustment Resolution Test

The repeatability of the shift movements of the entire K-mirror on a bench has been individually tested at the Tomelleri company place, by Tomelleri, Spacelight and Padova teams. The vertical repeatability has been measured taking the central travel position as a reference, shifting several times the system of a known amount in one direction and measuring the true shift with a mechanical comparator, to compare the reached positions. These measurements have been taken in both directions, to check the bidirectional repeatability too. An analogous procedure has been used to measure the lateral adjustment repeatability. The repeatability has been measured taking the central travel position as a reference, tilting several times the system of a known amount in one direction and measuring the true tilt with at least two dial gauges, to compare the reached positions. These measurements have been taken in both directions,

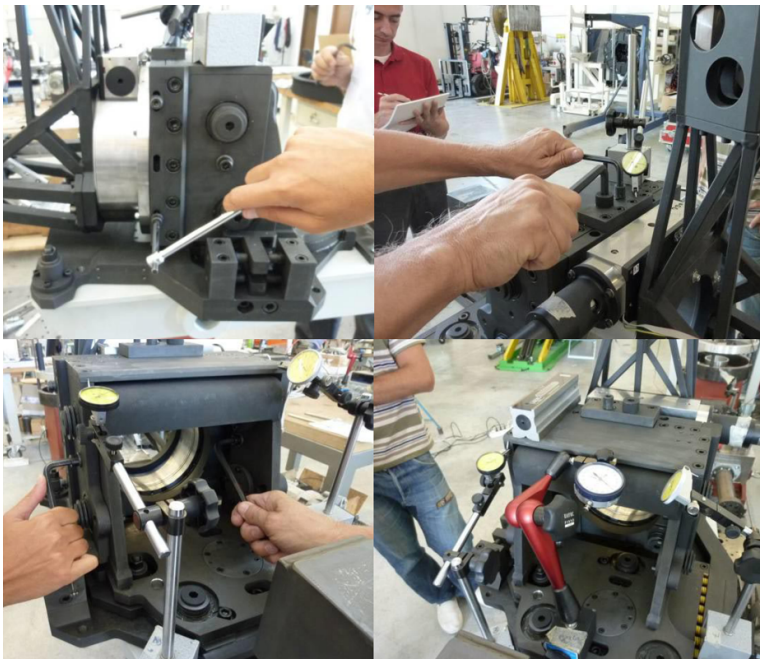

Figure 2.32: *Vertical adjustment of the k-mirror as a whole. On the left, the two screws used to fix the vertical position are unscrewed to allow the vertical adjustment test. On the right, two screws placed on the upper part of the k-mirror are used for the vertical regulation, with push and pull functions respectively.On the left, the system is tilted using two dedicated screws. On the right, three mechanical comparators are used to measure the combination of tip and tilt of the system.Mechanical comparators used to measure the horizontal tilt directly on the base of the k-mirror*

to check the bidirectional repeatability too. It has been found out in both cases that it would be required to proceed on the same direction for the tuning. In such a case, the requirement is fulfilled and referring to figure 2.28 the results are:

1. pitch - in figure 3 (red) and figure 4 (red).

   Travel range: ±1.35degree

   Resolution: 10”

   The unidirectional repeatability: 4”

2. roll - in figure 3 (blue) and figure 1 (black).

   Travel range: ±2.3degree

   Resolution: 10”

   The unidirectional repeatability: 3”

3. X linear displacement - in figure 2 (red) and figure 1 (white).

   Travel range: ±5mm

   Resolution: 10μm

   The unidirectional repeatability: 2 microns

   Bidirectional repeatability: 16 microns

4. Y linear displacement - in figure 5 and figure 6.

   Travel range: ±5mm

   Resolution: 10μm

   The unidirectional repeatability: 2 microns

   Bidirectional repeatability: 20 microns

2.4.5 Base-Plate Flexure Test

A complete, optical test of the KM behavior for different inclination angles of LN bench could not be performed with our facilities, being the tilting bench too small to include an optical setup on it; so this topic needs further investigations, to be performed at MPIA. A quick check of the behavior of the KM beam in a tilted configuration, has been carried out at the Tomelleri company place, by Tomelleri, Spacelight and Padova teams. The KM mechanical structure (with only M2 mounted on it) was tilted of 60^o in the direction shown in Figure 17 and the resulting shift of the structure in the tested point was 46 μm. Flexures will be combined with the thermal effects and internal KM misalignments, to verify their compliance with requirements.

Figure 2.33: *Left: a tilting bench is used to change the inclination of the system, while the flexures are measured using a mechanical comparator. Right: flexure test at the Max Plank Institute for Astronomy in Heidelberg after the internal alignment technical support. The KM SX was placed on the linc-NIRVANA bench that will be at the LBT telescope in the next future.*

In Heidelberg has been performed a second flexures test on the complete and aligned KM. The tests was performed on the real linc-NIRVANA carbon bench that can tilt from 0deg to 60deg. After calibration of the autocollimator setup, K-Mirror SX and DX was inserted into the optical path. It was aligned to a reasonable low absolute tilt on the auto-collimation telescope (error angle less than 150") Then, the bench has been tilted continuously to 70 degrees. The tilt angles where recorded by the autocollimator and saved by the INCOLINK software. The tests have been carried out in 2 different configurations:

1. KM at 90 degrees: In this position, the tilt signal due to flexure is dominated by the y-component (up-down direction with respect to the bench surface). The contribution of tilt in x direction (left-right) is small.

2. KM at 45 degrees: With the K-Mirror rotated to a 45 degree position, the tilt sensitivity is almost equal for x and y direction.

For each configuration we used two different measurement procedures. The bench was tilted continuously or by steps of 10 degrees. In the following plots the results of our measurements are displayed. The magenta curves show the combined tilt of both (x and y) directions. In conclusion, the total chief ray tilt angle due to K-Mirror flexure is:

- KM at 90 deg: 22.5 arcseconds
- KM at 45 deg: 17 arcseconds

The maximum of the tilt occurs at an bench inclination of around 45 degrees. In the figure **??** is shown the flexure of the baseplate of the KM SX. In the first figure is described a single elevation of the bench (up and down) with the KM rotated of an angle of 90°. In the second figure are described three elevation of the bench (up and down) with the KM rotated of the same angle of 90°. In the third figure is described a single elevation of the bench (up and down) with the KM rotated of an angle of 45° as visualized in the second of figure 2.33. In the last figure is described the flexures during three elevations of the bench (up and down) with the KM rotated of an angle of 45°.

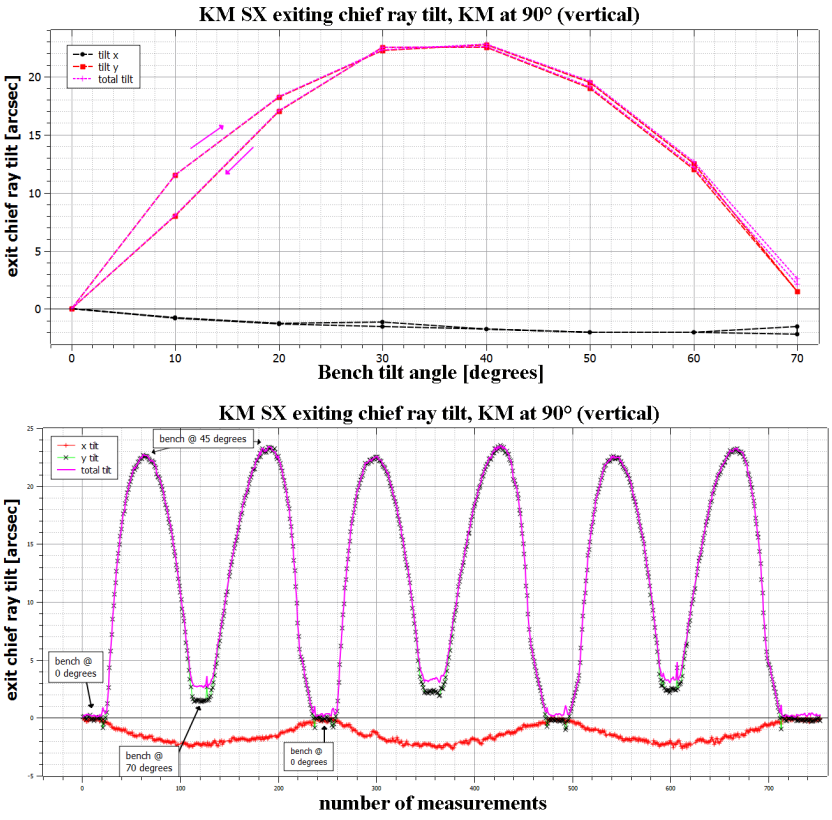

Figure 2.34: *Two images to describe the flexure measurement of the baseplate of the KM SX roteted of an angle of 90degrees. The "sinusoidal" shape describe the elevation of the NIRVANA bench performed three times.Here the setup allows to measure tip and not the tilt because of the inclination angle of the frame(90deg) that make one measurement insensitive.*

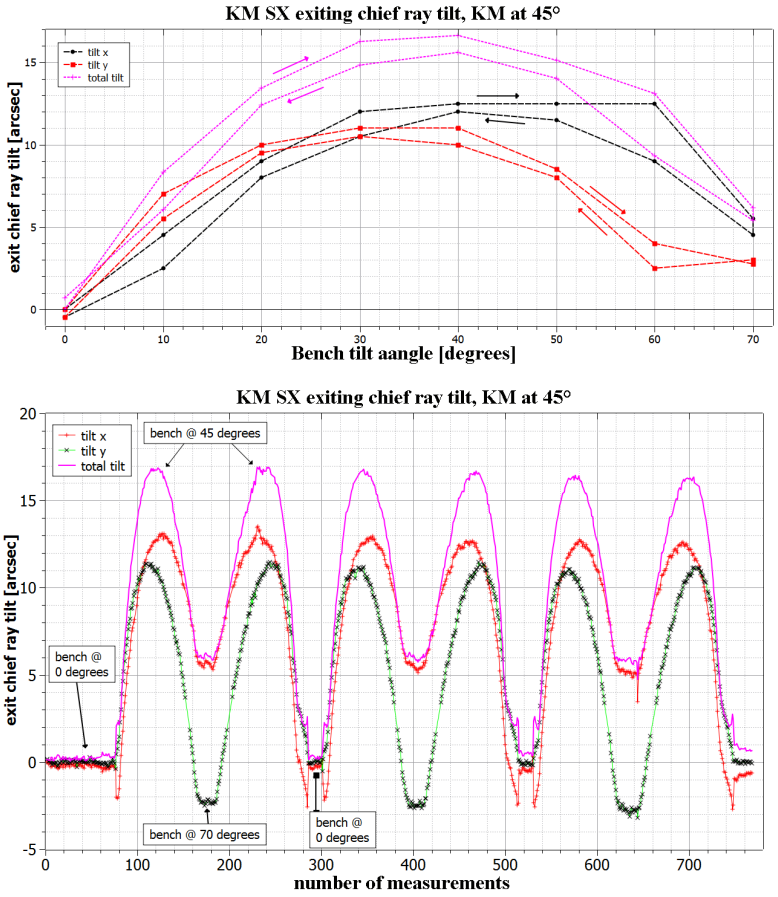

Figure 2.35: *Two images to describe the flexure measurement of the baseplate of the KM SX rotated of 45degrees. The "sinusoidal" shape describe the elevation of the NIRVANA bench performed three times. In this case both tip and tilt are sensitive*

2.4.6 Mirrors Flatness Test

The mirror flatness measurements have been performed by the manufacturer, they are summarized in figure 2.36. The mirror flatness in the central part of each mirror has been re-checked also using an interferometer (reference wavelength = 633nm, beam diameter = 100mm) in the Observatory of Padova. Of course, a smaller aperture probably means a smaller flatness PtV value, so these measurements are just a check. The results, summarized in figure 2.36 and obtained by the manufacturer and in our test, are both inside specifications. The requirement is then fulfilled.

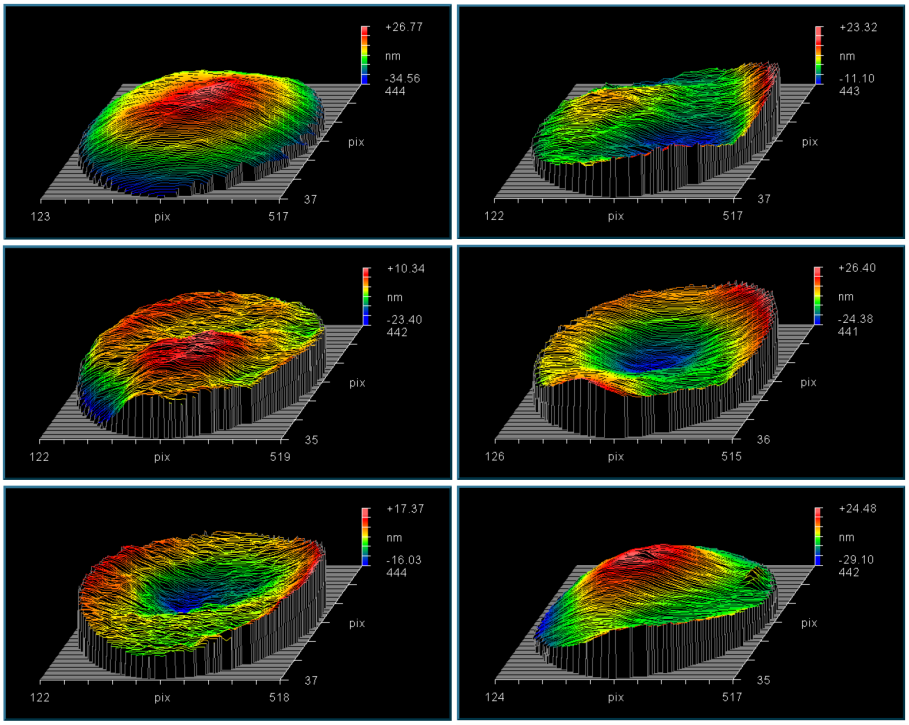

Mirror	Required RMS	Manufacturer RMS	Padova RMS
KM#1 M1	< λ/35 @ 800nm	λ/62 (λ not specified)	λ/56 @ 632.8nm
KM#1 M2	< λ/60 @ 800nm	λ/91 (λ not specified)	λ/163 @ 632.8nm
KM#1 M3	< λ/35 @ 800nm	λ/50 (λ not specified)	λ/102 @ 632.8nm
KM#2 M1	< λ/35 @ 800nm	λ/71 (λ not specified)	λ/123 @ 632.8nm
KM#2 M2	< λ/60 @ 800nm	λ/83 (λ not specified)	λ/70 @ 632.8nm
KM#2 M3	< λ/35 @ 800nm	λ/100 (λ not specified)	λ/61 @ 632.8nm

Figure 2.36: *Interferometric measurement performed in Padova, taken in a central portion with diameter = 100mm. The left column represents the KM SX with mirrors M1, M2 and M3. The right column is for for KM DX. Mirrors flatness interferometric RMS measurements results from the manufacturer compared with the values obtained obtained in the Adaptive Optics laboratory in Padova.*

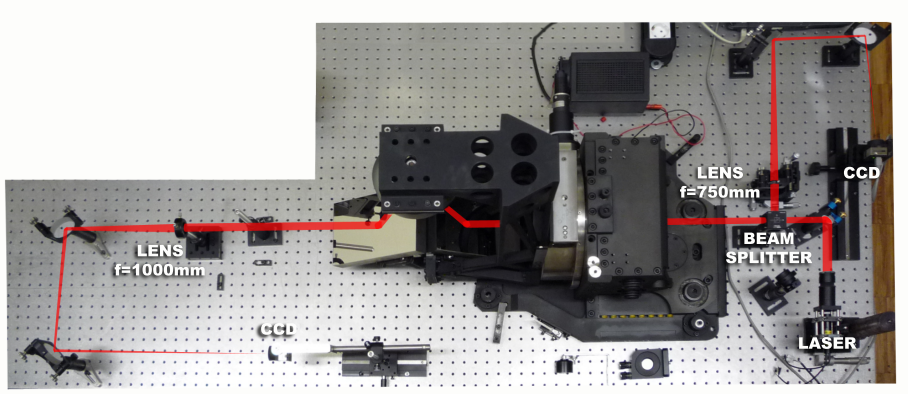

Figure 2.37: *Optical setup. The part on the right of the K-mirror is labeled "bench-side 1", used for the bearing rotation axis materialization. The part on the left of the K-mirror is labeled "bench-side 2", used to check the direction of the beam coming out from the KM.*

2.5 Internal Alignment Verification

In the following the result of the alignment procedure on the transmitted beam. The beginning of the procedure from item 1 to item 3 define the accuracy of the materialization of the bearing rotation axis while the following steps define the correct internal alignment of the derotator. The adjustment of the internal optical path is important because define the focal position of the FoV on the MHWS. The maximum deflection and decentering of the chief ray through a contiguous span of ±30deg in the pupil plane, corresponding to ±15 deg of rotation of the physical frame of the K-mirror, has been quantified using the setup for the M1 and M3 alignment.

K-MIRROR DX (UNIT 1) deflection and decentering of chief ray verification results

The data obtained with verifications of the out-coming beam deflection and decentering for position angle ranging from 0° to 90° (range in which KM unit 1 could work avoiding collisions with KM unit 2) are shown in Figure 18, resulting in a 31 arcsec and a 70μm ranges, respectively. However, deflection and decentering of the chief ray requirements, according to the requirements contained in AD4, are to be intended as the maximum (Peak to Valley) deflection and decentering through a contiguous span of ±30° in the pupil plane, corresponding to ±15° of rotation of the physical frame of the KM.

K-MIRROR SX (UNIT 2) deflection and decentering of chief ray verification results

The data obtained with verifications of the out-coming beam deflection and decentering for position angle ranging from 90° to 180° (range in which KM unit 2 could work avoiding collisions with KM unit 1) are shown in Figure 18, resulting in a 5 arcsec and a 80 μm ranges, respectively. The system is then fulfilling the requirements in all the possible working range. Moreover, deflection and decentering of the chief ray, according to the requirements, are

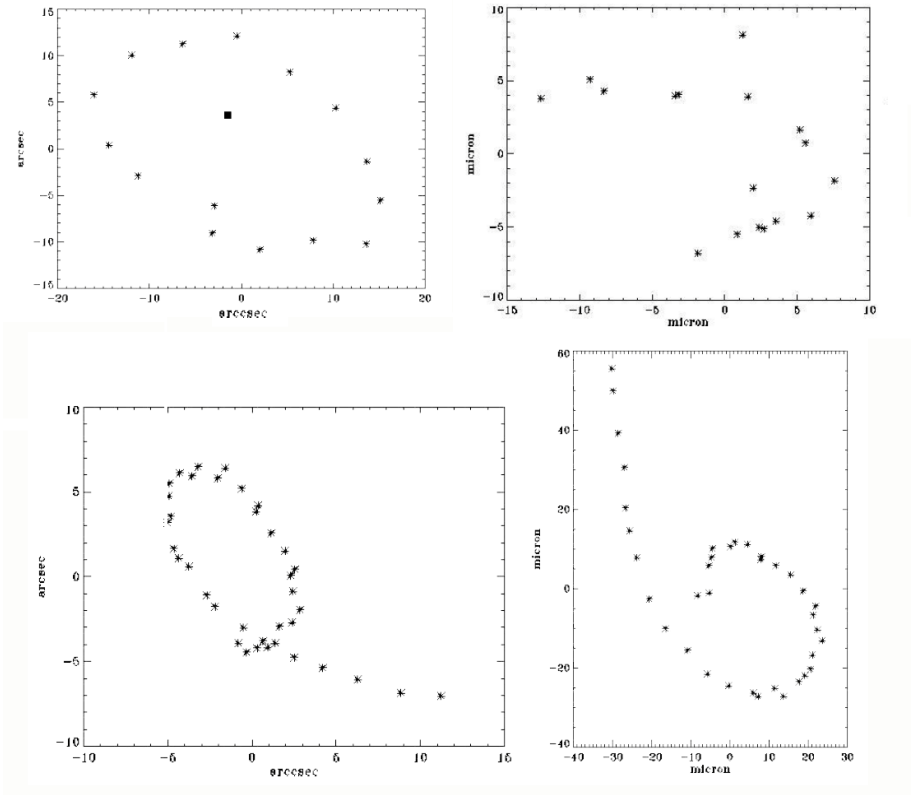

Figure 2.38: *Top images: graphics for KM1 with the accuracy obtained for the materialization of the axis in tip-tilt (left)and decentering (right).The stars represent the angle of the beam reflected by the reference mirror during a rotation of 180°. The squared dot is the beam reflected by the corner cube. Deflection and decentering of the beam out-coming from the K-mirror DX, for a position angle ranging from 0° to 90°.On the left, the tilt measurements are shown, resulting in a tilt range (for a 180° field rotation) of about 22 arcsec. On the right, the de-centering measurements show an overall range of 97μm.*

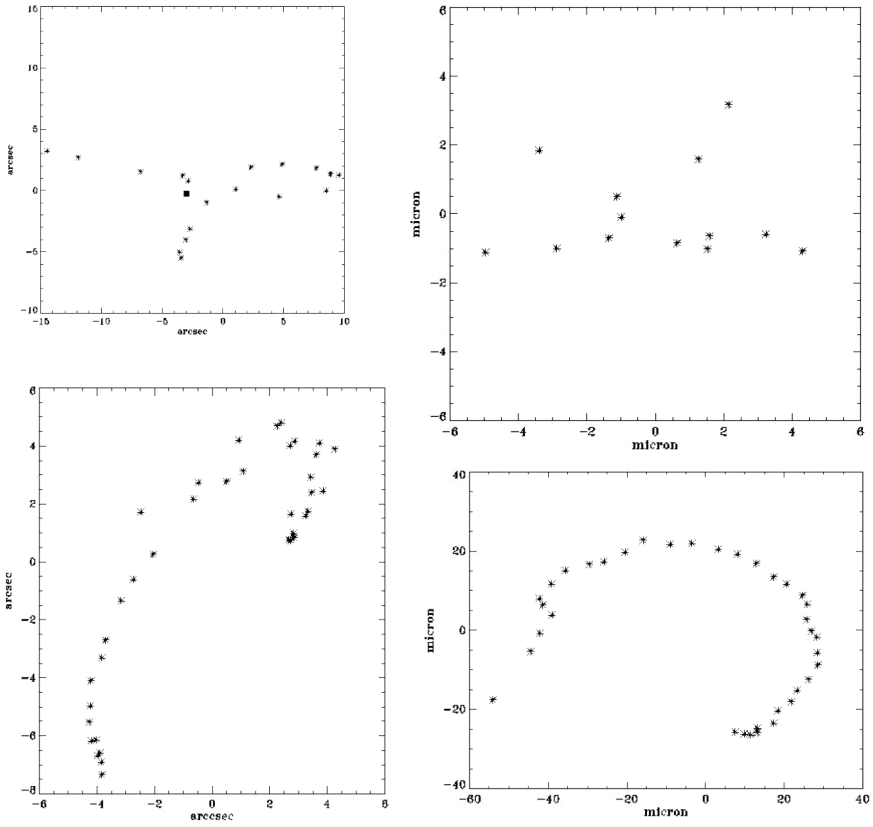

Figure 2.39: *Top images: graphics for KM1 with the accuracy obtained for the materialization of the axis in tip-tilt (left)and decentering (right).The stars represent the angle of the beam reflected by the reference mirror during a rotation of 180°. The squared dot is the beam reflected by the corner cube. Deflection and decentering of the beam outcoming from the K-mirror DX, for a position angle ranging from 0° to 90°. On the left, the tilt measurements are shown, resulting in a tilt range (for a 180° field rotation) of about 16 arcsec. On the right, the de-centering measurements show an overall range of about 94μm.*

to be intended as the maximum (Peak to Valley) deflection and decentering through a contiguous span of ±30° in the pupil plane, corresponding to ±15° of rotation of the physical frame of the KM.

1. Alignment of a reference setup mirror, making it orthogonal to the bearing rotation axis:
   - for KM1, the resulting tilt range is about 32 arcsec, corresponding to 32/2 16 arcsec of mirror wobble, mainly due to a bearing wobble.
   - for KM2, the resulting tilt range is about 25 arcsec, corresponding to 25/2 13 arcsec of mirror wobble, again mainly due to a bearing wobble.
2. Laser beam alignment, to reach a parallelism between the mechanical rotation axis of the bearing and the laser beam, using a corner cube:
   - the non-parallel error angle produces a spot that hit the detector in the middle of the point distribution range defined by the performances of the bearing. This means that the accuracy is of about 5 arcsec.
3. Centering of the laser beam on the mechanical axis, the reference flat mirror is removed and replaced by a test camera:
   - the laser alignment reaches an accuracy of about 25μm for KM1.
   - the laser alignment reaches an accuracy of about 10μm for KM2.
4. Deflection and decentering of the chief ray regulated adjusting M1 and M3.
   - the deflection and decenterin alignment reaches respectively an accuracy of about 13arcsec and 92μm for KM1.
   - the deflection and decenterin alignment reaches respectively an accuracy of about 11arcsec and 62μm for KM2.

2.5.1 Optical Path

The internal optical path has been measured during the K-mirror alignment procedures, as described in Section Error! Reference source not found.Although the manufacturer declare a maximum error of ±3mm for measurements up to 12 m, we elected to perform an in house verification of the error just in the range where we are supposed to carry out our own measurement. The distantiometer was used to measure the distance from a screen positioned on a linear stage, equipped with a micrometric actuator. The stage was moved in a 1.5mm range and 10 measurements have been taken with the distantiometer for each screen position. The mean values obtained are displayed in figure , showing that a ±0.5mm error bar is enough to consider all the measurements as consistent with the true distance of the distantiometer from the screen. At that point the determination of the KM Unit 1 additional optical path was carried out (consisting in the average of 10 measurements), resulting in 420.3±0.5mm. The analogous optical path determination for KM Unit 2 resulted in 419.9±0.5mm. In both cases the error bars intersect the requirement range, which was 421±1mm, so the requirement is fulfilled, as far as our means allow to check it. However, considering the quite-large error bars, a shorter additional optical path has been preferred to a longer one, since in the first case an adjustment (MHWS shimming) is possible.

- The optical path determination results is 420.3±0.5mm for KM1.
- The optical path determination results is 419.9±0.5mm for KM2.

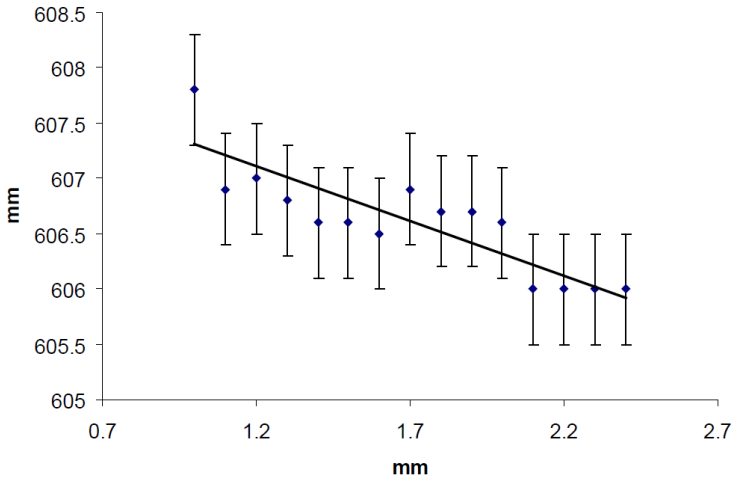

Figure 2.40: *Distantiometer sensitivity verification. On the x-axis there are the micrometer positions, while the y-axis is the distance obtained with the distantiometer. The black line, which is a straight line with angular coefficient equal to -1, represents the expected (true) values., while the blue spots are the obtained measurements. Each measurement has a ±0.5mm error bar.*

2.5.2 Strehl Ratio

KM optical quality requirement is Strehl ratio $S > 90\%$ The optical quality has been verified retrieving the flatness of the beam transmitted by the KM optics in a double pass configuration. The actual Strehl calculation requires complex math, but a simple empirical expression gives a very close approximation of the Strehl ratio in terms of the RMS wavefront error: where e is the natural logarithm base (2.72, rounded to two decimals), and ù is the RMS wavefront error in units of the wavelength. With that expression, the requirement in terms of Strehl ratio can be translated into a RMS WFE requirement: measured RMS WFE must be lower than 50nm. In figure 2.41, the setup used for the interferometric measurement is shown. A Zygo interferometer measures the RMS WFE of the K-mirror in double pass with a previously verified mirror as a reference (for KM1 verification the M2 mirror of KM2, 10 nm RMS, has been used as a reference, while for KM2 verification another flat mirror, 7 nm RMS, has been used). As shown in figure 2.41, the KM1 mean measured RMS WFE is less than 60 nm, since we know the reference mirror contribution (10 nm RMS) and since this is a double pass measurement, the RMS WFE contribution introduced by the KM can be retrieved as nm 30μm RMS

The KM DX mean measured RMS WFE is less than 22 nm, since we know the reference mirror contribution (7 nm RMS) and since this is a double pass measurement, the RMS WFE contribution introduced by the KM can be retrieved as 10.5μm RMS. The requirement is then fulfilled by both the K-mirrors:

$$S = e^{-(2\pi\omega)} \tag{2.5.2.1}$$

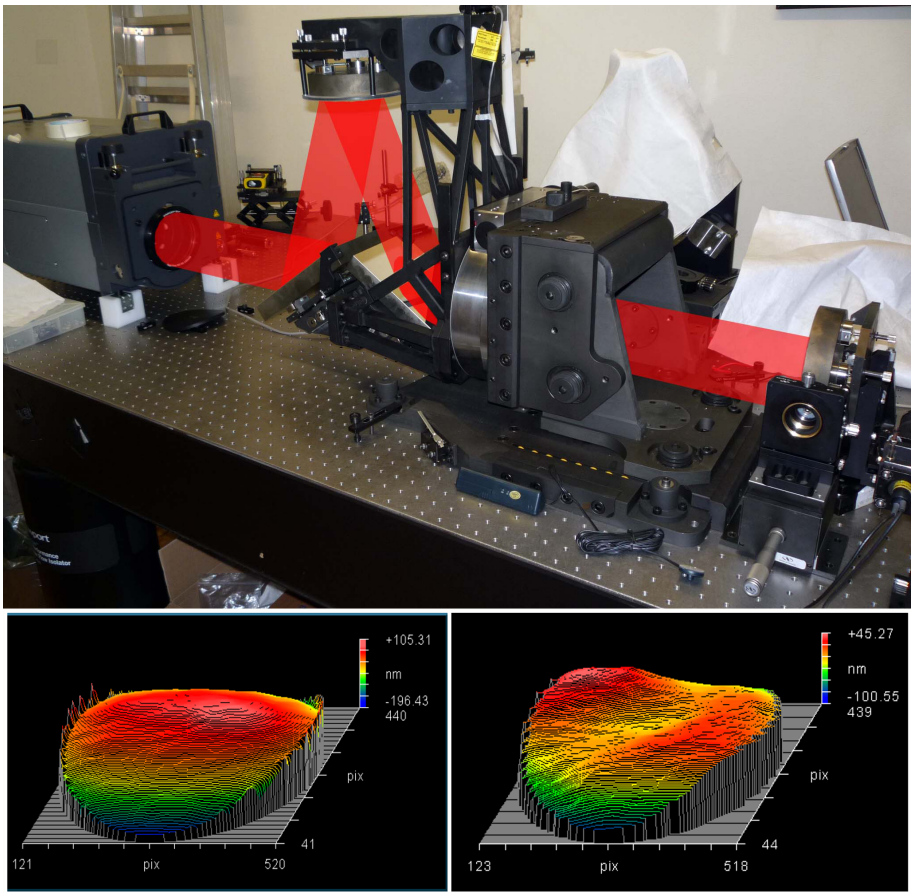

Figure 2.41: *Setup for the interferometric measurements concerning the KM optical quality in double pass configuration. Examples of WF retrieved during KM1 (left) and KM2 (right) Strehl ratio verification test.*

2.6 Conclusions

One of the possible key reference element in optical alignment is represented by a rotational stage, a mechanical bearing, or any similar suitable device with enough accuracy and precision in the rotation such that the optical tolerances are reasonably larger than the imperfections in the rotational movement. NIRVANA on LBT provide three flat mirrors system arranged in a so called K-mirror layout, moving together on a precision rotating stage. Care has to be given when internally aligning and aligning externally with respect to an existing opto-mechanical system, are to be accomplished within a certain degree of precision. To further make the situation more complex, the technical overall requirements can be tight enough that the distribution of the error budget between the various component (imperfect mechanical rotation, imperfect internal alignment, flexures during rotations) is not dominated by a single item. In this case, two optical derotators within the specification are implemented and running in the final Linc-NIRVANA bench. A lot of experience on the testing procedure, modification solution and optics are the best opportunity to evolve any future design and application for giant telescope [17] and for instrumentation for medical and industrial purposes.

Chapter 3

Dust and Fluid Sensor

In this chapter are described two sensor prototype for the analysis of dust and fluids in dense or less dense environment as space or planet atmosphere. The results are obtained after more than one year collaboration with the Spacelight company.

A sensor for the study of the martian atmosfere was developed in the Spacelight company and several optical test were necessary to define the best optical design of the prototype. The science concept is the measurement of the scattered light deflected by the dust particles with a size comparable with the wavelength of the incident light. The amount of energy measured per time unit gives a statistical value about the dust diametral dimension.

A second sensor developed in Padova is able to see the discontinuity of a volume filled with dense or less dens fluid (air, water or glass) and can measure in a single shot the local distribution of refraction index. The pyramid wavefront sensor is the main components and gives to the prototype an high sensitivity measurements with respect to the Shac-Hartman or the curvature sensor.

The synergy of both sensor can produce surely interesting results for a lot of human application. However the purpose was to start getting friendly with the wavefront sensing techniques in order to test and upgrade the performance up to the top of the requirements for current application with rewarding results.

3.1 Dust Sensor

Dust and water vapor are fundamental components of the study of planet atmosphere and to understand the climate and its evolution [23]. In such environment dust and water vapor have (and have had) a strong influence. Generally speaking the analysis of dust or fluid for planet and moons of the solar system can provide a technological solution for a lot of human application starting from medical research to industrial purpose [9]. The tests described in this chapter characterize the beam produced by an optical fiber source for the dust sensor. The instrument breathe the dust and illuminate the particles flux with a thin "knife" of light in order to measure the light scattered backward and forward. The scattering is measured by a photodiode and from the bump energy intensity and distribution it is possible to derive the dimension of the dust particles. In this report we describe two optical bench setup to test multi-mode laser diode and fiber optic coupling. The light of a laser diode is focused inside an optical fiber. The output signal is studied to measure the numerical aperture (NA) of the fiber, the speckle pattern and the top flat intensity as a remark of a correct light input in fiber core.

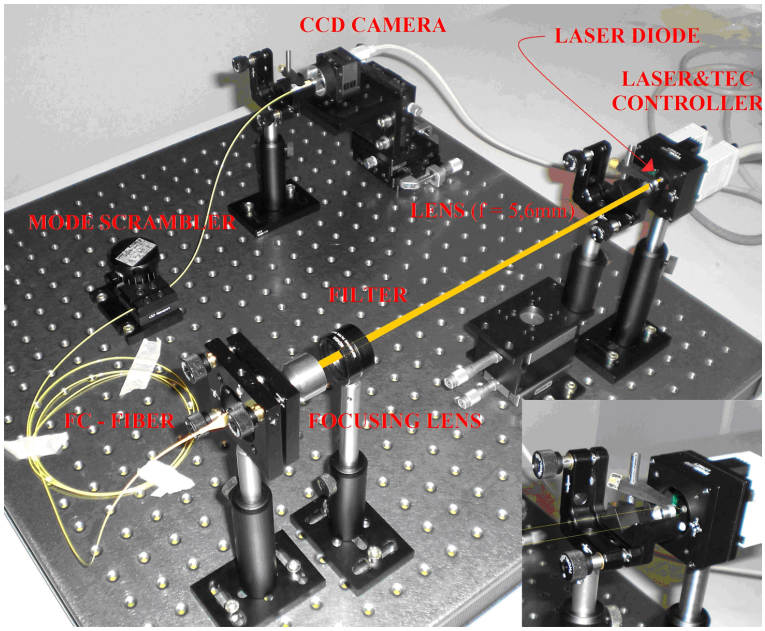

Figure 3.1: *One lens of about 5.6mm of focal length collimate laser diode light into the focusing lens with FC fiber adapter. The fiber pass in a "mode scrambler" and ended in front of the CCD camera observe where the signal is recorded.*

3.1.1 NA<0.22 input Beam

The laboratory setup:

- Multymode laser diode 808nm wavelength, L808P200
- Laser diode with λ=808μm and temperature controller, ITC510
- Neutral density filter with 0,01% trasmissivity, ND40A
- Multymode FC fiber optic with 100um core and 2m length
- Aspheric lens LT220P-B with NA=0,25 f=11,0mm and diam=5,6mm.
- Focusing pacage F810FC-780, with aspheric lens, NA=0,25 and f=35,9mm
- Camera CCD uc480 from Edmund, with computer USB interface

The first tests uses a 808μm laser diode allocated inside a laser temperature controller. The effective laser diode astigmatism is measured with a micrometer by using a fluorescence screen because of the mechanical impossibility to put closely to the diode emitting surface the camera and the filter. We measured all distances with a micrometer We assume a distance of 0.5mm from the diode surface to the glass window. First results gives:

- 3.6 deg for horizonal axis.
- 37.3 deg for vertical axis.

The vertical angle is limited by the window aperture that produce an evident and marked light loss. This diode features will bring to a collimation beam with a thin profile in one direction and a divergent/convergent beam for the other

	Min [deg]	Typical [deg]	Max [deg]	Measured [deg]
Horizontal beam divergence	8	10	12	3.6
Vertical beam divergence	25	30	40	37.3

Figure 3.2: *Table with the values estimated for the horizontal and vertical astigmatism of the laser diode.*

axis because of the marked astigmatism. The beam is collimated by using the aspheric lens LT220P-B. To collimate the beam in the other axis It should need a cylindrical lens not used here for the purpose.

Focus alignment: the laser screwed box allows to adjust lens in focus. Decentering adjustment are not required here because any effect is considered negligible. To minimize any deceneterig effect is decided to use a V-mount and a micrometer to adjust collimation. Collimation of the beam is adjusted when measuring fiber output variation and stopped when top luminosity is reached on the detector.

Tip-tilt alignment: the focusing lens mounted in the conic mount from Thorlabs is mounted on a 10arcsec sensitivity tip-tilt mount. This adjustment allows to appreciate on the focal plane of the lens where is placed the fiber core a shift of about 20μm of the laser diode image, depending on screws and manual rotation. To ensure the light spot on the fiber core we observe with camera CCD the fiber intensity output curve in function of focusing package tip-tilt.

The collimated laser beam footprint on the focusing lens have a rectangular shape of about 1.5x5 mm with the bigger axis quasi parallel to the gravity because of orientation of laser diode emitting surface. The way the light enter inside the circular fiber core depends on tilt regulation so it is possible to observe on the detector a circular distribution of light that became a bright ring just before disappearing. This effect is not visible during tip regulation. That is because there is not an homogeneous light angle distribution in pupil aperture of the focusing lens. Some angles can excite high fiber mode (visible ring) when moving along y axis direction.

When the fiber output transmit maximum power (in correspondence of the maximum of luminosity curve) we can suppose the best diode image overlapping on fiber core.

3.1.2 Numerical Aperture

The NA is measured by using a couple of images of the fiber light output. First image is acquired from a zero reference position that correspond to a value on camera micrometer. The second image is obtained by shifting the camera from the zero reference position of a certain quantity. The radial difference between a couple of images and the distance between them returns the NA value of the fiber output. R1 and R2 are the returned radial value of an IDL program. To be sure that NA value measured is independent from the intensity, from the speckle pattern, or from alignment defocus or tip-tilt, are analyzed images with different zero position and focal length.

Two IDL software measure the radial variation. One program return NA obtained as a parameter of the Gaussian normalized fit. The other one, returns NA% value of table, obtained from a "circularization" of the area calculated as

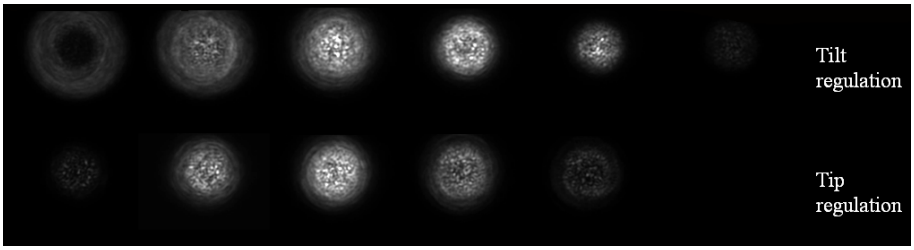

Figure 3.3: *Output shape of the fiber. The specke pattern change with respect to the incident light angle of the input beam inside the core of the fiber.*

Δz	Modulation	Reference image	Second image	$NA_{1\%}$	$NA_{10\%}$	$NA_{20\%}$
5mm	Without mode scrambler	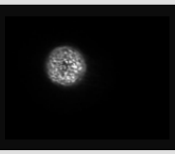	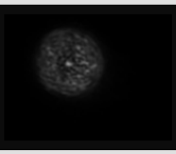	0.073	0.083	0.062
5mm	Without mode scrambler	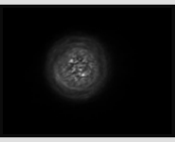	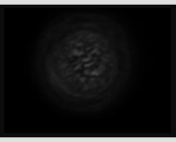	0.14	0.13	0.12
2mm	Without mode scrambler	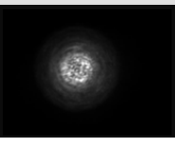	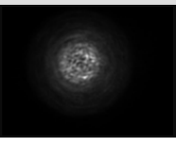	0.13	0.032	0.011

Figure 3.4: *Result of calculation of the NA of the fiber output beam. The input beam angle is smaller than 0.22 and this produce an output profile which is far from the requirement of a flat and uniform distribution profile with NA=0.22 even if the threshold is varied between 1%, 10%, 20%.*

a sum of pixels with normalized intensity upper 1%, 10%, or 20% cut off. We can also consider the radius of one disc image and numerical aperture measured on both images. We can calculate the distance D1 and D2 of fiber output from CCD surface for both images by the formula:

It's not possible to know the absolute distance with high accuracy but to know easily the relative distance by shifting the fiber placed on a micrometric stage. The distance between the two position of the stage compared with the dimension of the disk on the CCD returns the NA angle.

Both methods return an NA not comparable with the required value. The expected "top hat" intensity distribution is not visible and the speckle pattern generate a non uniform light distribution with an intensity variation of about 50%. A "mode scrambler" is used to stress the fiber in order to simulate a long fiber cable. This tool should provide for a speckle merging but no marked evidence of smoothing effect were observed.

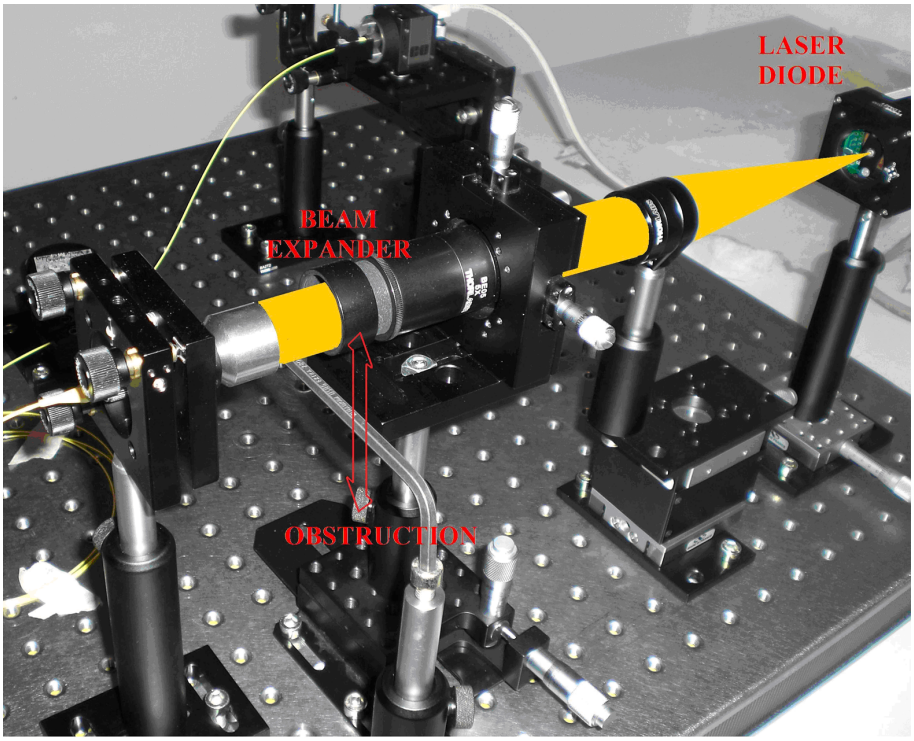

Figure 3.5: *Table with the values estimated for the horizontal and vertical astigmatism of the laser diode.*

3.1.3 NA≈0.25 Input Beam

A second setup was changed to change the diameter of the collimated beam (by using a beam expander) and the telecentric angle of on the fiber core. Instruments and optical setup:

- Multimode laser diode 808nm wavelength, L808P200
- Laser diode and temperature controller, ITC510
- Aspheric lens, diam=25mm, f=150mm
- Neutral density filter with 0,01% transmissivity, ND40A
- Beam expander
- Focusing package, F810FC-780, with aspheric lens, NA=0.25 and f=35.9mm
- Multi-mode FC fiber optic with 100μm core and 2m length
- Camera CCD uc480, with computer USB interface

Is not possible to chance the astigmatic angle but it's possible to select the inner part of the beam to reduce the astigmatic contribution and make the footprint on the focusing lens as circular as possible. A collimated beam is generated by a lens with a 150mm focal length and with a 1" diameter is placed 150mm far from laser diode source. The horizontal beam divergence (3.6 deg) cover all the diameter of the lens.

Is used a beam expander between collimation lens and filter, to select with focusing lens aperture a portion of a more uniform wavefront in order to excite all modes with the same input power. All the focusing lens is now illuminated. In this configuration disappear any "luminous ring" during tip tilt regulation. The light cone that focus on the fiber has got a NA of about 0.25rad.

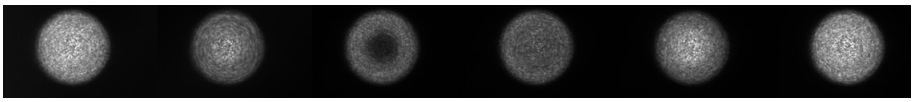

Figure 3.6: *collection of images that show the exited modes during the decentering of the central obscuration in placed in the collimated beam of figure 3.5.*

The NA was measured with the Gaussian fit program but it doesn't gave a stable result. "Circularization" program returns the expected value except when cut off level was set at 0.1%. That is because of the background noise could add "hot pixels" and force the program to overestimate the effective illuminated area of the CCD and NA value consequently.

The mode scrambler doesn't add a great benefit as previous test. In both cases the top hat intensity profile shows a speckle average variation of about 30%. The obstruction tool was occasionally used to stop chief rays to demonstrate that marginal rays excite high orders frequencies clearly visible as a ring form fiber output as shown in figure 3.6to that shows the obstruction moving up-down with the speckle pattern changing.

The expected value for NA=0.22 was measured with a background cut-off of $10\% - 20\%$ of normalized intensity and an error of 1%. Mode Scrambler doesn't modify NA.

To know how a top hat profile could influence our optical project we finally measure the intensity distribution when the circular spot virtually collapse in one axis in order to simulate the laser blade power distribution on the anastigmatic objective prism. That situation allows an integration of speckle that gives a more uniform profile with the fulfill of the RMS energy requirement.

The fiber output depends strongly on the fiber input angle. This angle must be telecentric and must have also the same NA accepted by the fiber or more. We use a 0.25NA focusing lens but since the collimated beam diameter remain smaller than our focusing lens aperture, we produce a light cone on the fiber core with lower NA that lens' one.

Test shows that a tip-tilt misalignment with respect to the fiber axis can produce a light ring shape with a radius bigger than expected. The non telecentric angle can easily excite the high order inside the fiber while subtract light power at low order. This effect is clearly visible in figure 3.6.

This fact can explain also why mode scrambler doesn't run correctly in this case: it has not high order to merge with low order so speckle pattern don't change significantly. Expanding the collimated beam to increase the numerical aperture of focusing lens can provide the correct configuration to.

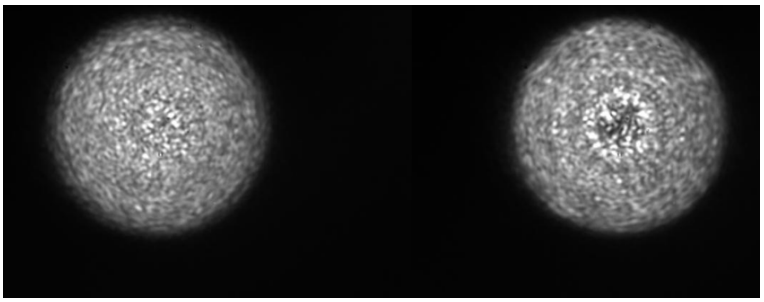

Figure 3.7: *left: image of the output of the fiber with the mode scrambler modulation. Right the same setup condition without the mode scrambler. The speckle merging effect is not evident and the inhomogeneous profile show variation of about 30% of light intensity due to speckle interference.*

Δz	Modulation	Reference image	Second image	$NA_{1\%}$	$NA_{10\%}$	$NA_{20\%}$
3mm	With mode scrambler			0.28	0.24	0.23
2mm	Without mode scrambler			0.44	0.22	0.21
1mm	Without mode scrambler			0.65	0.22	0.22

Figure 3.8: *Result of calculation of the NA of the fiber output beam. The input beam angle is 0.25rad and this produce an output profile which fullfill the requirement with NA=0.22 for different threshold varying between 1%, 10%, 20%. The constraint on the profile uniformity is calculated by collapsing the disk on one axis merging all speckles in a sort of mean distribution.*

3.2 Wave Front Sensor

In this chapter are described several tests and results coming from the characterization and analysis of a pyramid wave front sensor able to perform the reconstruction of a perturbed wavefront thanks to the Zernike polynomials. The concept of the thomografic reconstruction of a transparent medium (atmosphere, liquid, plastic, biological fluids) is here referred and connected to the concept based on the Multi-conjugated Adaptive Optics Layer oriented (MCAO). The laboratory setup is here simplified by using a single source reference for the data acquisition.

The test are performed in the laboratory of the Observatory of Padua on a prototype that observe the pupil plane. In the laboratory setup a pupil aperture is simulated by several lenses to have the possibility to variate the F number of the optical system in order to characterize the variation of sensibility of the prototype. The main idea of the setup is to characterize the static optical aberration of different lenses. At the end of the characterization are given some analyzed and reconstructed wavefronts. Some lenses are also placed in a liquid solution to demonstrate that the prototype can analyze the wavefront in a wide range of condition.

The sensor is mounted on a XYZ stage to scan the focal plane of the lens with high accuracy in terms of decentering, defocus and tip-tilt. The sensor is built using the pyramid prism and a CCD camera while the test lenses are fixed to the bench setup.

A laser He-Ne is used to aligns all the optical components before the calibration of the instrument while the visible light fiber source is used to perform the analysis. A collimation lens is placed at the focal distance from the fiber to collimate the beam. The fiber is placed on a tip-tilt magnetic mount in order to allows the tip-tilt and defocus alignment with respect to the collimation lens. The magnetic mechanism allows to remove the fiber and use the laser for alignment check. An optical window is used to hold the liquids for the test with the lens inside the fluid.

The two transparent surfaces (characterized by an excellent surface quality) are separated by a thick rubber that maintains a distance of about 2 mm apart. A paste applied on the outside of the silicone rubber tube keeps it all together.

To have a correct dimension and separation of pupils on the detector a Star enlarger was placed in front of the pyramid sensor in order to magnify the spot on the pyramid changing the F number. This simple solution is adopted instead of the modification of the vertex angle of the pyramid prism. The laboratory setup used for the experiment is described as follows:

- A laser was used for the purpose of aligning the various optical components in the experiment.
- In front of the laser is positioned (with the aid of a magnetic base that allows the temporary removal) an optical fiber which is the white light source that uses the sensor.
- The lens L1 collimate the beam coming from the optical fiber.
- An optical window can hold the lens in the liquid solution.
- The focal plane of the lens is located on the top of a pyramid which divide the light into 4 parts to form four pupils. Two lenses (L2 and L3), located between the test lens and the pyramid itself, enlarge the size of the spot created by the intraocular lens with a magnification factor of approximately 13.9 in order to decrease the size of the pupils avoiding the

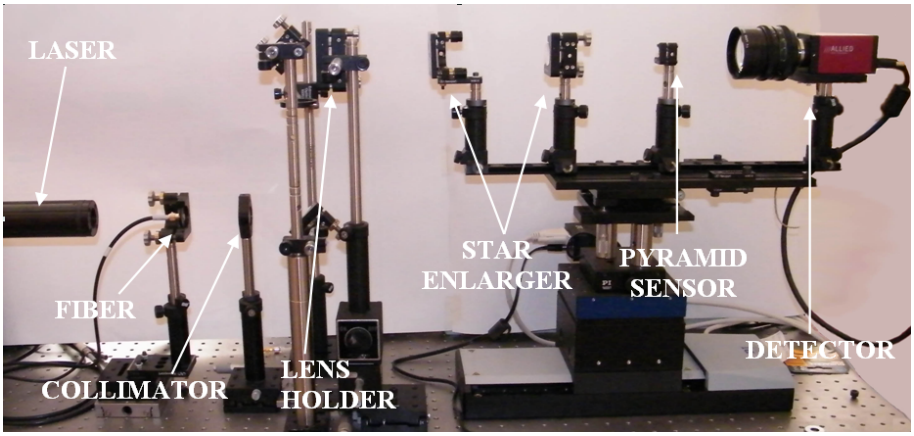

Figure 3.9: *The Pyramid wave front sensor mounted on a three axis motorized stage.*

pupil overlapping due to the small angle at the apex of the pyramid. This optical system is called Star Enlarger.

- A photographic objective collects the 4 beams from the pyramid forming pupil optical plane on the CCD detector, the last component of the prototype.

The following are the main tests carried:

1. Characterization of the setup.
2. Repeatability test on the measurement of the wave front.
3. Estimation of sensitivity, accuracy, stability and linearity range for decentering (the measured values by the sensor are tip and tilt) and defocus.
4. Measurement of optical aberrations.

3.2.1 Alignment

The alignment of the setup is performed thanks to a laser that pass trough the lenses of the setup. By observing the Newton ring it is possible to adjust all the lenses in decenter(accuracy of about 50μn) and tip-tilt (accuracy of about 0.1deg).The motorized stage along the z axis is also aligned parallel to the optical axis with an accuracy of about 0.3deg.

3.2.2 Zernike Polynomials

In the analysis of an optical wavefront is often accomplished by breaking down the so-called Zernike polynomials, mathematical functions that allow to recognize and describe the aberrations that affect the wavefront.

Usually the turbulence of a medium such as the atmosphere could be described by using a finite number of aberration coefficient with different power. Generally speaking the most power is distributed among low order of aberration and define the low spatial frequency of a wave front.

The lower order is the piston that is usually considered for interferometric purpose. For Adaptive Optics and Tomographic analysis are used tip, tilt, defuous, astigmatism, spherical, trifoil and few orders more.

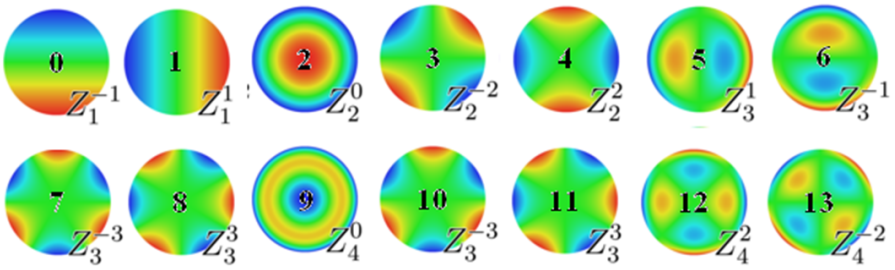

Figure 3.10: *first 14 terms of the Zernike polynomials with the numbers associated to the aberration recalled in this document.*

Motorized axis	Motor	Design resolution [µm/step]	Adjustment	Positioning Accuracy
z	M-511DG	0.033	Defocus	35step (1.15µm)
y	M-501DG	0.0056	Decentering (tilt)	417step (2.33µm)
x	M-126.PD1	0.125	Decentering (tip)	29step (3.62µm)

Figure 3.11: *characterization of the motorized linear stages used to the positioning of the sensor. The accuracies of positioning is obtained for each motor as the standard deviation of 10 re-positioning measurements.*

3.2.3 Focal Length and Sensibility Relation

The purpose of this test is to scan the focal plane of several lenses with different focal length, derive the position of the focal plane by measuring the coefficient of defocus obtained from the analysis of the Zernike polynomials.

The position of the focal plane of the lens is expressed in mm with respect to a reference position called "home" that is recorded in the electronic controller of the linear stage. At the end of the characterization a calibration allows to give the focal position as an absolute value instead of a relative one.

The aberration coefficient are plotted as a function of the sensor location to define the linear range of the sensor. A linear interpolation of these measures provides the equation of a straight line called the "best fit", where m is the inclination as shown in the following equation.

This line provides an empirical law that connects the aberration coefficient and the position of the stage expressed in mm. This law is based on a proportion that binds the calculated intervals (y) and the displacement of the sensor (x). The steps of the stage are then converted to mm and by using the equation of the line we get the location that should match the coefficient of zero defocus:

$$y = mx + q \tag{3.2.3.1}$$

The motor can moves in the position of zero defocus and measure the coefficient as a check. This procedure is usually iterated twice. Ideally this measure would provide a defocus of zero, but in a real case is useful to quantify how much the measured value deviates from the ideal one to quantify the accuracy and repeatability.

It must be noted that the location depends on the value of the inclination m of the best fit line. The proportion (4.7.0.2) leads to table with 3.11 in which is described the value of the defocus coefficient (y-axis) that correspond to the

FOCAL LENGTH (mm)	Resolution requirement [diottric power]	Equivalent Defocus coeff.	Equivalent shift [mm]	Sensor resolution [defocus coeff.]	Sensor equivalent resolution [mm]
150	0.125 =	25 =	2.81	1 =	0.113
100	0.125 =	55 =	1.25	1 =	0.023
76.2	0.125 =	89 =	0.73	1 =	0.008
95.2	0.125 =	56 =	1.15	1 =	0.021

Figure 3.12: *in the table is shown the relation between the resolution power of the sensor (in terms of defocus coefficient) and the corresponding shift interval expressed in mm for lenses with different focal length. The values are compared with the requirements.*

displacement of the stages that move the sensor (expressed in millimeters, or steps).

In the table of fig. 3.12 characterize the resolution of the sensor motor shift wrt the focal length of the test lens. The relation is retrieved from the equation (4.7.0.2) that gives different line with different angular coefficient for each focal length.

3.2.4 Range of Linearity (Defocus)

In this section is tested the linearity range of the Pyramid sensor for a lens of 100mm focal length. When the sensor is placed far from the best focus of the lens the signal saturate on the detector and the acquisition procedure fails the calculation. It is important to define and characterize the range useful for a correct behavior of the sensor in order to estimate the final performances of the prototype.

The prototype aims to measure the wave front but it can also estimate the focal length of the lens with high accuracy. Usually a commercial lens is certified with focal length associated error of about 1% of the focal length. This sensor is able to reach extremely higher accuracy as reported in the following section. With regard to saturation values, it can be seen, from the graph in figure 3.13, that the line tends to became horizontal asymptotically at the margin of the range.

This limit define the acquisition range of the sensor and the linearity range for a lens with 100mm focal length. The linearity range is smaller than the acquisition range and is located in the graph into the central 4mm area in which the data are on a line. The limit of the non linear response of the sensor are form 0mm to 5mm and from 15mm to 20mm.

- Estimated linearity range : 4mm

3.2.5 Range of Linearity (Decentering)

In this section is tested the linearity range of the Pyramid sensor for the same lens with a 100mm focal length and a second one with a 150 mm focal length. The purpose of this test is to characterize the decentering of the sensor with respect to the tested lens.

It is necessary to analyze the Zernike polynomials connected with the tip and the tilt of the wave front. In different words what is considered as a tip-tilt

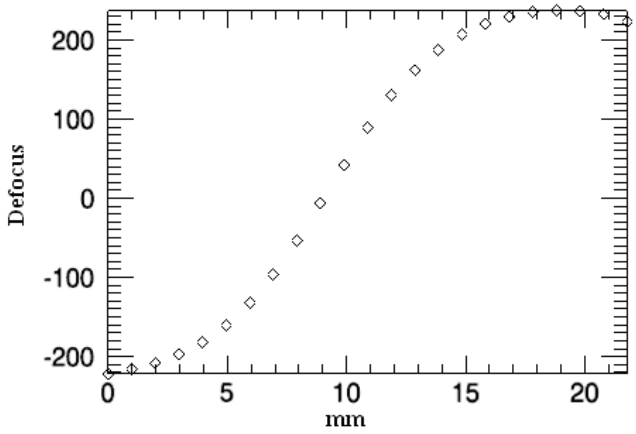

Figure 3.13: *Trends in the value of the coefficients for the defocus lens with f = 100 mm. The interval is not perfectly symmetrical to show the saturation range on the right part of the graphic. The linearity range is represented by the central 4mm area in which the data are on a line.*

by the sensor is translated in a linear displacement of the sensor itself thanks to the motorized axis in X and Y direction.

For each lens are taken measurements of the tip and tilt coefficients values. Two position of the sensor can define a direction for the motor adjustment that minimize the value of the coefficient. The procedure aims to the null value of the coefficient of tip and of tilt because that's the way to estimate properly the defocus coefficient.

There is a small dependence of defocus from the tip-tilt coefficients. In this scenario it's better to find the best centering before the defocus measurement. A plot of the ratios of tip and tilt function with respect to the sensor position make evidence that data are arranged in a straight line.

As for the characterization of defocus is here calculated the "best fit" line along the both axes. Is so measured the relative conversion factor between the coefficients of tip-tilt and displacement of the motors expressed in mm. From the graphs (f=100mm lens) it is observed that the variation is linear in a small range, corresponding to about 0.3 mm, in which the four pupils are all illuminated. In the situation where only 2 pupils are illuminated the program fails and coefficients of tip and tilt are not trusted (extremes of the graph).

- Estimated linearity range for decentering: 200μm

3.2.6 Accuracy of Measurement

The aberrations of a lens is calculated from the values of the Zernike coefficients. Each wavefront is reconstructed using the first 14 polynomials while the high orders are neglected because the general assumption is that the optical power dominates at low modes. Before each acquisition, the wavefront sensor is centered and focused by minimizing the tip-tilt and defocus signal respectively. The remaining tip, tilt and defocus are then subtracted from the same wavefront. The PtV of each aberration is expressed in nanometers.

To obtain the wave front in nanometers it is necessary to calculate a conversion factor that allows to transform the aberration coefficients in a linear

Focal Length [mm]	Sensor Resolution [Tip coeff.]	Δx Motor shift [mm]	Sensor Resolution [Tilt coeff.]	Δy Motor shift [mm]
150	1 =	0.001064	1 =	0.001010
100	1 =	0.000471	1 =	0.000454

Figure 3.14: *Conversion coefficients for two lenses with 100 and 150 mm focal length. The conversion coefficient links the decenter (measured as tip/tilt) with the equivalent displacement of the motorized stages in which is mounted the pyramid wavefront sensors. Tip end Tilt are measured in the x(horizontal) and y(vertical) axes respectively.*

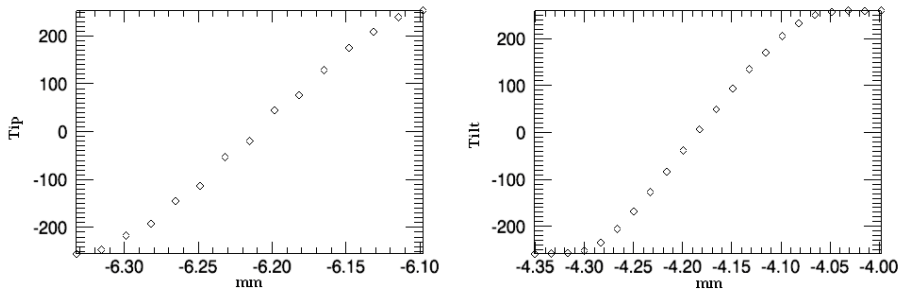

Figure 3.15: *tip and tilt coefficients for a single lens with 100mm focal length. Tip end Tilt are measured by the wavefront sensor and processed as decentering signal to adjust lateral displacement (left) and vertical displacement (right) of the sensor. The estimated linearity range for decentering is rawly 200μm.*

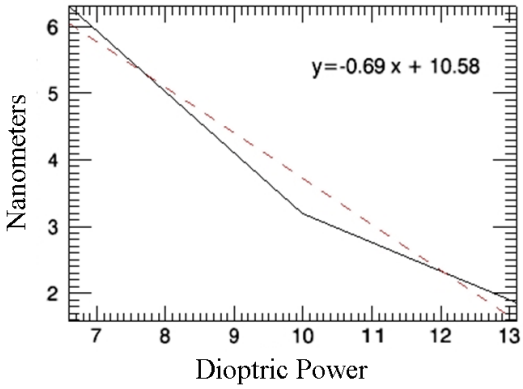

FOCAL LENGTH [mm]	Conversion factor [mm]
150	6.5 E-06
100	3.2 E-06
76.2	1.9 E-06

$$y = -0.69x + 10.58$$

Figure 3.16: *Values of the conversion coefficient that allows to quantify the magnitude of the aberrations in nm expressed here as a function of the dioptric power of the three examined lenses.*

measurement depending by the F number of the lens.

The conversion factor is calculated by the following formula:

$$DefocusCoeff. = \frac{1}{16\sqrt{3}} \cdot \frac{D^2}{f^2} \cdot \frac{\Delta l}{\Delta c} \tag{3.2.6.1}$$

where D is the effective illuminated diameter of the lens, Δl is calculated from linearity graphic and represent the shift in mm of the sensor along the optical axis, Δc is the equivalent range of the defocus coefficient[1].

The ratio l/c is calculated in a neighborhood of the best focus of the lens and is expressed in mm. This value is extrapolated from the line fit of defocus signal to minimize random errors. It is multiplied by the square of the focal ratio appropriately scaled to the value 2, which allows you to switch between the RMS values to PtV. This coefficient changes with the focal length of the lens and this evidence is plotted as a function of the three focal lengths (expressed in diopters).

Any further analysis could demonstrate that probably there is a law that binds the conversion coefficients and focal lengths. Despite the small number of points (3) we obtained a fit which seems to highlight the existence of a relationship between the conversion coefficients and the dioptric power of lenses. It is important to understand how much the conversion factor measured by the sensor depend by the environment condition of the laboratory setup. Repeatability test performed in the laboratory on a f=100mm, D=50.8mm glass lens measure the conversion coefficient at different times and in different setup condition. The values gives a variation between 2.9nm and 3.3nm. Considering that the average PtV static aberration is approximately equal to 100nm it is possible to deduce that the coefficient variation would lead to an errors of 13 nm on the wavefront analysis. This fact allows to estimate the wavefront with an accuracy of $\lambda/50$ because the visible light wave length is rawly 0.55nm. Moreover, by repeating the measurement of the slope and position of best focus for 10 measures on the same interval, the results are in accordance with fluctuations.

- Accuracy of measurement: $\lambda/$ 50

[1] the ratio could be intended also as the inverse of the angular coefficient of the best fit line.

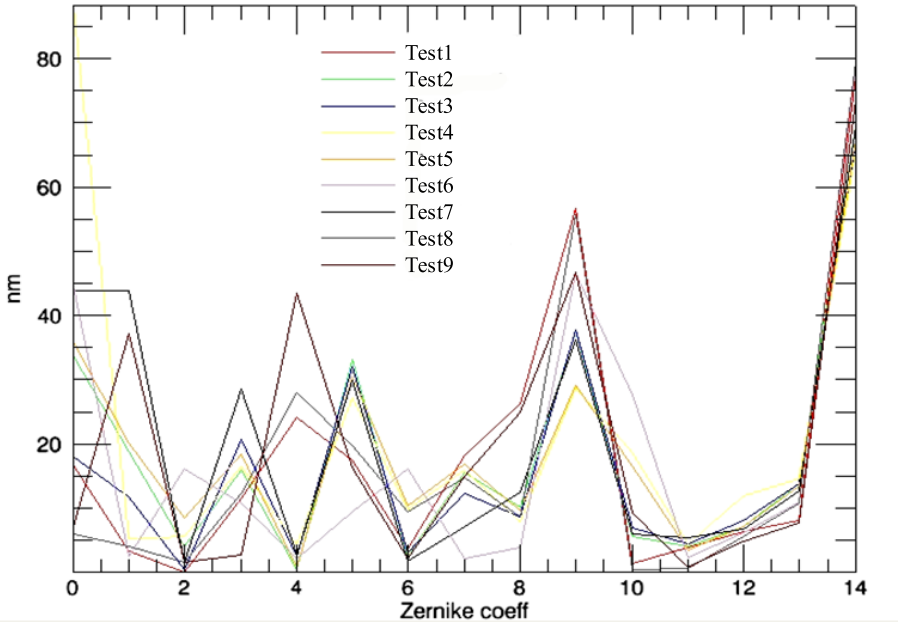

Figure 3.17: *Analysis of aberrations on the 100 mm focal length lens. For each measurement the sensor was adjusted in order to minimize defocus and tip-tilt. The measurements are recorded in different in days or in response to small changes in the setup (removal,reinsertion,rotation of the light source or flip of the lens) to estimate the repeatability of the measurement of the wavefront.*

3.2.7 Prototype Stability

The following test represent the analysis of the stability of the prototype by observing the measured value of the lens aberrations in different condition.

The light shining on the lens through an aperture diameter of 6mm. In the table fo fig. 3.17 is highlighted the value of the wavefront PtV and the value of spherical aberration, which dominates the other aberrations. During some tests the source was removed and replaced (Test3,Test4), the lens was rotated by 90° (Test5), the magnetic base on which the source is located was removed(Test6) and any of this perturbation didn't change the performances and reveal a very stable prototype.

When lens is reversed (Test7) the coefficient of spherical aberration increases, and consequently the value of the PtV. In any case the values of PtV aberrations are less than 100nm, and therefore lower than $\lambda/6$, so it can be concluded that the static aberrations intruduced by the setup and the lens are negligible.

f = 100mm LENS															
Aberration Coeff. [nm]	0	1	2	3	4	5	6	7	8	9	10	11	12	13	PtV
Test1	47	3	17	11	2	10	17	2	4	49	29	2	7	12	83
Test2	46	46	2	30	3	32	2	7	13	38	6	6	7	13	74
Test3	19	12	0	22	3	34	3	13	9	40	7	5	9	15	71
Test4	36	20	4	17	0	35	3	16	11	40	6	4	8	15	74
Test5	38	21	9	19	1	32	11	18	10	31	17	4	8	14	71
Test6	93	6	6	18	5	29	10	17	8	30	20	5	13	15	69
Test7	6	4	2	13	30	21	10	16	9	59	0	1	6	11	84
Test8	16	3	0	11	23	17	3	17	25	54	1	4	6	8	73
Test19	7	35	1	3	41	15	2	14	23	44	9	1	5	7	69

Figure 3.18: *Test3 and Test4 are obtained by repositioning the light source (fiber optic) to see the stability of the setup. Test5 is obtained by rotating the fiber in place of about 90deg. Test7 rapresents wavefront of the "flipped" lens inside the setup. The other wave fronts are taken at different date to see the stability during time. For each measurement the sensor was adjusted in order to minimize defocus and tip-tilt.*

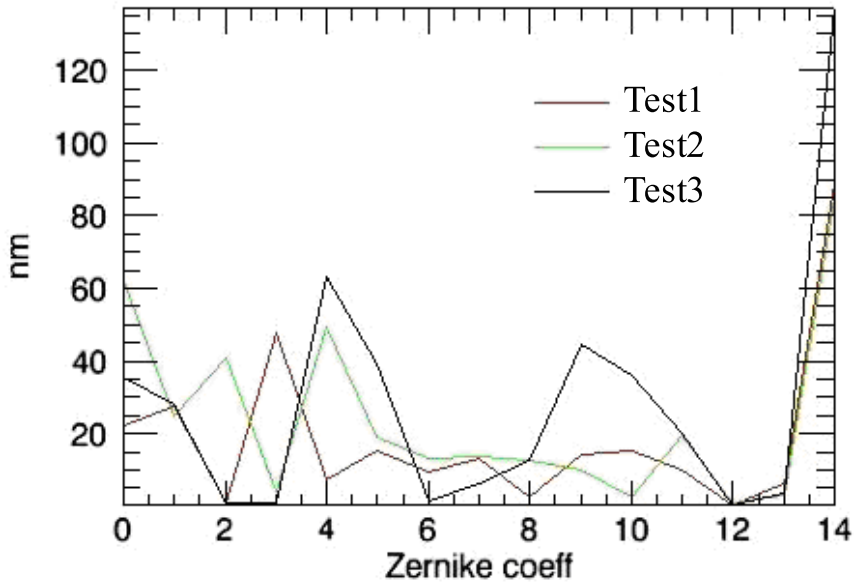

Figure 3.19: *Test1, Test2 and Test3 are here obtained at different date to see the stability during time. For each measurement the sensor was adjusted in order to minimize defocus and tip-tilt.*

f = 150 mm LENS															
Aberration Coeff.	0	1	2	3	4	5	6	7	8	9	10	11	12	13	PtV
Test1	22	27	1	48	8	15	10	13	2	14	15	10	1	6	89
Test2	62	25	41	4	49	19	13	14	13	10	3	20	1	3	85
Test3	35	28	1	1	63	40	1	6	12	45	36	20	0	3	137

Figure 3.20: *Test1, Test2 and Test3 are here obtained at different date to see the stability during time. For each measurement the sensor was adjusted in order to minimize defocus and tip-tilt.*

3.2.8 Wave Front Analysis

The box within the liquid is placed in front of the lens with f=100mm with the known wavefront. The contribution of the lens is subtracted in order to measure the contribute given by the fluid and the transparent box. The box introduces about 37nm of astigmatism due, probably, a slight curvature of the surfaces of the container, however, it is concluded that this aberration is negligible. This residue was calculated by subtracting the two wave fronts and making the fit of Zernike polynomials on the resulting wavefront. In this test is calculated the repeatability of the measurement position given for the best focal plane and are compared several measurement of the same wave front. The measurement is performed by minimizing the values of tip, tilt and defocus. The lens is inside the transparent box fulfilled with the liquid (water). All the system is supported by a tip-tilt mount previously aligned with respect the laser beam with an accuracy of about 0.3deg. During the test the system as been placed and removed away 10 times to measure the positioning accuracy.

For each of the ten measurements the focus position is calculated with respect to a fixed reference in the linear stage. For simplicity we show the differences calculated with respect to the average position. We note that the maximum interval that separates measures WF4 and WF6 is 255μm, a value that is acceptable within the specifications required because for a focal length of rawly 95.2 mm the maximum error in focusing correspond to 1.15 mm which is close to value for the f=100 mm lens of figure 3.12. For a statistical distribution of 10 measures the 3σ correspond to 0.2% of the lens focal length, value that is abundantly within the requirements.

The proper functioning of the procedure depends on the value of focal length that fits by default. It is important to provide a value that approximates the real focal that is to measure. This part is strictly bounded with the calibration of the prototype by using lenses with high accuracy measurement of the focal length. With regard to the repeatability of the measure for the wave front, since the lens can moves inside the transparent box is helpful to rotate properly the wavefronts via software to be able to compare all of them. The correct angle is obtained by maximizing the correlation coefficient as a function of the rotation of one of the two wavefronts. The reference wavefront is the first one and all of the following wavefronts are rotated to orient as the first one of figure 3.22. The figure shows the plot of the values obtained by the fit of the aberrations of the ten already rotated wavefronts. The last value is the total wavefront PtV, who recalls being dependent on the value of the conversion factor ($2.9 \cdot 10^{-6}$ mm) described before. It as been calculated that an error in the input focal length can give a different value of the conversion factor. An error of 5 mm on the input focal length which is the 5% leads to a conversion coefficient which varies

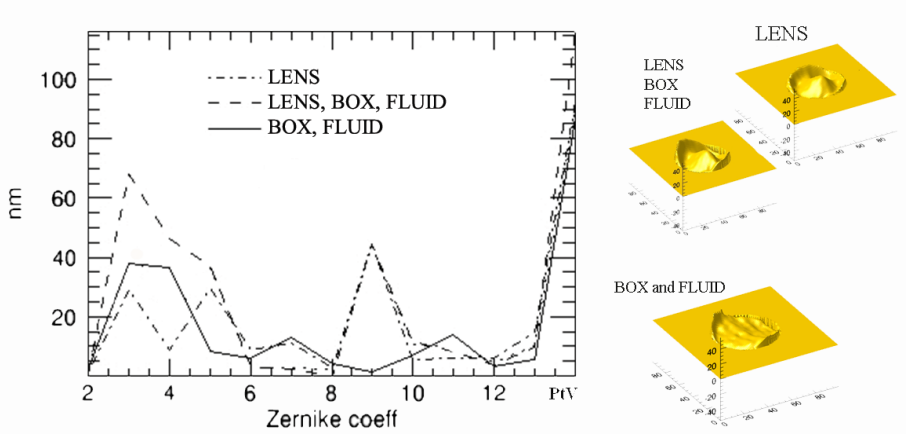

ABERRATED WAVE FRONT	0	1	2	3	4	5	6	7	8	9	10	11	12	13	PtV
LENS	~~44~~	22	2	29	9	30	9	11	3	~~44~~	6	6	6	15	92
LENS and BOX and FLUID	122	10	1	68	~~46~~	37	3	3	0	~~44~~	12	8	~~4~~	10	116
BOX and FLUID	~~4~~	1	3	38	37	8	6	13	~~4~~	1	7	14	3	5	87

Figure 3.21: *the lens aberration, the lens and the transparent box aberration with fluid, the contribution of the box with fluid. The vertical coordinate represent the defocus coefficients multiplied by the conversion factor in order to get the scale in nanometers. The upper value of the displayed scale corresponds to the maximum "defocus coefficients" imposed by the requirements of 0.125 diopters.*

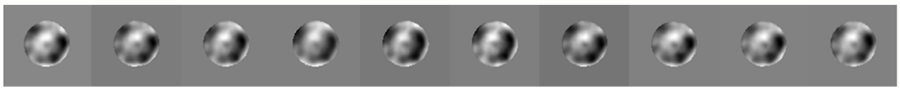

	WF1	WF2	WF3	WF4	WF5	WF6	WF7	WF8	WF9	WF10
FOCUS POSITION [μm]	2	27	-17	171	-65	-84	24	-9	-51	-14
Correlation wrt **WF1** (no rotation)	1	0.97	0.93	0.84	0.85	0.84	0.97	0.94	0.96	0.94
Correlation wrt **WF1** (rotation)	1	0.97	0.96	0.87	0.93	0.94	0.97	0.97	0.96	0.95

Figure 3.22: *The extent of the focus position provides values within a range of about 255μm, with a value of 3σ of 210μm. The correlation referred to the first wavefront WF1 returns higher values for rotation angles that determine the best matching between the two wavefronts.*

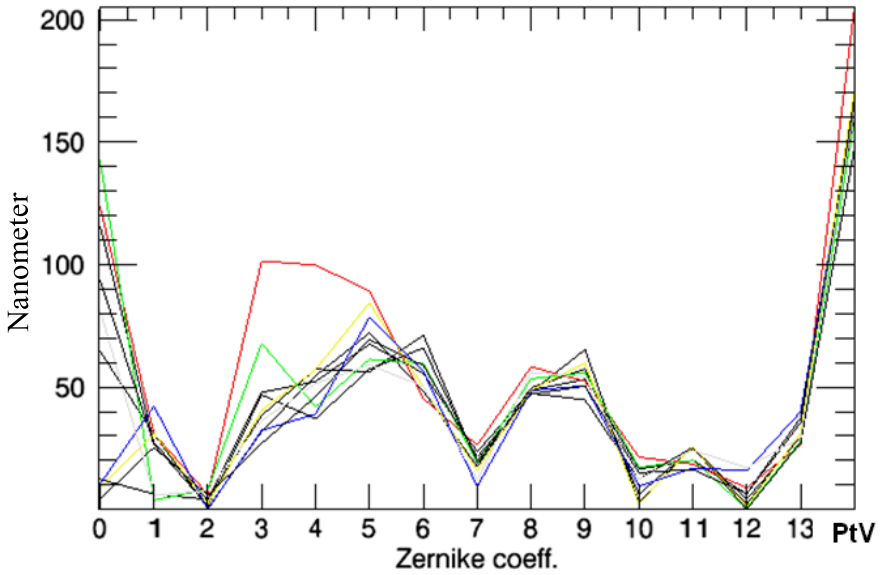

Figure 3.23: *the first 14 values of the aberration coefficients for the reconstruction of the wavefront generated by a lens with a focal length of about 100mm. Each color is related to a measure of the wavefront described also in figure 3.22. The x-axis from left to right are tip, tilt, defocus, astigmatism, etc...The repeatability of the measurements is higher for wavefront that have a null mutual rotation.*

of about $0.3 \cdot 10^{-6}$ nm, with a consequent change in the wavefront PtV average of about 20 nm (from 170 to 190 nm). The error/accuracy on the estimation of the wavefront PtV should be in this case the 10%.

3.2.9 Conclusion

The wave front sensor prototype is based on the Multi-Coniugate Adaptive Optics (MCAO) used in astronomy for the tomographic analysis and reconstruction of the atmosphere. The concept is used for the LBT telescope associate with the layer Oriented technique to visualize a 3D model of the atmosphere. Both concepts are here simplified to get friendly with the optical components, the alignment, and the data reduction. The target of the test was to acquire skills to understand the physical and optical behavior of the light in order to project and design such instrumentation for astronomy or human application. The instrumental capability can be applied to a wide range of human technological application for example medical research and industrial metrology. The Prototype operational range was tested in the Adaptive Optics Laboratory of the Observatory of Padua (INAF) for lenses with a focal length starting of 50mm up tu 150mm. The measured wavefront accuracy for a lens, in the middle range, with an f=100mm focal length is of about $\lambda/50$ while the repeatability is of the order of 95% (described by the correlation factor). The aquisition/linearity range of the prototipe is of about 4mm for defocus and 200μm for decentering.

Chapter 4

Magic F/15.28 Lantern

In the instrument alignment scheme for LINC-NIRVANA, the instrument will be aligned to the straight LN internal F/15 focal planes. A light source (FISBA interferometer) will be installed at the nominal center of FLN,s on each side and serves as reference for the entire alignment of the instrument. The only exception is the GWS system on each side. In the optical path it is located before FLN,s. Hence, it cannot be directly referenced to the FISBA interferometers. A different reference has to be introduced before the annular mirror. Such a different reference has to reproduce the important characteristics of FLN,s (lateral position, axial focus position, tip/tilt). In addition, it must be picked up in the annular field of view of the GWS Sensor. It was decided to introduce an F/15 light source named Magic F/15 Lantern or (ML), which is a telescope simulator. The light source shall allow to simulate a seeing limited PSF anywhere in the straight (FLN,s) and bent focal planes (FLN,F). The alignment of the GWS System to the Instrument will then include the following steps:

1. Alignment or calibration of the motion plane and axial distance of the ML to FLN,s.
2. Alignment of the GWS System to the ML.

The ML can be used also for other alignment and test purposes. In the order of priority:

- Alignment of the GWS System to the rest of the Instrumentation.
- Correlation of the various coordinate systems in the instrument (Star Enlargers, GWS, MHWS, Patrol Camera, Science Camera, Fringe Tracker).
- Pupil image simulation on the CCD for Software tests and Patfinder experiiment.
- Verification of the alignment of the GWS SEs to the GWS internal focal plane.

A is the Annular Mirror surface with the origin in the pivot point of the annular mirror, directions y and l in the surface of the mirror, z in direction of straight light propagation, $F_{LN,S}$ is the straight LN internal F/15.28 focal plane (SX/DX) to which the full instrument arm (SX or DX) is aligned to. The straight telescope FP has to coincide with F_{LN}.

$F_{LN,S}$ is the folded LN internal F/15 focal plane (SX/DX) is defined by $F_{LN,S}$ and the position and orientation of the annular mirror; F_{GWS} is the GWS

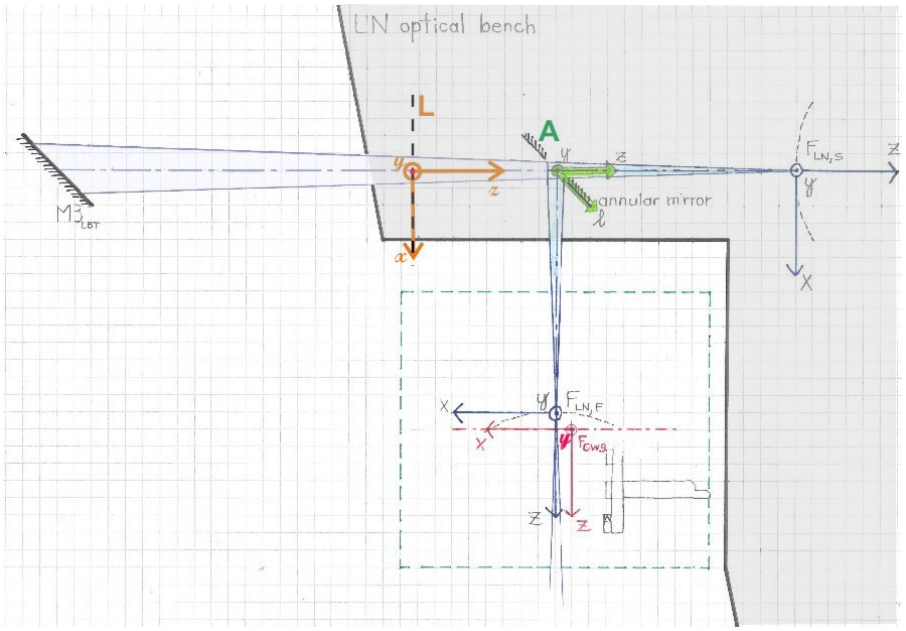

Figure 4.1: *First design of the Magic F15 lantern location in the left side (SX) of LINC-NIRVANA in grey colour.*

Sensor internal focal plane, defined by the common nominal focus position of the SEs and the rotation axis of the GWS bearing; L is the plane parallel to the tangential plane passing through the vertex of $F_{LN,S}$ but in front of the annular mirror. The 'magic F/15.28 lantern' will be positioned along this plane. ML is the Magic F/15.28 lantern.

4.1 Requirements

- Location: The ML shall be installed in front of the Annular Mirror.
- Motion plane: The ML shall move in a plane that is centered on and normal to the axis to which the warm optics is aligned to.
- Motion plane tip/tilt adjustment: The motion plane shall be adjustable in tip/tilt to align it to the axis.
- Travel range: The travel range of the ML will cover a large fraction of the Focal Plane of the GWS. Goal: The outer rim of the GWS focal plane (diameter: 217 mm) can be accessed by the F/15 beam in a circular pattern with a spacing of 90deg.
- Travel range: The travel range of the ML shall cover more than 75% of the accessible field of each SE. This is given for a travel range with a diameter of 200 mm.
- Focus adjustment: The ML shall be able to move also along z-direction to adjust the focus.
- Motorized adjustment: The lateral positioning in the motion plane and the focus positioning shall be motorized.

- Beam tip/tilt adjustment: The beam direction with respect to the motion plane shall be adjustable. It shall be possible to make the axis of the beam parallel to the optical axis of the instrument.
- Beam tip/tilt adjustment: The beam tip/tilt adjustment mechanism shall be lockable.
- Fiber fed: The ML shall be fed by optical fibers. The fibers shall be exchangeable.
- Fiber connector: FC
- Employment: The ML shall be temporarily installable and removable on the LN optical bench for alignment and testing purposes. The installation shall be possible also when LN is on the telescope. It shall also be possible to install it on the GWS Testbed for Pathfinder commissioning.
- Flexible design: Only one ML shall be used for both, the SX and the DX alignment.
- Gravity stable: The ML will be used only in horizontal orientation ("Zenith pointing").

Mechanical Requirements:

- Travel range: x, y: = 200 mm, z: = 15 mm
- Motion plane tip/tilt tolerance: $\pm$123 arcsec (TBD)
- Lateral positioning accuracy per stage: $\pm 5\mu$m
- Bidirectional repeatability in z: $\pm 10\mu$m
- Max. angular deflection per direction (sum of all stages): $\pm 137\mu$rad
- Beam tip/tilt adjustment sensitivity: $\pm$15 arcsec

Optical Requirements:

- F-Number: 15.28
- Light source type: incoherent white light
- Bandpass for alignment: narrow band, centered on λ=0.630μm
- Bandpass for coordinate system mapping: 0.6-1.25μm
- PSF diameter: similar to seeing limited PSF allowing for linear response of the pyramid WFSs in both GWS and MHWS
- Exit pupil position: 14 m
- Design wavelength: λ=0.630μm. Achromatic design, if possible
- Oversized collimator: A fraction of the collimated beam, which is part of the F/15 optics, shall be able to bypass the remaining optics. Collimated light shall be accessible in the GWS focal plane at a constant offset from the F/15 beam.

4.2 Tip/Tilt Adjustment Tolerance

Relevant for the tolerance δ_{tt} is the peak-to-valley variation of the length of the optical path between the last lens of the ML and the motion plane of the SEs. In a perfectly aligned instrument, this variation must not exceed the tolerance x for the distance FP15 and SE lens1. This tolerance is partially used up by the focus alignment of each SE. Here the tolerance is assumed to be a factor of 2 lower. Furthermore, the tip/tilt tolerance δ_{AM} of the annular mirror has to be considered (but is negligible).

$$\delta_{tt}^2 = arctan^2(\frac{x/2}{d}) - \delta_{AN}^2 \tag{4.2.0.1}$$

However, the outer tip/tilt adjustment is not necessary at all, if the axial position of the ML is adjusted as function of the position in the motion plane. In this case, the inclination of the motion plane with respect to the optical axis of the instrument has to be determined. The procedure would be similar to the procedure of the actual tip/tilt adjustment of the motion plane: The focus is measured with the MHWS at several positions in the MHWS FoV. But instead of minimizing it by adjusting a tip/tilt mechanism, it is minimized by moving the ML in axial direction. A spherical model can be fitted to extrapolate the focal plane into the GWS FoV. In this case, the positioning device can be much simpler. The inclination of the motion plane with respect to the optical axis of the instrument can be arbitrary, as long as it is covered by the z-travel range. Second advantage: the ML will simulate the focal plane curvature.

- Tolerance for the distance FP15 and lens1 (x): ±0.13mm
- GWS focal plane diameter (d): 217 mm
- Annular Mirror unidirectional repeatability (δ_{AM}): 15arcsec
- tip/tilt tolerance (δ_{tt}): ±60 arcsec

4.3 Lateral Positioning Accuracy

Plate scale of the FP15: 613μm/arcsec. The required lateral positioning accuracy is driven by the task to relate the various coordinate systems in the instrument to each other. Coordinate transformations should be accurate to ±0.1 arcsec on sky (the resolution of the patrol cameras). To calibrate the coordinate systems, several points in the focal plane have to be reached by the ML. Each of these points may be revisited with an error of less than 61.3μm.

- Positioning accuracy in the focal plane: ±60μm
- The positioning accuracy in the focal plane is a function of the accuracy of the stages and the stages pitch/yaw.
- (Assumed) accuracy per axis (per 100 mm): ±5μm
- (Assumed) focal length of ML (f): 400 mm
- Max. lateral shift in FP due to angle errors : ±55μm

However, the outer tip/tilt adjustment is not necessary at all, if the axial position of the ML is adjusted as function of the position in the motion plane. In this case, the inclination of the motion plane with respect to the optical axis of

the instrument has to be determined. The procedure would be similar to the procedure of the actual tip/tilt adjustment of the motion plane: The focus is measured with the MHWS at several positions in the MHWS FoV. But instead of minimizing it by adjusting a tip/tilt mechanism, it is minimized by moving the ML in axial direction. A spherical model can be fitted to extrapolate the focal plane into the GWS FoV. In this case, the positioning device can be much simpler. The inclination of the motion plane with respect to the optical axis of the instrument can be arbitrary, as long as it is covered by the z-travel range. Second advantage: the ML will simulate the focal plane curvature.

- Max. angular deflection (sum of all stages): $\pm 137\mu\text{rad}(arctan[55/4 \cdot 10^5])$
- Max. pitch/yaw per stage (3 stages[1]): $\pm 45\mu\text{rad}$

If this is given, a calibration of stage positions with the help of a focal plane mask is not necessary. The discussed method of introducing a focal plane mask has several disadvantages:

- The alignment of the mask to the optical axis in the straight focal plane FLN,s is difficult (esp. in tip/tilt)
- The position calibration procedure is lengthy
- There is no easy feedback for the calibration procedure in the 2-6 arcmin annulus (outside of the FoV of the Patrol Camera)
- For pathfinder, placing the focal plane mask in the bent focal plane would be difficult.

It seems to be beneficial to invest in a positioning system with low pitch and yaw and to get rid of the focal plane mask.

4.4 Beam Tip/Tilt Adjustment

The commonly used specification for the tilt of the incoming beam was derived from the famous 1/10 of the sub-aperture criterion.

- Max. angle between beam-SE motion plane: ± 1 arcmin
- Beam tip/tilt adjustment sensitivity[2]: ± 15 arcsec

This requirement, however, is necessary primarily for the superposition of several light sources on the CCD. This will not be the case for the ML. Moreover, the ML cannot simulate the non-telecentricity of the focal plane, which is considered in the design of the pupil re-imager. The constant angle of incidence, the ML produces over the entire field, will result in a field dependent shift of the pupil images on the CCD. The CCD will have to be repositioned in order to maintain the position of the pupil images on the CCD.For the GWS the angle

- will change from 9 arcmin to 27 arcmin
- angle of incidence change across the field: 18 arcmin
- pupil image shift on the CCD 1.8 sub-apertures = 3.6 pixels = 86,4μm

[1]The actual pitch/yaw requirement depends on the mounting of the stages

[2]Annular mirror doubles the angle. And annular mirror has a unidirectional repeatability of 15 arcsec.

For this purposes the angle of incidence of the beam, and with that the zero point in the motion plane of the CCD is somewhat arbitrary. For the verification of the alignment of the GWS SEs, however, it might be interesting to have a 90° angle of incidence. The aforementioned static (pseudo-telecentric) angle already introduces a circular trajectory of the pupil images on the CCD, as the bearing rotates (and the ML follows). A non perpendicular angle of incidence will increase the radius of the circular trajectory. So we might want to stick to the original requirement and ask for:

- beam tip/tilt adjustment sensitivity: ±15 arcsec

4.5 z Travel

For the z-travel range the following has to be considered:

- Focal plane curvature
- focus tolerance
- Tip/tilt tolerance of the motion plane, if it is not adjustable
- focal plane curvature radius: 1024 mm
- FP axial shift @3 arcmin radius: 6 mm
- (Assumed) tip/tilt tolerance of motion plane 4 mm
- (Assumed) focus tolerance 5 mm
- required travel range in z: 15 mm

The bidirectional repeatability is driven by the lower value for the depth of focus

- MHWS depth of focus (for λ=0.633μm): ±0.24 mm
- GWS depth of focus: ±0.13 mm
- Magic F/15 Lantern Design

Because some of the tolerance is already used up by the focus alignment of the SEs, the actual repeatability should be better.

- bidirectional repeatability in z: ±10μm

This can easily be achieved by normal micro-positioning stages.

4.6 Light source

For the alignment of the GWS to the instrument, the focus has to be determined by the MHWS. The MHWS is more sensitive in terms of chromatic effects and, thus, defines the requirements. The requirements are derived from the MHWS flexure test

- light source type: white light
- band pass: narrow, centered on λ=0.630μm
- fiber: multimode
- fiber core diameter:

- fiber connector type: FC

For the MHWS flexure test a 300μm core multimode fiber was used to achieve a linear response of the pyramid wavefront sensor. The produced spot size should correspond to that of a seeing limited PSF. Note that for the MHWS flexure test, the F/20 simulator was introduced immediately in front of the SEs, without the magnification of the FP20 optics.

This has to be considered for the size of the fiber core of the ML. The white light source and the narrow band filter can be reused from the MHWS flexure test. To allow for an instrument wide coordinate system mapping which includes the focal planes in the cryostat, a broad band with the low end being $> 1\mu$m has to be injected. Our thermal light source should cover this.

4.7 Optical Design

The focal number should correspond to the focal number that is provided by the Telescope under consideration of the 300mm focus shift for LINC-NIRVANA. The exit pupil should be compliant with the distance to the secondary mirror in the telescope:

- F number (300mm focus shift): 15.28
- Exit pupil position 14m

The design should be achromatic in the range from 0.6μm-1.25μm. This would allow using the ML without any adjustment for both, GWS external alignment and coordinate system mapping. If an achromatic design is not possible, it should be optimized for λ=0.630μm, to suit its main purpose: the external GWS alignment because of its adjustable z-axis, it should be easy to introduce a focus compensation for the coordinate system mapping in the Near-IR.

It was suggested to design the optics as a two lens system, the first lens is used to collimate the beam, the second to focus it with the appropriate focal length.

Collimated light directly injected into the SEs can be useful for the identification of the pupil image positions. A design with an oversized collimated beam was suggested, which allows some of the collimated light to bypass the second lens. The design concept is to use polychromatic light, an optical fiber, a pupil stop and two lenses to collimate and focusing the beam with the correct focal number F/15. The optical fiber source could be exchangeable to vary the core dimension between 50 and 400 micron in order to simulate the dimension of the PSF corrected or seeing limited.

The magic Lantern (ML) will be used to align all the components of Linc-NIRVANA so this beam will be aligned with respect to the optical axis defined by the MHWS which will define the reference for the alignment of the all optical components. The ML will take place on the edge of the optical bench of Linc-NIRVANA in the area of the GWS to simulate the Gregorian focal plane of LBT as shown in figure 4.1 and it could be used to align both sides DX and SX of NIRVANA.

The beam propagates with a F/15.28 focal ratio in the direction of the anular folding mirror that split the light to the GWS sensor dividing the FoV in two areas the inner one of 2x2arminute and the outer part which is is 6x6arcminute.

The Magic lantern is designed to have a 500mm focal length to allows free space between the L2 and the focal plane of LBT. An XYZ and tip-tilt stage adjustment hold the optics on a mechanical interface. The travel range could allows the decentering and tip-tilt regulation in order to map all the FoV of

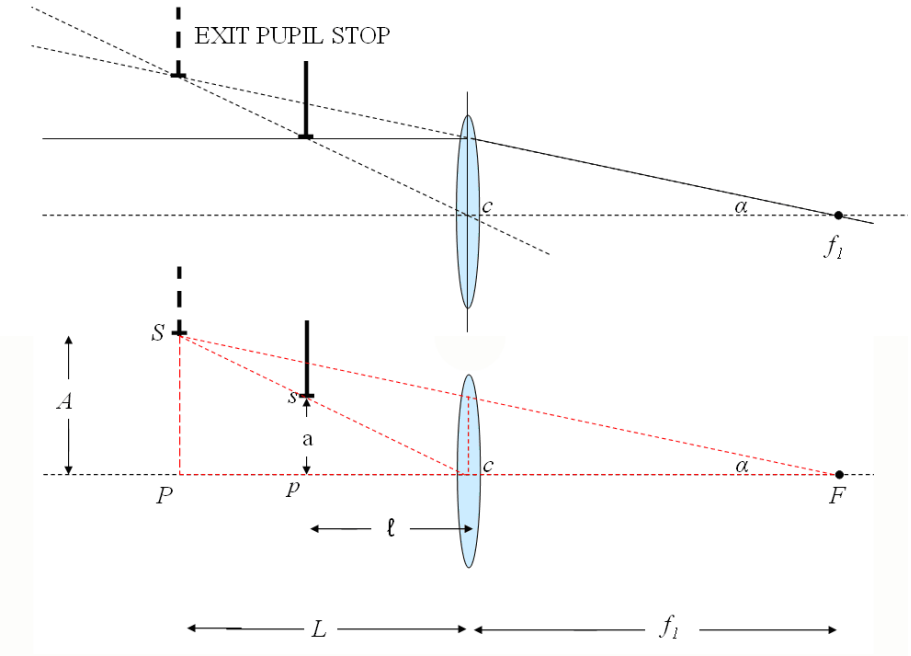

Figure 4.2: *Geometric calculation of te pupil stop position with respect to the L_2 lens.*

LBT from 0-6arcmin. The Magic lantern can be placed in different position in order to hit the anular mirror and reach the GWS or to pass the mirror central hole in the MHWS direction.

The optical path of the light out coming form the fiber source is collimated by the first lens L1 with a focal length of 250mm and D=50mm. A Pupil stop with a diameter of D=33.7mm simulate the exit pupil of LBT placed at a distance of 14m.

In this area could be placed a turbulent screen to simulate the atmospheric turbulence for the Pathfinder experiment. A second lens L2 with a focal length of f=500mm and D=50mm is placed 483mm far from the stop pupil to fix the focal ratio. To define the stop position and so the image position of the pupil is used this relation as described in figure 4.2

$$A : a = L : l \tag{4.7.0.2}$$

$$A = (L + f)sen(\alpha) \tag{4.7.0.3}$$

$$a = \frac{1}{2} \cdot f/15.28 \tag{4.7.0.4}$$

$$\alpha = arctan(a/f) \tag{4.7.0.5}$$

$$L = 14000mm \tag{4.7.0.6}$$

$$l = 483.0mm \tag{4.7.0.7}$$

Stop pupil (L value) [m]	Exit pupil (ℓ value) [mm]
13.0	481.749
13.5	482.411
14.0	483.027
14.5	483.602
15.0	484.140
15.5	484.644
16.0	485.118

Figure 4.3: *table with the variation of the stop image position in function of the variation of the pupill stop positioning error inside the Magic F15 Lantern.*

The formula gives the distance of the stop pupil from the lens L2 in order to simulate the exit pupil of LBT which is placed al 14.0m far from the gregorian focal plane. The accuracy for the positioning of the stop pupil is defined on the limit of 1m to the error allowed on the positioning of the exit pupil. This error is translated to 1mm in the position of the stop. The variation of the stop image position (A) is written in funtion of the variation of the pupill stop position (L) in table of figure 4.3:

4.7.1 First Layout

The design take in account that the dimension of the PSF of the ML should be comparable with the PSF of an uncorrected/corrected star. The fiber source could be changed in order to vary the dimension of the simulated star. The magnification factor of the Magic Lantern is M=2 and so a 100μm fiber core can produce an image of 200μm diameter. The foldimg mirror close to L_2 will provide tip-tilt adjustment to regulate the angle of the telescope simulator beam. The first lens L_1 is placed 250±2mm far from the fiber source in order to collimate the beam. then the pupil stop with an aperture of D=33.7mm calculated by using equation (4.7.0.2). The stop could be placed on a micrometric stage to adjust the distance with respect to the lens L_2 which define the position of the simulate pupil telescope. At a distance of 483.0mm far from the stop is placed the lens L_2 which have a 500±2mm focal length. Two folding mirrors make the ML more compact while the mirror close to L_2 is to regulate the tip-tilt of the beam and for the alignment with an external optical axis.

Distances between the components of the ML:

- fiber source and L_1 lens: 250±2mm
- L_1 lens and the stop: 17mm
- Stop and first folding mirror: 50mm
- First folding mirror and the second one: 200mm
- Second folding mirror and L_2 lens: 233mm
- L_2 lens and the third folding mirror: 50mm

Magic F15 Lantern (Lens characteristics)	L_1 Lens[1]	L_2 Lens[1]
Code	F49-393	F49-290
Substrate	N-BaK4/N-SF10	N-BK7/N-SF5
Diameter [*mm*]	50.00	50.00
EFL [*mm*]	250±2	500±2
BFL [*mm*]	243.41±2	494.50
Thickness [*mm*]	13.25±2	12±0.2mm
Centering [*arcminute*]	3-5	3-5
Coating *(reflectance less than 2%)*	VIS-NIR (400 – 1050*nm*)	VIS (450-800*nm*)
Surf. Quality *Scratch and dig*	60 – 40	60 – 40
Surface Accuracy [λ]	Not specified	Not specified

Figure 4.4: *table with the characteristics of the commercial lenses from Thorlabs used for the design of the ML.*

4.8 Conclusions

The concept of the ML for LINC-NIRVANA is already tested for a current application in the Adaptive Optics laboratory in Padua for the alignment phase of the Ground Layer Wave Front Sensor (GWS) for LBT. A ML has bean aligned and used during the test and the alignment of the Star Enlarger (SE) because of the necessity to simulate the correct F number of LBT (F/15.28) and the correct size of the pupil (33.7mm). The turbulence was also simulated for a small check on the instrumentation performances and sensitivity. The design of the ML is still in review because of possibility to make the ML more compact. In such condition it could be used also for flexure test of the whole LINC-NIRVANA bench once all the optical components and sensors will be installed.

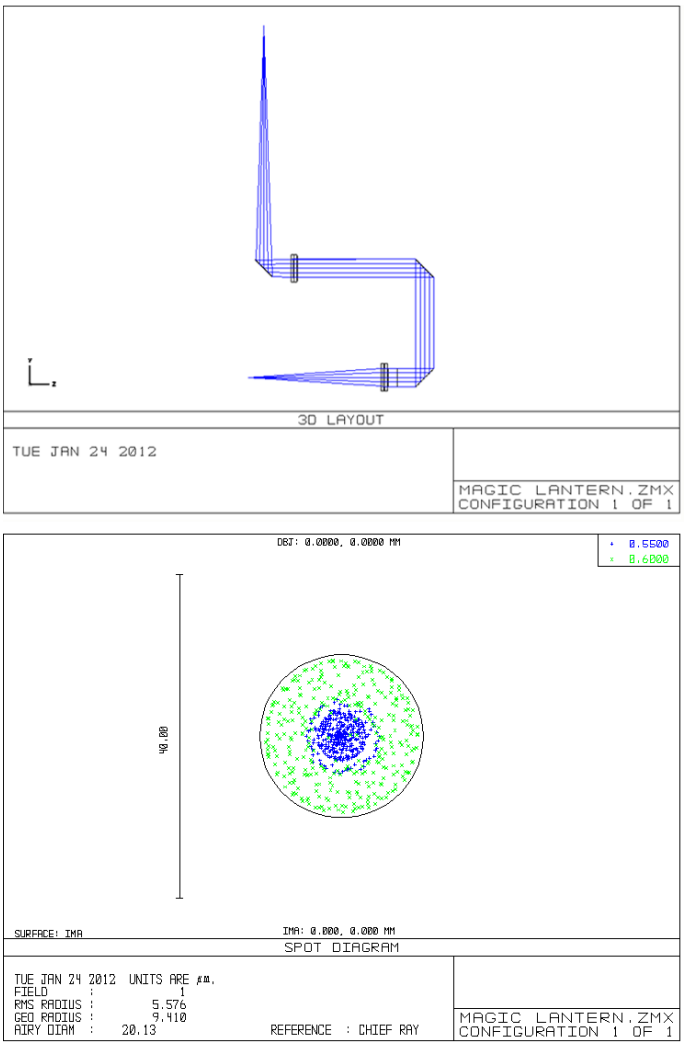

Figure 4.5: *Zemax layout of the ML. Three folding mirrors make the ML more compact.*

Chapter 5

Alma Antenna

The Atacama Large Millimiter Array (ALMA) is under construction in the Northern Chile [1]. The European Consortium composed by TAS-F, TAS-I, MTM and the Italian company EIE-Group where a scientific collaboration took place in December 2011 for Optical simulations. The concept of the new antenna, the design, construction and erection are realized by Alcatel and European Industrial Engineering (EIE-Group) for ESO [21]. Some of the main concepts and technologies adopted on the antennas are the large use of extreme composite materials, the direct drive system, the use of a dedicate metrology system for the correction of the errors induced by the external environmental condition.

The array will be made by a large number (up to 64) of 12m diameter antennas and a number of smaller ones, to be operated on the Chajnantor plateau at an altitude of 5000 m. The antennas will operate up to 950GHz ($\approx 300\mu$m) so that their mechanical performances, in terms of surface accuracy, surface scattering of the solar radiation, pointing precision and dimensional stability, are very tight. The successful realization of the antenna prototype was designed, constructed and delivered by the AEC Consortium (made by Alcatel and European Industrial Engineering (EIE). A collaboration with EIE company was performed in December 2012 to simulate via software the ray-tracing between the antenna mirrors in order to understand the solar burning effect on the secondary mirror area, the Apex, during the sun tracking test.

5.1 Antenna Main Characteristics

The antennas will be fully operative at an altitude of 5000 m, in the open air, working night and day. The antenna is a symmetrical 12m-diameter paraboloid reflector, with Cassegrain geometry, installed over an azimuth mount. The sub-reflector is supported by feed legs in a quadripod configuration. A remotely servo-controlled mechanism, an hexapod inside the Apex, is used for focusing and collimating the beam . The back-up structure is a box with front and backplane connected by radial ribs and tangential plates, to provide stiffness and prevent local buckling. It is made of 16 individual slices which were glued and bolted together under dimensional control using a laser tracker. The BUS has been divided into two halves which remain separated and consent an easier shipment.

The panels of the antenna are largely made of a core of unidirectional pitch carbon fibre, which guarantees low temperature gradients in the structure and good dimensional stability under varying ambient temperature con-

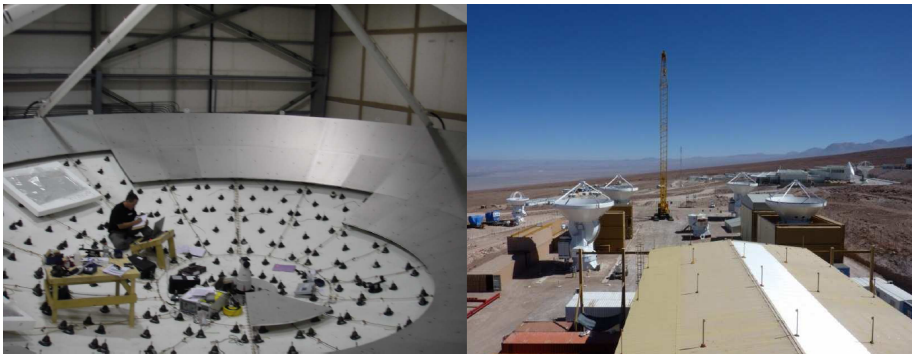

Figure 5.1: *Reflector Panels assembly phase and a general view of the work-site during different mounting and acceptance phases of the antennas.*

ditions, thanks to a high thermal conductivity but a low expansion coefficient. A coating film protects the external layers of the sandwich against moisture. The primary reflector consists of 5 panel rings for a total of 120 panels with an area of about $1m^2$ each. The value of [400-600]nm for the rough manufacturing tolerance and small gravity deformation was achieved with the panel mounted on real adjusters and it was made possible by the replica technology, used in the sandwich panels.

The panels are coated with 200 nm of Rhodium to increase the reflectivity in visible and sub-millimeter band. The high reflectivity reduces the thermal absorption, while protecting the panel from corrosion and oxidation. To prevent any infiltration of water inside the panel, the edges are sealed with a special silicon rubber. A special valve allows for air pressure equalization during air transport and installation at 5000 m. The panels were subjected to a very stringent campaign of development and production test. Each panel is mounted on five adjusters, four at the corners of the panel, and one at the center, constituted by a bell fixed to the BUS on which an Invar rod is mounted. The differential thermal expansion between the Nickel panel and the BUS is absorbed by flexure in the corner adjusters, whereby the central adjuster defines the absolute horizontal position of the panel.

5.2 Temperature Sensor

This document contains the description and the analysis of the issue of apex surface burn marks appeared when the ALMA European antenna points towards the sun. The analysis is necessary to understand the phenomenon and the real causes behind this issue as scattering of primary reflector that should avoid solar concentration as defined in the requirement document. During the shakedown tests with ALMA antenna, a limited area of the apex structure suffered burns due to concentration effect of parabola. A specific test showed that under certain conditions, temperature rise over the critical limit of 80°C on the structure that hold the sub-reflector of the antenna, the Apex. This temperature limit is critical for the carbon fibre structure as it changes its mechanical properties. This test made on site, highlighted that temperature increase quickly reaching up to 80°C during the track in proximity of the sun with an off-axis of about 2.5° - 3.0° angle (maximum effect with 2.8°). Resuming, the on site test results are:

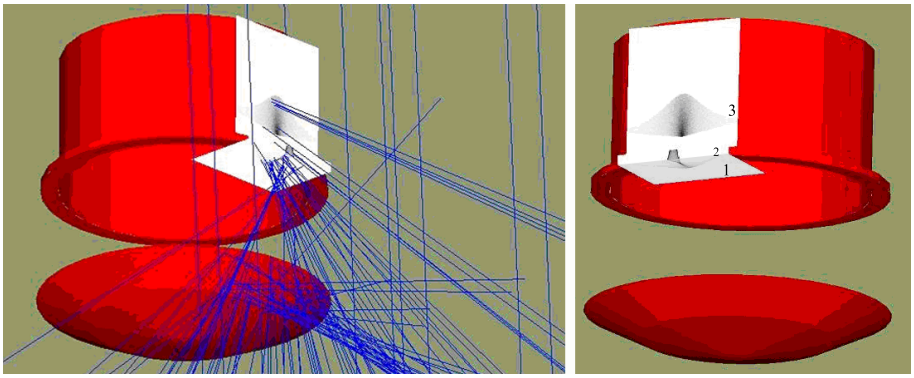

Figure 5.2: *View of the simulated propagation of rays from the primary mirror to the Apex structure. Are visible the virtual detectors and the beam footprint dominated by the COMA aberration for an off-axis of 3deg, while no scattering is here simulated.*

- Sun incidence off axis wrt antenna boresight axis: 2.8°
- Temperature rise: 27.5°C
- Time interval observed: 5minutes (300s)

A first calculation is performed to understand the amount of power energy reaches the Apex structure. Several temperature sensors has been placed on the edge of the Apex during the temperature test and one of them measured a increasing heat of about 27.5°C in a 5minutes time for an off-axis of the sun of 2.8°. It is possible to estimate from these data the solar flux Peak Irradiance fot a comparison with the simulation results. The aluminium sensor head is 25x10x5mm dimension and it is fixed with a white screw on the Apex. The absorbed heat is proportional to:

$$mC_p\Delta T = Q\Delta\tau \tag{5.2.0.1}$$

Were $Q \approx 0.17W$ is the absorbed heat, m is the sensor mass, the Cp is the specific heat, ΔT and $\Delta\tau$ are the increasing temperature and the time range, respectively. The thermal equilibrium equation is:

$$Q \approx I_0 al - S_{Tot}\varepsilon\sigma(T_{Atm} - T_{Sky}) - C \tag{5.2.0.2}$$

where $a \approx 0.25$ is the absorption coefficient of the sensor material (aluminium), $l \approx 2.5cm^2$ is the face-on area of the sensor, $S_{Tot}$is the unknown total flux, $\epsilon \approx 0.2$ is the emissivity and $\sigma \approx 5,67 \cdot 10^{-8}$ is black-body constant.

$$C = a\alpha(T_{sensor} - T_{air}) \tag{5.2.0.3}$$

C represent the convection term and $\alpha = 10$ is a constant to calibrate the convection of local parameters (wind velocity) given in the design document. The calculated irradiance I_0 at the Apex position is

$$I_0 = 5251W/m^2 = 0.5W/cm^2 \tag{5.2.0.4}$$

A second test is also performed by using a potentiometer after the reflection on the secondary mirror close to the focal plane of the antenna above the primary mirror (Feed) give a power irradiance of:

Off axis angle	Peak power [W/ cm^2]			Total power on detector [W/ cm^2]		
	Detector 1	Detector 2	Detector 3	Detector 1	Detector 2	Detector 3
[deg]	%/cm^2	%/cm^2	%/cm^2	%	%	%
1	0.005	0	0.003	0.015	0	0.004
1.5	0.005	0.003	0.005	0.016	0	0.006
2	2.355	0.003	0.003	17.533	0	0.006
2.5	3.053	0.089	0.003	30.073	0.731	0.006
3	3.399	0.508	2.121	31.736	2.450	3.81
3.5	3.616	1.076	0.414	28.369	3.557	12.023
4	3.415	2.156	0.267	18.578	3.592	21.848
4.5	2.975	1.043	1.298	0.621	3.097	32.824
5	0.008	0.003	0.970	0.094	0	26.260
5.5	0.008	0.003	0.766	0.091	0	5.172
6	0.007	0.003	0.003	0.101	0.001	0.007

Figure 5.3: *simulation of the peak intensity and total power on the virtual detectors positioned in the apex structure of the ALMA antenna. With an off-axis of 6° the rays are not involving significantly the apex and that the peak effect is obtained when the off-axis is about 3° to 4°.*

$$I_{Feed} \approx 0.13 W/cm^2 \tag{5.2.0.5}$$

To study the effect of the scattering, it is necessary to build a model which can reproduce the most real behavior of the parabola. Than, a series of investigations require to be made to see the following section.

5.2.1 Off Axis Analysis

The analysis is carried out in Zemax importing a 3D file .iges including the surfaces of the primary reflector, the surface of the sub-reflector and finally the outer surface of the apex structure as in figure 5.2. Three detectors were positioned on the model on a side of the apex in order to capture the incident rays. The scattering present in the primary parabola is not considered at the moment as the analysis aims to verify the amount of incident rays in a variable off-axis configuration. It was imposed an incoming power energy of 1W on the primary reflector of the Antenna and the direction of the Sun was tilted, starting from 1°, up to the limit of 6° where the rays are not incident on apex anymore. These angle will be increased of 0.5° steps, investigating the percentage of power which converge on each detector. The table of figure 5.3 shows that the peak intensity correspond to an off-axis angle of 3°-3.5° which is close the observed value of 2.8deg[1]. The presence of the scattering effect could only smooth the peak power angle dependence.

[1]The power peak was measured after the burning happened. When the temperature increased more than 80°C the antenna was quickly turned to avoid an overheating of carbon fiber.

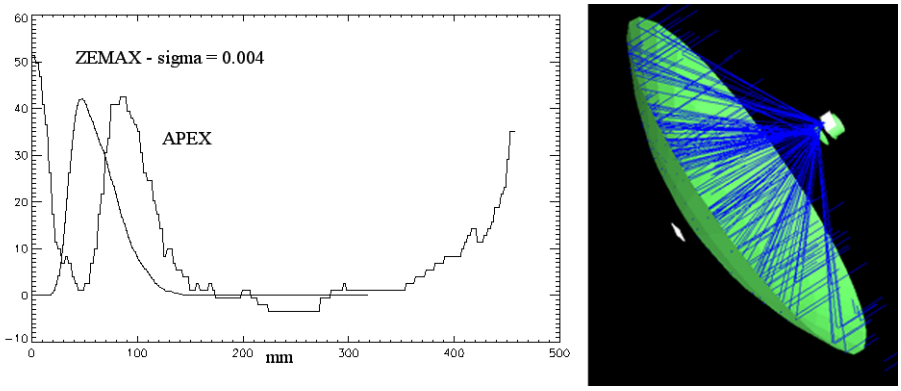

Figure 5.4: *Left: plot with the intensity profile obtained by the image analysis of the burned area on the Apex structure compared with the fit form the simulation. The shift of the two curves is to see better both profiles. Right: Zemax model with the ray tracing from the primary mirror to the Apex and the Feed plane. The simulated off-axis is 3deg.*

5.3 Simulated Coating and Absorbtivity

To model the ALMA antenna surfaces with Zemax are used the design values of

- Primary mirror reflectivity 70%.
- Primary mirror absorption 30%.
- Sub-reflector reflectivity 60%.
- Sub-reflector absorption 40%.

5.4 Geometrical Consideration

In the Alma antenna the diameter of the burned area dimension estimated from figure **??** is 250mm at a distance of 4700mm from the primary mirror on with the scatter occur. By using a simple geometric relation, is it possible to estimate the angular radial dimension of:

$$\frac{1}{2} arctan(\frac{250}{4700}) \approx 1.5^\circ \qquad (5.4.0.1)$$

One other way to estimate the scattering (described in the following sectioon)is to find the best fit of the burned area in terms of width of the gaussian profile and position with respect the vertical direction of the Apex as explained in the left picture of figure 5.4. Form the gaussian profile it is possible to obtain a scattering value of $\sigma = 0.004$ while from the position on the virtual detector it is possible to obtain the off-axis best angle of 3.0° that is in agreement with the measured angle on the ALMA site.

From the position of the burned area wrt the Apex edge it is possible to retrive geometrically the incoming direction of rays and so the area on the primary mirror that reflect the major amount of energy. The resulted area is the parabola rest between R=1700mm and R=3000mm. By using the bolometric

Figure 5.5: *Images of he area interested by the overheating that caused the color change in the white painting of the apex structure close to the secondary mirror. The burned area is estimated to be 200-250mm large.*

Sun intensity power ($1280W/m^2$) is possible to write the formula to define the power intensity in the apex area:

$$I_{Apex} = \frac{I_{Sun} \cdot S \cdot R \cdot \sigma}{s} \approx 0.5W/cm^2 \tag{5.4.0.2}$$

Were the$S = 1.7m^2$ is the area in the primary mirror that send the majority of rays on the Apex, $R \approx 0.8$ is the reflectivity, , $s \approx 400cm^2$ is the burned estimated area and $\sigma \approx 0.2$ is peak scattering profile given in the test report of the panels and is of about 1-2%. This formula takes in account the scattering effect that reduce the geometric radiation propagation at value of 1%. This formula is in agreement with the value of equation (5.4.0.2). The result make evident that the only the 1-2% of the incident light on the primary mirror is back reflected by the panels in a geometrical way directly on the Apex. This radiation can burn the Apex.

5.5 Scattering

In this section are simulated the surface scattering properties of the primary mirror and the sub-reflector. To simulate the surface scattering of the primary mirror we set for simplicity a Gaussian scattering profile. The profile contain more than 99% of energy distribution at a radial distance of 3σ. More than the 50% of the energy is contained into the σ radial value for this reason is decided to convert the 1σ value to an angle (σ_S) in order to describe the efficiency of the scattering surface of the antenna panels.All the simulation are performed with a non resolved source, but in the real case the Sun have an angular radial dimension of 0.27deg. The σ that define the scattering of a surface is varied from 0.002 to 1 corresponding rawly to angles of 0.2deg and 40deg respectively. The off-axis has been fixed to the value of 3° and the sigma parameter as been varied in order to obtain a power profile on the detector that match the 250mm area. The simulated scattering is modeled in order to fit the profile of the burned area returning the value of σ=0.004.The angle defined by a σ=0.004 is of about 0.5deg.

The σ parameter of the sub-reflector is then fixed to the value of σ= 0.04. The simulation returns a power Intensity I_Z on the virtual detector number 3 and I_{Apex} in the detector placed in the Feed.

- $I_{Apex} \approx 102W/m^2$

- $I_{Feed} \approx 16W/cm^2$

The scattering curve provided in the test report by the company returns a peak value that varies between of 1-2% of the incident beam on axis. To scale the simulation values is necessary to multiply the results for 0.01 finding an extremely comparable value wrt equation (5.4.0.2) and (5.2.0.5):

- $I^{\%}_{Apex} \approx 1.0W/m^2$
- $I^{\%}_{Feed} \approx 0.16W/cm^2$

5.6 Conclusions

In such a situation the simulation suggest that the 1% of the surface panel of the primary mirror behave mostly as a mirror producing a scattering of rawly 0.5deg ($\sigma = 0.004$). The amount of IR power could be dominant with respect to the visible light because the roughness of the panels is around 500 nanometer. Any error theory consideration is difficult because of the uncertainty in the input data used to fit the simulations. However is here considered the order of magnitude of the results insted small differences of a factor two or three. Any further simulation could be compared in the near future with tests that are planned in the ALMA Antenna by the EIE company after this very first simulation results.

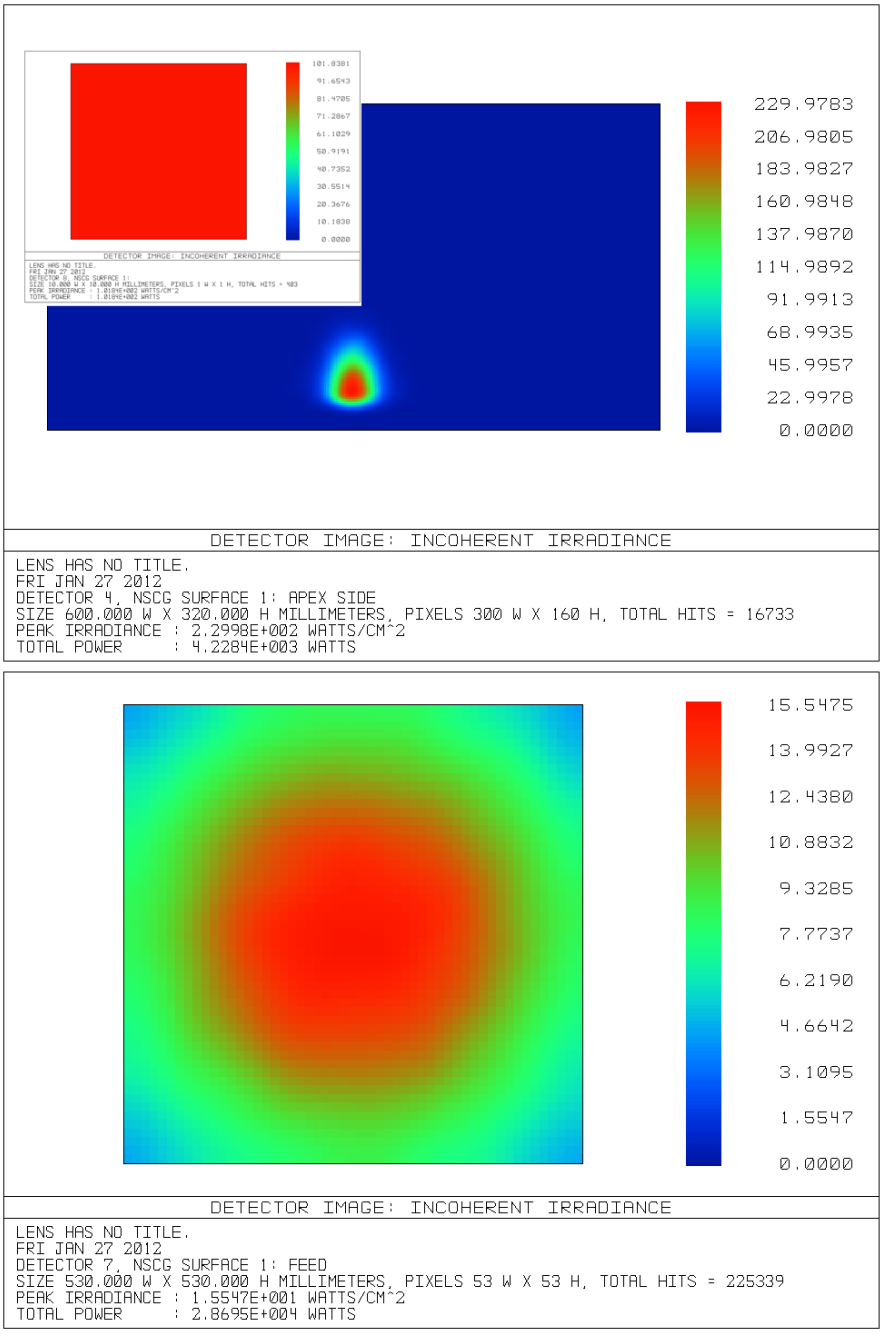

Figure 5.6: *simulation of the scattering of the primary mirror and sub-reflector. On the top the detector placed in the Apex. The red detector have a* $1cm^2$ *size and is used to calculate the real irradiance on the apex structure. Down the virtual detector placed in the Feed.*

THANKS TO my all friends and colleagues for the support.

Bibliography

[1] M. Apers, G. Marchiori, M. Pozzobon, P. Emde, P. Lapeyre, M. Suita, F. Rampini, and S. Stanghellini. Manufacturing and on-site assembly of the European ALMA production antennas: a status report. In *Society of Photo-Optical Instrumentation Engineers (SPIE) Conference Series*, volume 7012 of *Society of Photo-Optical Instrumentation Engineers (SPIE) Conference Series*, Aug. 2008.

[2] C. Arcidiacono, E. Diolaiti, R. Ragazzoni, J. Farinato, and E. Vernet-Viard. Sky coverage for layer-oriented MCAO: a detailed analytical and numerical study. In D. Bonaccini Calia, B. L. Ellerbroek, & R. Ragazzoni, editor, *Society of Photo-Optical Instrumentation Engineers (SPIE) Conference Series*, volume 5490 of *Society of Photo-Optical Instrumentation Engineers (SPIE) Conference Series*, pages 563–573, Oct. 2004.

[3] C. Arcidiacono, M. Lombini, R. Ragazzoni, J. Farinato, E. Diolaiti, A. Baruffolo, P. Bagnara, G. Gentile, L. Schreiber, E. Marchetti, J. Kolb, S. Tordo, R. Donaldson, C. Soenke, S. Oberti, E. Fedrigo, E. Vernet, and N. Hubin. Layer oriented wavefront sensor for MAD on sky operations. In *Society of Photo-Optical Instrumentation Engineers (SPIE) Conference Series*, volume 7015 of *Society of Photo-Optical Instrumentation Engineers (SPIE) Conference Series*, July 2008.

[4] J. M. Beckers. Detailed compensation of atmospheric seeing using multi-conjugate adaptive optics. In F. J. Roddier, editor, *Society of Photo-Optical Instrumentation Engineers (SPIE) Conference Series*, volume 1114 of *Society of Photo-Optical Instrumentation Engineers (SPIE) Conference Series*, pages 215–217, Sept. 1989.

[5] T. Bertram, C. Arcidiacono, J. Berwein, P. Bizenberger, F. Briegel, E. Diolaiti, J. Farinato, W. Gässler, T. M. Herbst, R. Hofferbert, F. Kittmann, M. Kürster, R. Ragazzoni, L. Schreiber, J. Trowitzsch, and V. Viotto. The MCAO systems within LINC-NIRVANA: control aspects beyond wavefront correction. In *Society of Photo-Optical Instrumentation Engineers (SPIE) Conference Series*, volume 7736 of *Society of Photo-Optical Instrumentation Engineers (SPIE) Conference Series*, July 2010.

[6] M. Carbillet, S. Correia, P. Boccacci, and M. Bertero. Restoration of interferometric images. II. The case-study of the Large Binocular Telescope. *A&A*, 387:744–757, May 2002.

[7] E. Diolaiti, R. Ragazzoni, and M. Tordi. Closed loop performance of a layer-oriented multi-conjugate adaptive optics system. *A&A*, 372:710–718, June 2001.

[8] S. E. Egner, W. Gaessler, T. M. Herbst, and R. Ragazzoni. A Closed Loop Layer-oriented Adaptive Optics Test Bed: Applications to Ground-Layer Adaptive Optics. *PASP*, 119:1114–1125, Oct. 2007.

[9] F. Esposito, L. Colangeli, P. Palumbo, V. Della Corte, C. Molfese, J. Merrison, P. Nornberg, J. J. Lopez-Moreno, and J. Rodriguez Gomez. Monitoring the airborne dust and water vapor in the low atmosphere of Mars: the MEDUSA experiment for the ESA ExoMars mission. In *37th COSPAR Scientific Assembly*, volume 37, page 826, 2008.

[10] W. Gaessler, C. Arcidiacono, S. Egner, T. M. Herbst, D. Andersen, H. Baumeister, P. Bizenberger, H. Boehnhardt, F. Briegel, M. Kuerster, W. Laun, L. Mohr, B. Grimm, H.-W. Rix, R.-R. Rohloff, R. Soci, C. Storz, W. Xu, R. Ragazzoni, P. Salinari, E. Diolaiti, J. Farinato, M. Carbillet, L. Schreiber, A. Eckart, T. Bertram, C. Straubmeier, Y. Wang, L. Zealouk, G. Weigelt, U. Beckmann, J. Behrend, T. Driebe, M. Heininger, K.-H. Hofmann, E. Nußbaum, D. Schertel, and E. Masciadri. LINC-NIRVANA: MCAO toward Extremely Large Telescopes. *Comptes Rendus Physique*, 6:1129–1138, Dec. 2005.

[11] W. Gaessler, R. Ragazzoni, T. M. Herbst, D. R. Andersen, C. Arcidiacono, H. Baumeister, U. Beckmann, J. Behrend, T. Bertram, P. Bizenberger, H. Bohnhardt, F. Briegel, E. Diolaiti, T. M. Driebe, A. Eckhardt, S. E. Egner, J. Farinato, M. Heininger, M. Kürster, W. Laun, S. Ligori, V. Naranjo, E. Nussbaum, H.-W. Rix, R.-R. Rohloff, P. Salinari, R. Soci, C. Storz, C. Straubmeier, E. Vernet-Viard, G. P. Weigelt, R. Weiss, and W. Xu. LINC-NIRVANA: how to get a 23-m wavefront nearly flat. In D. Bonaccini Calia, B. L. Ellerbroek, & R. Ragazzoni, editor, *Society of Photo-Optical Instrumentation Engineers (SPIE) Conference Series*, volume 5490 of *Society of Photo-Optical Instrumentation Engineers (SPIE) Conference Series*, pages 527–534, Oct. 2004.

[12] R. Gilmozzi and J. Spyromilio. The European Extremely Large Telescope (E-ELT). *The Messenger*, 127:11, Mar. 2007.

[13] T. M. Herbst, R. Ragazzoni, A. Eckart, and G. Weigelt. LINC-NIRVANA: the Fizeau interferometer for the Large Binocular Telescope. In *Society of Photo-Optical Instrumentation Engineers (SPIE) Conference Series*, volume 7013 of *Society of Photo-Optical Instrumentation Engineers (SPIE) Conference Series*, July 2008.

[14] A. Kolmogorov. The Local Structure of Turbulence in Incompressible Viscous Fluid for Very Large Reynolds' Numbers. *Akademiia Nauk SSSR Doklady*, 30:301–305, 1941.

[15] E. Marchetti, N. N. Hubin, E. Fedrigo, J. Brynnel, B. Delabre, R. Donaldson, F. Franza, R. Conan, M. Le Louarn, C. Cavadore, A. Balestra, D. Baade, J.-L. Lizon, R. Gilmozzi, G. J. Monnet, R. Ragazzoni, C. Arcidiacono, A. Baruffolo, E. Diolaiti, J. Farinato, E. Vernet-Viard, D. J. Butler, S. Hippler, and A. Amorin. MAD the ESO multi-conjugate adaptive optics demonstrator. In P. L. Wizinowich & D. Bonaccini, editor, *Society of Photo-Optical Instrumentation Engineers (SPIE) Conference Series*, volume 4839 of *Society of Photo-Optical Instrumentation Engineers (SPIE) Conference Series*, pages 317–328, Feb. 2003.

[16] D. Peter, M. Feldt, T. Henning, S. Hippler, J. Aceituno, L. Montoya, J. Costa, and B. Dorner. PYRAMIR: Exploring the On-Sky Performance of

the World's First Near-Infrared Pyramid Wavefront Sensor. *PASP*, 122:63–70, Jan. 2010.

[17] R. Ragazzoni, C. Arcidiacono, M. Dima, J. Farinato, D. Magrin, and V. Viotto. Adaptive optics with solely natural guide stars for an extremely large telescope. In *Society of Photo-Optical Instrumentation Engineers (SPIE) Conference Series*, volume 7736 of *Society of Photo-Optical Instrumentation Engineers (SPIE) Conference Series*, July 2010.

[18] R. Ragazzoni, S. Kellner, W. Gaessler, E. Diolaiti, and J. Farinato. Pseudo-infinite guide stars for multi-conjugated adaptive optics on extremely large telescopes. *MNRAS*, 368:1796–1802, June 2006.

[19] R. Ragazzoni, E. Marchetti, and F. Rigaut. Modal tomography for adaptive optics. *A&A*, 342:L53–L56, Feb. 1999.

[20] R. Ragazzoni, E. Marchetti, and G. Valente. Adaptive-optics corrections available for the whole sky. *NAT*, 403:54–56, Jan. 2000.

[21] F. Rampini, G. Marchiori, R. Biasi, S. Stanghellini, and L. Ghedin. The mechanical performances and the metrology system of the European ALMA antenna. In *Society of Photo-Optical Instrumentation Engineers (SPIE) Conference Series*, volume 7733 of *Society of Photo-Optical Instrumentation Engineers (SPIE) Conference Series*, July 2010.

[22] F. Roddier. The effects of atmospheric turbulence in optical astronomy. *Progress in optics. Volume 19. Amsterdam, North-Holland Publishing Co., 1981, p. 281-376.*, 19:281–376, 1981.

[23] The International Medusa Team, L. Colangeli, J. J. Lopez-Moreno, P. Nørnberg, V. Della Corte, F. Esposito, E. Mazzotta Epifani, J. Merrison, C. Molfese, P. Palumbo, J. F. Rodriguez-Gomez, A. Rotundi, G. Visconti, J. C. Zarnecki, and the International MEDUSA Team. MEDUSA: The ExoMars experiment for in-situ monitoring of dust and water vapour. *PLANSS*, 57:1043–1049, July 2009.

[24] V. Viotto, R. Ragazzoni, C. Arcidiacono, M. Bergomi, A. Brunelli, M. Dima, J. Farinato, G. Gentile, D. Magrin, G. Cosentino, E. Diolaiti, I. Foppiani, M. Lombini, L. Schreiber, T. Bertram, P. Bizenberger, F. de Bonis, W. Gässler, T. Herbst, M. Kuerster, D. Meschke, L. Mohr, and R.-R. Rohloff. A very wide field wavefront sensor for a very narrow field interferometer. In *Society of Photo-Optical Instrumentation Engineers (SPIE) Conference Series*, volume 7734 of *Society of Photo-Optical Instrumentation Engineers (SPIE) Conference Series*, July 2010.